ELECTROCHEMICAL QUARTZ CRYSTAL MICROBALANCE STUDY OF BISMUTH UNDERPOTENTIAL DEPOSITION ON RUTHENIUM AND ON ELECTROCHEMICALLY FORMED RUTHENIUM OXIDE

Po-Fu Lin, B.S.

Thesis Prepared for the Degree of

MASTER OF SCIENCE

UNIVERSITY OF NORTH TEXAS

December 2011

APPROVED:

Oliver M. R. Chyan, Major Professor
Robby A. Petros, Committee Member
William E. Acree, Jr., Chair of the Department of Chemistry
James D. Meernik, Acting Dean of the Toulouse Graduate School

Lin, Po-Fu. Electrochemical Quartz Crystal Microbalance Study of Bismuth Underpotential Deposition on Ruthenium and on Electrochemically Formed Ruthenium Oxide. Master of Science (Chemistry - Analytical Chemistry), December 2011, 106 pages, 8 tables, 103 figures, 21 references.

Kinetics and thermodynamics of bismuth (Bi) underpotential deposition (UPD) on ruthenium (Ru) and on electrochemically formed Ru oxide are studied using electrochemical quartz crystal microbalance technique. The Bi UPD and Bi bulk deposition are observed both on Ru and on electrochemically formed Ru oxide electrodes.

The anodic peak potential of Bi UPD shifts slightly to positive potential as the scan rate increases. The peak current ratio ($I_{Anode}/I_{Cathode}$) of Bi UPD and Bi bulk increases as the scan rate increases. Bi monolayer coverage calculated from mass (ML_{Mass}) and from charge (ML_{Charge}) with scan rates dependent are compared both in Bi UPD region and in Bi bulk region. Stability and oxidation time effects are also investigated.

Bi UPD on Ru and on electrochemically formed Ru oxide are quasi-reversible, scan rate independent, oxidation time dependent, and have higher plating efficiency on Ru. However, Bi bulk deposition on Ru and on electrochemically formed Ru oxide are quasi-reversible, scan rate dependent, oxidation time independent, and have higher plating efficiency on electrochemically formed Ru oxide. Both Bi UPD adatoms and Bi bulk are unstable in 0.5M H_2SO_4.

ACKNOWLEDGEMENTS

I would like to take this opportunity to thank all the people who helped me accomplish this goal throughout my graduate studies. First of all, I would like to give my deepest gratitude to my major advisor, Dr. Oliver Chyan, for his kindness and patience in guiding me throughout my graduate studies. Without his guidance and support, I would not be able to accomplish this goal.

In addition, I would like to give my special thanks to our group alumni, Kai-Hung (Kyle) Yu and Karthik S. Pillia, for their encouragement and support during many difficult times. I really thank Kyle for his generosity in sharing life experiences and for his humorous words that gave me the energy to overcome many obstacles. I would also like to thank Karthik for his philosophical words which enlightened me towards a path of personal growth. I would like to express my gratitude for our group members, Jafar Abdelghani, Sirish Rimal, Simon Koskey, Nick Ross, and Arindom Goswami, who made the lab fun and enjoyable.

Finally, I would like to give my deepest gratitude to my father, Chia-Chuan, and my mother, Hsiu-Hui, for giving me the opportunity to study in the United States. Without their love and support, I would not be able to go this far. I would like to give my special thanks to my brothers, Sheng-Yun and Yen-Nan, for being there with me and supporting me throughout these years.

TABLE OF CONTENTS

Page

LIST OF TABLES

LIST OF FIGURES

CHAPTER 1

INTRODUCTION

1.1. Research Objective

Since the first fuel cell made in the mid-eighteen century, scientists have been dedicated to improve the efficiency of fuel cells as green power sources to reduce air pollution caused by fossil fuel power plants. To improve fuel cells efficiency, catalysts that can lower the activation energy for electrolysis of water or small organic molecules have to be used. Currently, platinum (Pt) is considered as one of the most efficient catalysts in the direct methanol fuel cells (DMFCs).[1] However, the byproduct, CO, in small organic molecule oxidation adsorbs strongly on Pt surface and blocks the active sites for hydrogen adsorption, thereby decreases the Pt catalytic activity.[1] In order to prevent CO poisoning effect and enhance Pt catalytic activity, various multimetallic systems and adatoms modified Pt electrodes have been tested.

Among various fuel cell catalysts, Ru/Pt has found to favor the electrochemical oxidation of formic acid and methanol than pure Pt due to bi-functional mechanism and electronic (ligand) effects.[1, 2] The adsorption of oxygen containing species on Ru atoms at lower potentials promote the oxidation of CO to CO_2.[1, 2]

On the other hand, bismuth (Bi) modified Pt electrode shows four to twenty times higher activities in formic acid oxidation than pure Pt and enhanced methanol oxidation by reducing CO poisoning effect due to third-body effect and electronic effect.[1, 2] Electronic effect of Bi enhanced the adsorption of OH on Pt due to shift in point of zero charge induced by Bi adatoms.[3] Competition between OH and CO for the same Pt sites decreases the CO poisoning effect.[3]

In this thesis, Ru is used as electrode substrate instead of Pt because Ru has high catalytic property with no CO poisoning effect. In addition, because RuO_2 catalyzes CO oxidation [4], electrochemically formed Ru oxide electrode is also used. Bi is chosen because Bi modified Pt electrode enhances methanol oxidation.[1] Because Ru is one of the platinum group metals (Ru, Rh, Pd, Os, Ir, and Pt), which may show similar catalytic property as Pt, it is interesting to see how Bi modified Ru and Ru oxide electrodes will behave as a fuel cell catalyst. However, the electrochemical properties of Bi modified Ru and Ru oxide electrodes have not been study before. Therefore, the purpose of this thesis is to investigate the electrochemical property for Bi adatoms on Ru and Ru oxide and to serve as a fundamental study for potential fuel cell catalyst.

1.2. Research Overview

This thesis is about the electrochemical quartz crystal microbalance (EQCM) study of Bi underpotential deposition (UPD) on Ru and electrochemically formed Ru oxide (Ru echem oxide). In order to study the electrochemical property of UPD in situ with mass change on electrode surface, it is critical to use a mass sensor with sensitivity in nanogram region while simultaneously study electrochemical redox process at electrode surface. Among various analytical techniques, EQCM is one of the most sensitive electrochemical techniques to study underpotential deposition. Chapter 1 describes fundamental knowledge about UPD, cyclic voltammetry (CV), quartz crystal microbalance (QCM), EQCM, and sputter deposition. Chapter 2 demonstrates the complete procedure of making EQCM electrode from a blank quartz crystal. This most

up-to-date procedure is developed from the Interfacial Electrochemistry and Materials Research Laboratory (IEMR Lab). This procedure builds up the foundation for making various EQCM electrodes, even electrodes with different metal-nonmetal ratios, to study their electrochemical properties with surface mass change. Chapter 3 analyzes the electrochemical property of Bi bulk and UPD on Ru and Ru echem oxide. UPD of metal is very interesting because the UPD adatoms can modify electrode surface and change the catalytic property of the electrode. Kinetic and thermodynamic properties of Bi bulk and UPD ML are studied.

1.3. Underpotential Deposition (UPD)

1.3.1. Introduction

Underpotential deposition (UPD) is the electrodeposition of metals on a foreign substrate at potential more positive than its thermodynamic potential for bulk deposition.[5, 6] UPD of metals take place when the bonding interaction between the metal and foreign substrate (M-S) is much stronger than the bonding interaction between the metals themselves (M-M).[5] For the reaction

$$M^{n+} + ne^- \rightarrow M \quad (1)$$

, where M^{n+} is the metal cation and M is the metal, the thermodynamic potential for bulk deposition (E_{bulk}) is represented as

$$E_{bulk} = E^0 - [(RT)/(nF)]\cdot \ln (\alpha^M/\alpha^{Mn+}) \quad (2)$$

, where E^0 is the standard reduction potential (V), R is the gas constant (8.314 J/mole·K), T is temperature (K), n is the number of mole in electron transfer (mol), F is the faraday's constant (96500 C/mol), and α is the activity; for UPD potential (E_{UPD}),

$$E_{UPD} = E^0 - [(RT)/(nF)]\cdot \ln (\alpha^{ML}/\alpha^{Mn+}) \quad (3)$$

, where α^{ML} is the activity for monolayer coverage of metal (M) on the substrate.[7] Because the activity $\alpha^{ML} < \alpha^{M}$, $E_{UPD} > E_{bulk}$.[7] The UPD shifts (ΔE_{UPD}) is $E_{UPD} - E_{bulk}$ [8], which can be converted to Gibbs free energy (ΔG_{UPD}) by

$$\Delta G_{UPD} = -nF\cdot\Delta E_{UPD} \quad (4)$$

$$= -nF\cdot(E_{UPD}-E_{bulk}) \quad (5)$$

$$= -nF\cdot\{-[(RT)/(nF)]\cdot \ln (\alpha^{ML}/\alpha^{M})\} \quad (6)$$

$$= [RT]\cdot \ln (\alpha^{ML}/\alpha^{M}) \quad (7)$$

1.3.2. Theoretical Analysis of UPD Shifts

In 1974, Kolb et al. correlate the UPD shifts with the work function of substrate and depositing metal as

$$\Delta E_{UPD} = 0.5\times(\Phi_S-\Phi_M) \quad (8)$$

, where ΔE_{UPD} is the experimentally observed UPD shift, Φ_S is the work function of the substrate, and Φ_M is the work function of the depositing metal.[5] This equation can not only estimate ΔE_{UPD} for polycrystalline substrates, but also predict the tendency of UPD between metal and substrate.[5, 7] For UPD to take place, the work function for substrate (Φ_S) must be larger than the work function for the metal (Φ_M).[7] Therefore, most of the substrates for UPD studies are inert metals, for examples, Pt (Φ_S = 5.03 eV) and Au (Φ_S = 4.80 eV).[5, 7]

1.3.3. Mechanism of UPD

The mechanism for monolayer formation of metal (M) on substrate (S) (Fig. 1-1) can be described as follows: (a.) mass transfer of solvated metal cations (M^{n+}) to the reaction zone, (b.) electron transfer from S to M^{n+} , and (c.) bond formation of S-M at the defective sites.[5] Because the electrode is solvated, the orientation of solvent dipoles at electrode surfaces needs to be considered when calculating ΔG.[5]

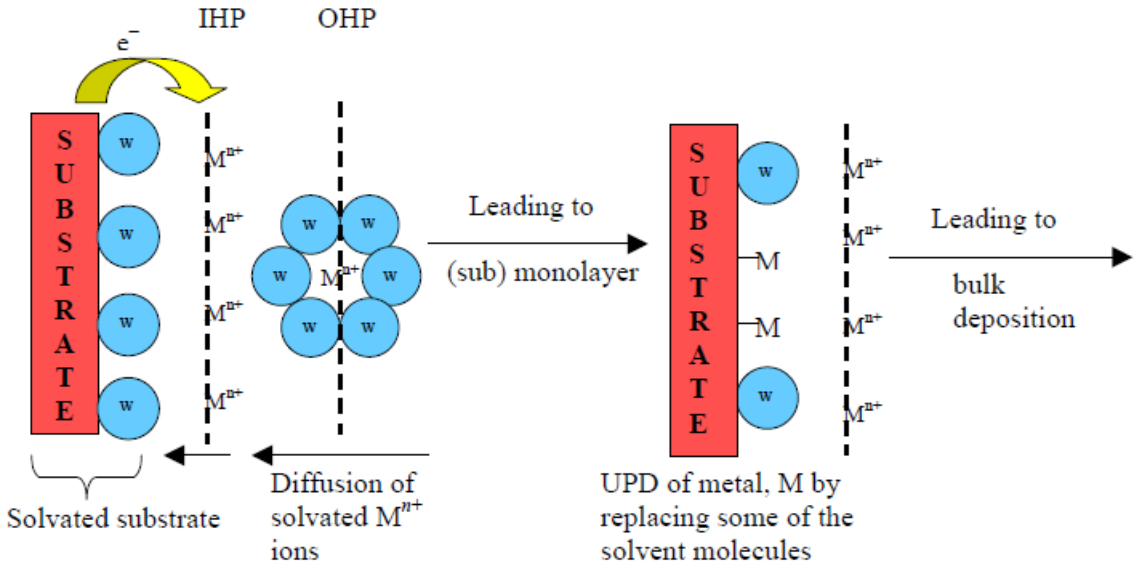

Figure 1-1: Process of underpotential deposition of metal (M) on substrate (S). Solvolysis of metal cations (M^{n+}) surrounded by solvent molecules (w) in the outer Helmholtz plane (OHP) are diffused into the inner Helmholtz plane (IHP). Then the metals replace solvent molecules on the surface of substrate upon deposition and forms bond between M and S. [5]

1.4. Cyclic Voltammetry (CV)

1.4.1. Introduction

Cyclic voltammetry is an important electrochemical technique for studying redox processes, reaction intermediates, and stability of reaction products. [9] This technique

is based on changing the apply potential with time in forward and reverse directions to detect the potential and current associated with redox of analytes.

1.4.2. Reversible System

The important parameters in a CV experiment are peak potentials and peak currents. [9] If the kinetics of electron transfer is fast enough compared with diffusion of oxidant or reductant, the reaction is called a reversible process. [9]

For a reversible process, the electrode potential is governed by the Nernst equation: [3]

$$E = E_0 - RT/(nF)\cdot\ln(\alpha_R/\alpha_O) \quad (9)$$

$$= E_0' - RT/(nF)\cdot\ln(C_R/C_O) \quad (10)$$

$$= E_0' - (0.0592/n)\cdot\log(C_R/C_O) \quad \text{(at 25°C)} \quad (11)$$

where E is the electrode potential (V), E_0 is the standard reduction potential (V), E_0' is the formal reduction potential (V), which contain activity coefficients and some chemical effects of the medium, R is the gas constant (8.314 J/mole·K), T is temperature (K), n is the number of mole in electron transfer (mol), F is the faraday's constant (96500 C/mol), α is the activity, and C is the concentration (mole/L), in which $_R$ stand for reactant and $_O$ stand for oxidant. The formal reduction potential (E_0') for a reversible reaction is [9]

$$E_0' = (E_{pc} + E_{pa})/2 \quad (12)$$

, and the peak potential separation ΔE_p for a reversible process is [9]

$$\Delta E_p = |E_{pa}-E_{pc}| = 2.303\ RT/(nF) \quad (13)$$

$$= 0.0592/n \quad \text{(at 25°C)} \quad (14)$$

where ΔE_p is the peak potential separation (V), E_{pa} is the anodic peak potential (V), and E_{pc} is the cathodic peak potential (V). Irreversible process has $\Delta E_p > 0.0592/n$ V due to slow electron transfer rate. [9]

For a reversible process, the peak current is given by the Randles-Sevcik equation: [9, 10]

$$I_p = 0.4463[F^3/(RT)]^{1/2} \cdot n^{3/2} \cdot A \cdot D_o^{1/2} \cdot C_o \cdot v^{1/2} \quad (15)$$

$$= (2.686 \times 10^5) \cdot n^{3/2} \cdot A \cdot D_o^{1/2} \cdot C_o \cdot v^{1/2} \quad \text{(at 25°C)} \quad (16)$$

where I_p is the peak current (amps), F is the faraday's constant (96500 C/mol), R is the gas constant (8.314 J/mole·K), n is the number of mole in electron transfer (mol), A is the electrode area (cm^2), D_o is the diffusion coefficient (cm^2/s), C_o is the concentration ($mole/cm^3$), and v is the scan rate (V/s). [9, 10] Cyclic voltametry is carried out in unstirred solution to ensure diffusion control. [9]

1.5. Quartz Crystal Microbalance (QCM)

1.5.1. Introduction

QCM is a high sensitive mass sensor. It can detect any substance that adsorbs or deposits on the surface of QCM. With its nanogram sensitivity, QCM has been applied extensively on chemistry, biology, and medical research in recent years. [11]

1.5.2. Basic Principle of QCM

In 1880, Pierre Curie and Jacques Curie found that when applying mechanical stress to the surfaces of acentric crystals, including quartz, rochelle salt

($NaKC_4H_4O_6 \cdot 4H_2O$), and tourmaline, an electrical potential was generated across the crystal with its magnitude proportional to the applied stress. This behavior is called piezoelectric effect. Acentric (non-centrosymmetric space group) crystal has a polar axis due to the dipoles associated with the orientation of atoms in the crystalline lattice. When applying stress on a quartz crystal, dipole is shifted due to the displacement of atoms in an acentric crystalline material. Once dipole shifts, charges are generated within the crystal. Converse piezoelectric effect is the application of voltage across the crystals produce a corresponding mechanical strain. QCM measures the surface mass change based on the converse piezoelectric property of quartz. [12]

Based on the reversible principle of piezoelectric and converse piezoelectric effects, applying alternative electric field across an acentric crystal will generate a vibration motion with fix frequency (Fig. 1-2). [13]

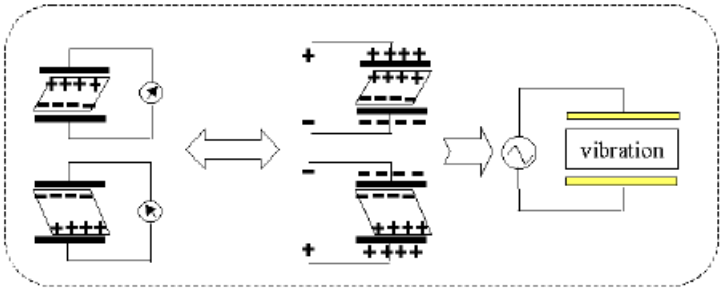

Figure 1-2: Piezoelectric and converse piezoelectric effects. [13]

Quartz crystals that cut with different directions or angles have different properties on the mode of deformation, vibration frequency, and the sensitivity to temperature, etc. [13] Only crystals cut with the proper angles show shear displacements. [12] Within those different cut crystals, AT-cut and BT-cut quartz crystals

show the thickness shear mode with vibration frequency within 0.5 to 250 MHz and 1 to 30 MHz, respectively (Fig. 1-3). [13] In addition, both AT-cut and BT-cut quartz crystals have very low frequency drift in room temperature range. [13]

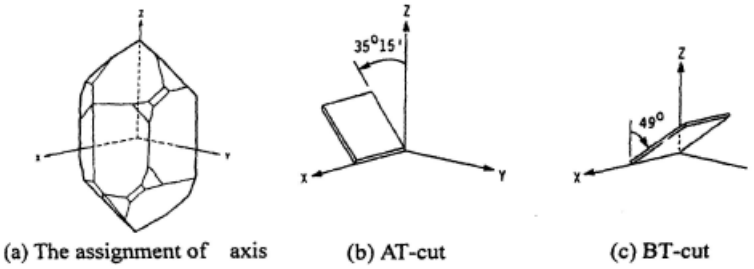

Figure 1-3: Quartz crystal (a) the assignment of axis, (b) AT-cut quartz crystal, and (c) BT-cut quartz crystal. [13]

1.5.3. Sauerbrey Equation

In 1959, Sauerbrey formulated an equation that account the relationship between the mass change and frequency change of a thickness-shear mode quartz crystal under vacuum condition. [14]

$$\Delta f = -2f_0^2 \Delta m/A(\mu_q \rho_q)^{1/2} \quad (17)$$

$$= [-2 f_0^2/(\mu_q \rho_q)^{1/2}] \cdot [\Delta m/A] \quad (18)$$

$$= -C_f \cdot \Delta m \quad (19)$$

where, Δf is the difference between the measured frequency and the resonant frequency of the crystal (1/s), f_0 is the resonant frequency of the crystal before any mass change (1/s), Δm is the mass change (g), A is the piezoelectrically active area (cm^2), μ_q is the shear modulus of quartz (2.947×10^{11} g/cm· s^2), ρ_q is density of quartz (2.648 g/cm^3), and C_f is the sensitivity constant (Hz/g). [14] This equation shows the linear

relationship between the mass change and its corresponding change in vibration frequency. Typically, QCM measurements are accurate when the mass of the film does not exceed 2% of the mass of the QCM crystal. [12]

Few assumptions were made when deriving this Sauerbrey equation. It assumes "no-slip" condition at the QCM-liquid interface; that is, the layer of liquid particles directly in contact with the vibrating region of the QCM surface moves the same velocity and amplitude with the vibrating region (Fig. 1-4). [12, 14] The Sauerbrey equation also assumes the density and transverse velocity associated with the foreign material are identical to those of quartz. [14] In addition, this equation assumes the frequency shift due to a mass deposited at some radial distance from the center of the crystal will be the same regardless of the radial distance. [14]

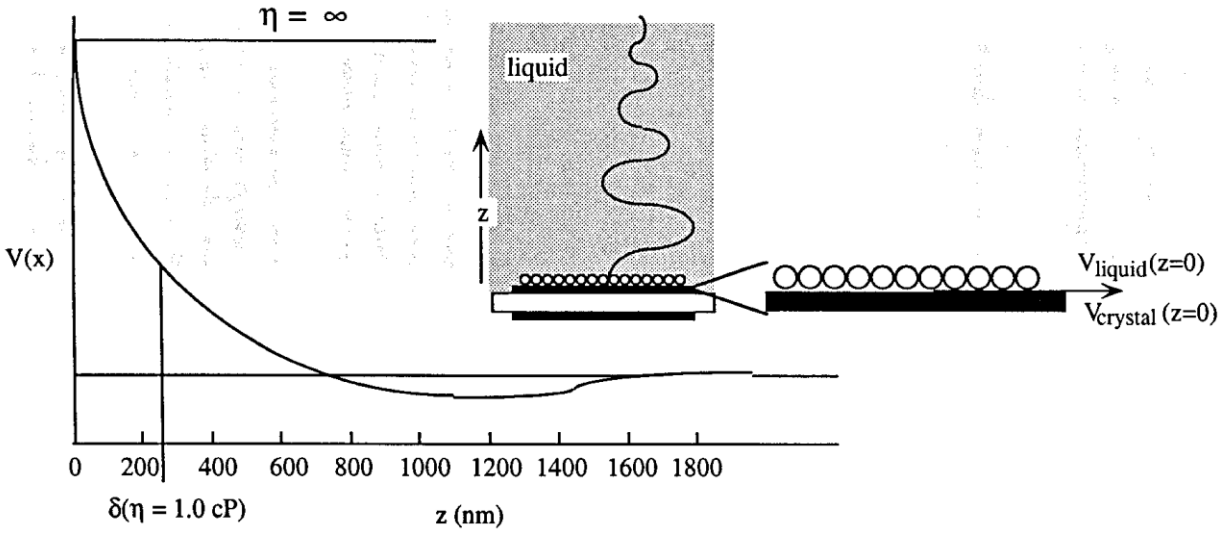

Figure 1-4: Description of the shear wave propagation in a fluid. The y-axis represents the shear velocity (parallel to the resonator-liquid interface) as a function of distance from the resonator-liquid interface. [14]

Because the factors affecting the vibration frequency in liquid condition are not the same as in vacuum condition, in 1985, Brukenstein and Shay incorporate the AC polargraphic diffusion layer thickness [11, 12, 13]

$$\delta = [\eta_L/(\pi \cdot f_0 \cdot \rho_L)]^{1/2} \quad (20)$$

into the Sauerbrey equation and formulate a vibration frequency equation under liquid condition [12, 13, 14]

$$\Delta f = -f_0^{3/2} \cdot [\rho_L \eta_L/(\pi \mu_q \rho_q)]^{1/2} \quad (21)$$

$$= [-2 f_0^2/(\mu_q \rho_q)^{1/2}] \cdot [\rho_L \eta_L/(4\pi f_0)]^{1/2} \quad (22)$$

where δ is the decay length (cm), ρ_L is the density of liquid (g/cm^3), η_L is the viscosity of liquid (g/cm·s), μ_q is the shear modulus of quartz (2.947×10^{11} g/cm· s^2), and ρ_q is density of quartz (2.648 g/cm^3). [12, 13] For pure water (20°C), ρ_L is 0.9982 g/cm^3 and η_L is 1.002×10^{-2} g/cm·s. [13]

1.5.4. Correction to Sensitivity Distribution of QCM

In 1980, Shen Hong incorporated Sauerbrey's sensitivity distribution curve with his experiment data and derived the following formula for the radial distribution of the QCM sensitivity (Fig. 1-5). [11]

$$\Delta f = -f_0^2 /(N \cdot R \cdot \pi \cdot R_z^2) \cdot \exp[1-(r^2/R_z^2)] \cdot \Delta m \quad (23)$$

where R is the radius of a concentric circle with the electrode (cm), R_z is the radius of QCM vibration region (cm), and r is the distance between a point and the center of the electrode (cm). [11] Note the Sauerbrey equation requires uniform film thickness on QCM, which makes the equation valid even though the sensitivity is not constant across the QCM surface. [12]

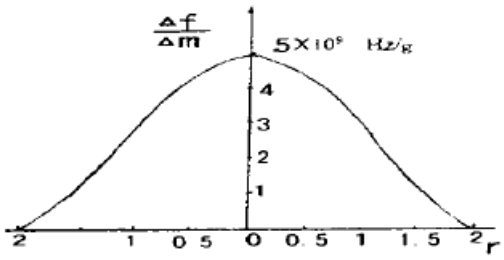

Figure 1-5: Radial distribution of the QCM sensitivity for AT-cut 10 MHz quartz crystal with 2 mm electrode radius. [11]

1.5.5. Equivalent Circuit Representation for QCM and EQCM

In vacuum condition, the QCM can be described as an electrical circuit that has an inductor (L), a capacitor (C), and a resistor (R) connected in series (motional branch) and a parallel capacitor (C_0) (Fig. 1-6). [12, 14]

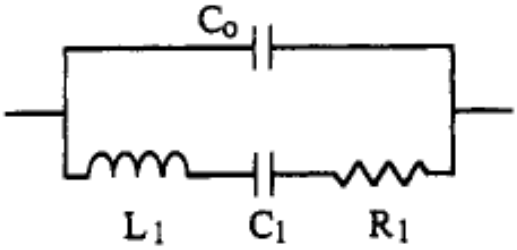

Figure 1-6: Equivalent circuit for QCM in vacuum condition. [12]

In this equivalent circuit, the inductor (L_1) represents the mass displaced during oscillation, the capacitor (C_1) represents the energy stored during oscillation, and resistor (R_1) represents the energy dissipation due to internal friction. [14] The series branch of the circuit is called motional branch because it represents the vibrational behavior of the crystal. [14] The parallel capacitor (C_0) represents the static capacitance of the quartz plate between its electrodes and any stray parasitic capacitances. [14]

This complete circuit is called Butterworth-van Dyke circuit. [14] The equivalent electrical parameters in terms of crystal properties: [14]

$$C_0 = D_q \varepsilon_0 A/(t_q) \approx 10^{-12} \text{ F} \quad (24)$$

$$C_1 = 8A\varepsilon^2/(\pi^2 t_q c) \approx 10^{-14} \text{ F} \quad (25)$$

$$R_1 = t_q^3 r/(8A\varepsilon^2) \approx 100\ \Omega \quad (26)$$

$$L_1 = t_q^3 \rho/(8A\varepsilon^2) \approx 0.075 \text{ H} \quad (27)$$

where, D_q is the dielectric constant of quartz (3.9), ε_0 is the permittivity of free space (8.854×10^{-9} F/cm), A is the piezoelectrically active area (cm^2), t_q is the thickness of quartz (cm), ε is the piezoelectric stress constant, c is the elastic constant, r is the dissipation coefficient corresponding to energy losses during oscillation, and ρ is density of quartz (2.648 g/cm^3). [14]

Kanazawa, Gordon, Bruckenstein, and Shay found that f_s (the series resonant frequency prior to the mass change) dependents on the density and viscosity of liquids when QCM is in contact with a viscous liquid or polymer film. [12] Under this condition, the equivalent circuit of QCM must include the mass loading density (L_L), the resistive viscosity (R_L) of the liquid or polymer, and the mass loading due to a rigid film (L_f) (Fig. 1-7). [12]

1.5.6. Modified Sauerbrey Equation for Viscous Liquid

The viscous coupling of QCM under liquid condition can be incorporated into the Sauerbrey equation (Eq. 1-28). [12]

$$\Delta f = [-2 f_0^2/(\mu_q \rho_q)^{1/2}] \cdot [(\Delta m/A) + [\rho_L \eta_L/(4\pi f_0)]^{1/2}] \quad (28)$$

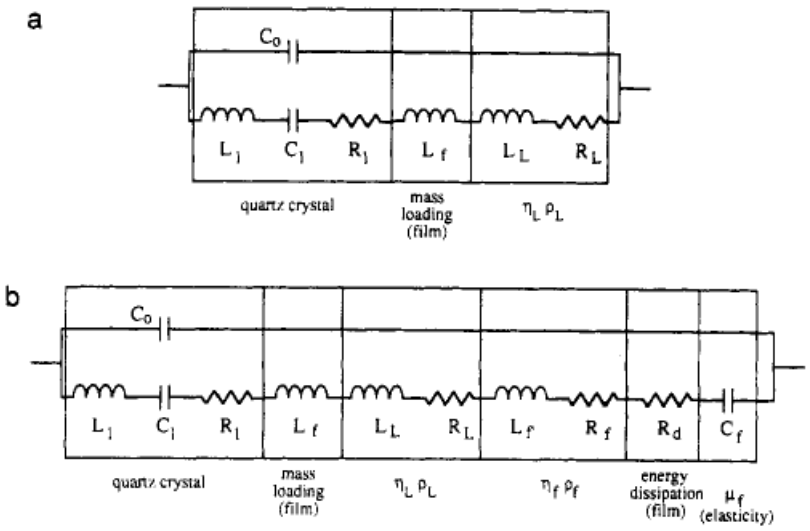

Figure 1-7: Equivalent circuit for QCM in liquid with (a) rigid film and (b) polymer film. [12]

This equation reflects the frequency shift due to liquid loading (which relates to η_L) and surface mass changes (which relates to ρ_L) associated with a rigid film. [12] If the product $\rho_L\eta_L$ is constant, the above equation (Eq. 1-28) reduced to the Sauerbrey equation (Eq. 1-17); however, if Δm is 0, then the frequency will be affected only by the density (ρ_q) and viscosity (η_L) of the medium and Eq. 1-28 reduces to Eq. 1-21. [12] Approximate -800 Hz frequency shifts is observed when immersing one side of the QCM in water. [12]

1.5.7. Modified Sauerbrey Equation for Polymer Film

Under ideal conditions, $\rho_L\eta_L$ is constant and the Sauerbrey equation is applicable. [12] However, polymer films are usually viscoelastic in nature, so the contribution of viscosity (η_f), density (ρ_f), and elasticity (μ_f) of the immobilized film must be considered. [12] When ignores elasticity (μ_f), the modified Sauerbrey equation for polymer film (Eq. 1-29) is similar to that for a liquid. [12]

$$\Delta f = [-2 f_0^2/(\mu_q \rho_q)^{1/2}] \cdot [(\Delta m/A) + [\rho_f \eta_f/(4\pi f_0)]^{1/2}] \quad (29)$$

Both $(\Delta m/A)$ and $[\rho_f \eta_f/(4\pi f_0)]^{1/2}$ terms contribute to Δf, especially for polymer films that experience insertion of counterions or incorporation of solvent that may lead to swelling of the film. [12]

1.6. Electrochemical Quartz Crystal Microbalance (EQCM)

The basic concept of EQCM is combining electrochemistry technique with QCM to study the surface property of an electrode. EQCM can record mass change associated with the QCM electrode while simultaneous performing electrochemical study on the electrode surface.

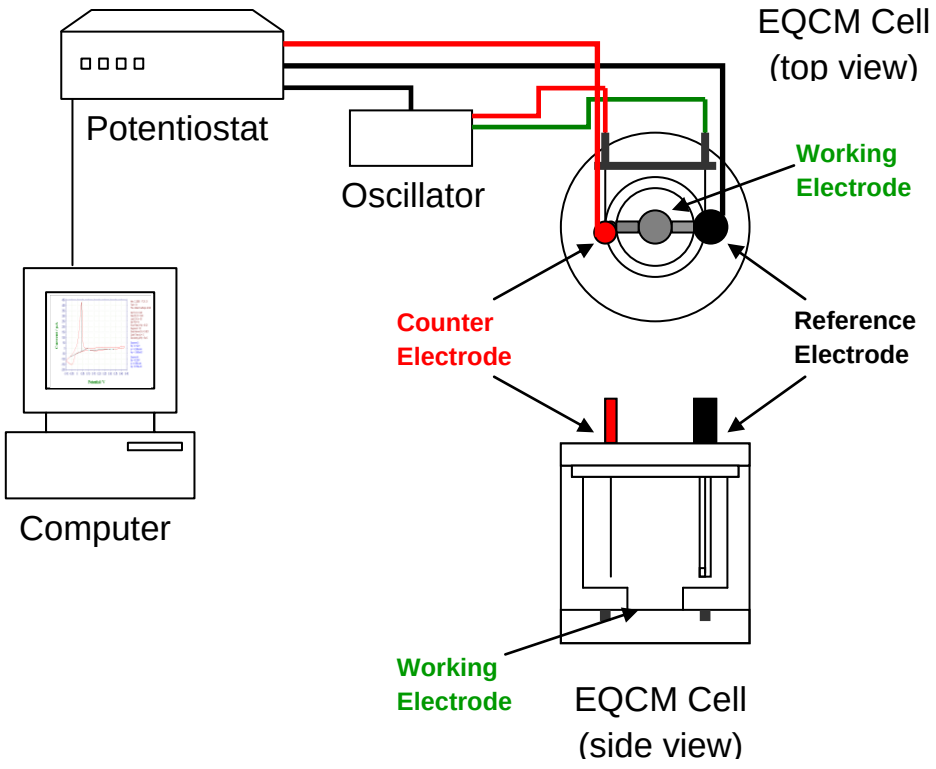

Figure 1-8: Basic setup of EQCM.

1.6.1. Application of EQCM

EQCM study can be classified into two fields— thin films and polymeric thin films. Application of EQCM for thin films involves *in-situ* study of metal electrodeposition such as underpotential deposition (UPD) of metals, electrochemical dissolution of metal films such as corrosion sensors, oxide formation and morphology change of metal electrodes, electrovalency of anions adsorption, hydrogen absorption in metal films, and formation of gas bubbles. [12] EQCM can also study non-metal substances, for examples, adsorption and desorption of self-assembled monolayers of organic and organometallic species and other thin-film systems such as semiconductor materials, catalyst, and antibody. [12]

Two types of polymer films have been studied using EQCM, redox polymers and conducting polymers. Examples of redox polymer films include poly(vinylferrocene) (PVF), poly(thionine), Prussian blue (PB) and related films, and other systems such as poly(nitrostyrene). [12] Examples of conducting polymer films include poly(pyrrole) (PPy), poly(aniline) (PA), and poly(thiophene) (PT). [12] EQCM become a powerful tool in surface analysis when QCM coupled with electrochemistry study.

1.7. Sputter Deposition

1.7.1. Introduction

Sputter deposition uses high-energy particles to bombard and to remove target material for deposition.[15] These high-energy particles are plasma, which are partially ionized gas consisting of anions, cations, electrons, and neutral gas molecules.[15] The

number of particles emitted from cathode target for each bombarding particle is the sputter yield (S), which is proportion to the product of the inert gas mass and the target mass.[15, 16]

$$S = P_e/P_i \quad (30)$$

$$= k\cdot(m_1\cdot m_2)/(m_1+m_2)^2 \quad (31)$$

, where S is the sputter yield, P_e is the number of emitted particles, P_i is the number of incident particles), k is the proportionality constant, m_1 is the mass of inert gas, and m_2 is the mass of target. The sputter yield is independent of the incident particle's charge, regardless whether the incident particle is an ion or an atom.[16] The physical sputtering relies only on the magnitude of kinetic energy of the incident particle.[16] The target material act as cathode, while substrate and vacuum chamber wall act as anode.[15]

1.7.2. Direct Current (DC) Diode Sputtering

The DC diode is the simplest sputter system.[15, 16] With adequate voltage and appropriate pressure, the feeding gas will breakdown into a plasma discharge.[16] Ions are accelerated rapidly toward the cathode and collide the target.[16] During this collision, secondary electrons are occasionally emitted from the surface.[15, 16] These electrons are accelerated back and collide with gas atoms to generate more ions.[16] The secondary electrons are the main energy source to sustain the plasma discharge.[16] However, the yield for secondary electrons is very low and is independent of ion energy.[16] DC diode can sputter conducting materials, but cannot sputter insulators.[16]

1.7.3. Radio Frequency (RF) Diode Sputtering

RF diode can sputter both conductors and insulators. The RF diode reverses the electric polarity of cathode and anode for a fraction of the RF cycle (Fig. 1-9), which eliminates charge buildup on an insulating surface.[16, 17] This oscillation of electric fields increases the path for electron movement within the plasma, thereby increases the probability of ionizing collision for a giving secondary electron and results in increasing the plasma density, ion currents, and sputtering rate.[16]

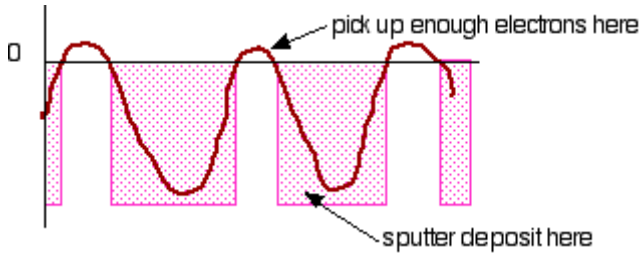

Figure 1-9: Radio frequency cycle of electric polarity on cathode.[17]

1.7.4. Magnetrons Sputtering

The cathode for magnetrons sputtering is either DC or RF diode.[16] Magnetron sputtering uses a static magnetic field at the cathode to trap secondary electrons near the cathode target surface (Fig. 1-10 and Fig. 1-11).[15, 16]

These secondary electrons collide with other electrons (electron heating) or with gas atoms (ionization), which results in a highly dense plasma in this drift ring.[16] In addition, ions made in the drift region can bombard the cathode and produce more secondary electrons and much denser plasma.[16]

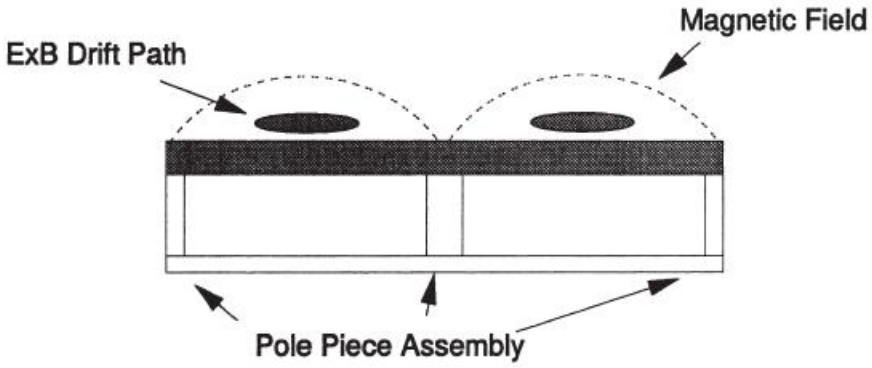

Figure 1-10: Side view of the magnetic field configuration for a circular planar magnetron cathode.[16]

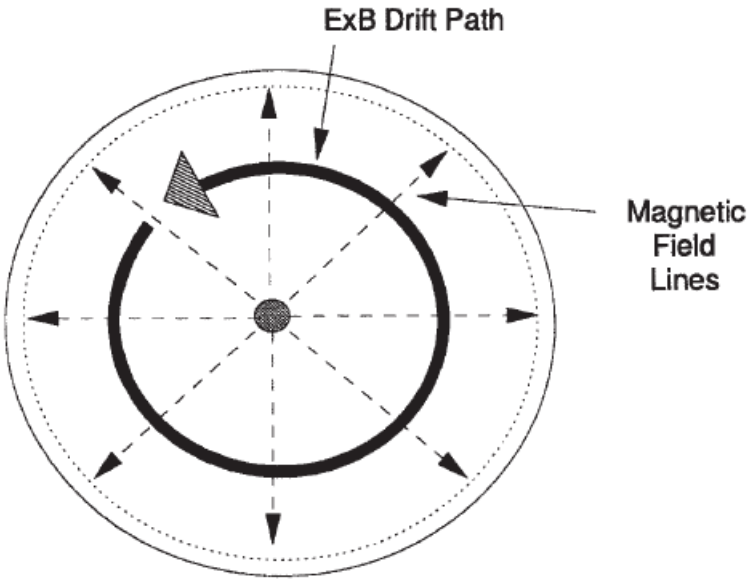

Figure 1-11: Top view of the magnetic field configuration for a circular planar magnetron cathode.[16]

The location of this drift ring is known as etch track due to the highest erosion of the cathode during sputtering in that location.[16] A deep groves can be seen on the cathode target after several sputtering events (Fig. 1-12). Magnetrons sputtering measures the discharge current (I) [16]

$$I = k \cdot V^n \quad (32)$$

, where I is the discharge current, V is the voltage, and k and n are system material and gas-dependant constants.[16] The coefficient n can be thought of as the efficiency factor.[16]

(a.) (b.)

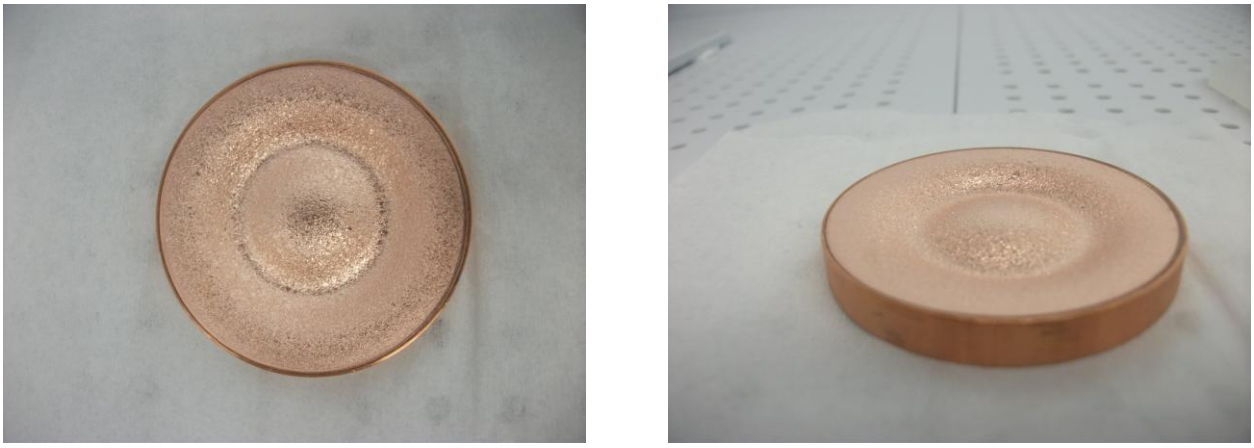

Figure 1-12: Pictures of copper (Cu) cathode target, which shows the etching track with deep groves on the cathode target. (a.) Top view of the Cu cathode target. (b.) Side view of the Cu cathode target.

1.8. References

1. Du, Y.; Wang, C. Preparation Ru, Bi monolayer modified Pt nanoparticles as the anode catalyst for methanol oxidation. *Mater. Chem. Phys.* **2009**, *113*, 927-932.
2. Chung, S.Y.; Uhm, S.H.; Lee, J.K.; Kang, S.J.; Tak, Y.S.; Lee, J.Y. Electrocatalytic Oxidation of HCOOH on Pt-based Anodes. *J. Ind. Eng. Chem.* **2007**, *13*, 339-344.
3. Schmidt, T.J.; Grgur, B.N.; Behm, R.J.; Markovic, N.M.; Ross, Jr. P.N. Bi adsorption on Pt(111) in perchloric acid solution--A rotating ring–disk electrode and XPS study. *Phys. Chem. Chem. Phys.* **2000**, *2*, 4379-4386.
4. Oh, I.; Gewirth, A.A.; Kwak, J. Electrocatalytic Dioxygen Reduction on Underpotentially Deposited Tl on Au(111) Studied by an Active Site Blocking Strategy. *Langmuir*. **2001**, *17*, 3704-3711.
5. Sudha, V.; Sangaranarayanan, M.V. Underpotential Deposition of Metals—Progress and Prospects in Modeling. *J. Chem. Sci.* **2005**, *117*, 207-218.
6. Herrero, E.; Buller, L.J.; Abruna, H.D. Underpotential Deposition at Single Crystal Surfaces of Au, Pt, Ag and Other Materials. *Chem. Rev.* **2001**, *101*, 1897-1930.
7. Shiue, W.J. Determination of trace copper by underpotential deposition-stripping voltammetry at nanoporous gold electrode. M.S. Thesis, National Cheng Kung University, Tainan, Taiwan, July 2006.
8. Zhu, W.; Yang, J.Y.; Zhou, D.X.; Bao, S.Q.; Fan, X.A.; Duan, X.K. Equilibrium Thermodynamics Analysis of Underpotential Deposition of Bi-Te Substrate System Thermoelectric Material. *Chemical Journal of Chinese Universities*. **2007**, *28*, 719-722.

9. *Handbook of Instrumental Techniques for Analytical Chemistry*, 1st ed. Settle, F., Ed.; Prentice Hall: Englewood Cliffs, NJ, 1997; Chapter 37, p 709.
10. Bard. A.J.; Faulkner, L.R. *Electrochemical Methods: Fundamentals and Applications*, 2nd ed.; John Wiley & Sons: Chicester, U.K., 2001; Chapter 6.
11. Single-Molecule and Nanobiology Laboratory. http://snl.bjmu.edu.cn/course/reviews/bitech/LvYalinT.pdf (accessed April 2011).
12. Buttry, D.A.; Ward. M.D. Measurement of Interfacial Processes at Electrode Surfaces with the EQCM. *Chem. Rev.* **1992**, *92*, 1355-1379.
13. Cheng, T.J.; Li, K.F.; Chang, H.C. The Principle and Application of Electrochemical Quartz Crystal Microbala. *Chemistry (The Chinese Chem. Soc., Taipei)*, **2001**, *59*, 219~233.
14. Rubinstein, I., Ed. *Physical electrochemistry: Principles, Methods, and Applications.* CRC Press: Boca Raton, FL, 1995; Chapter 7.
15. Applied Research Laboratory at Penn State. http://www.arl.psu.edu/capabilities/mm_mp_ct_sd.html (accessed April 2011).
16. *Handbook of Thin Film Deposition Processes and Techniques: Principles, Methods, Equipment and Applications,* 2nd Edition. Seshan, K., Ed.; Noyes: Norwich, NY, 2002; Chapter 8, p 319.
17. Physics of Thin Films—Sputter Deposition Techniques. http://www.uccs.edu/~tchriste/courses/PHYS549/549lectures/sputtertech.html (accessed April 2011).

CHAPTER 2

PROCEDURE FOR MAKING ELECTROCHEMICAL QUARTZ CRYSTAL MICROBALANCE ELECTRODE

2.1. Introduction

In this procedure, 7.995MHz AT-cut blank quartz crystals (SiO_2) were used to make electrochemical quartz crystal microbalance (EQCM) electrodes (Fig. 2-1 and Fig. 2-2). These blank quartz crystals were purchased from the International Crystal Manufacture.

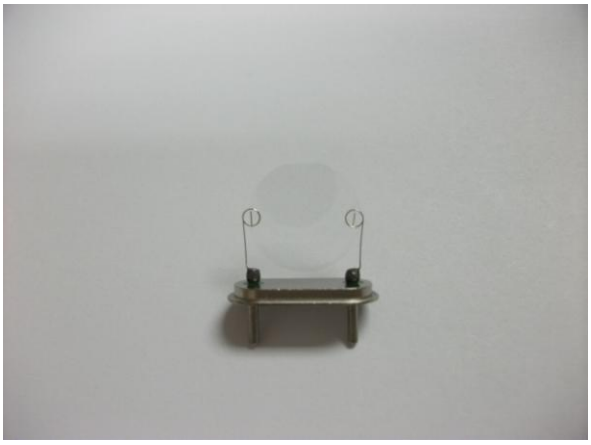

Figure 2-1: Blank AT-cut quartz crystal.

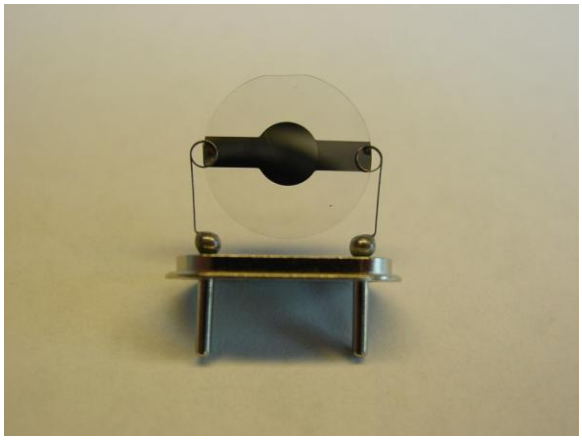

Figure 2-2: EQCM electrode.

In order to deposit a uniform metal on the quartz crystal, it is crucial to ensure the cleanness of the blank quartz crystals before metal deposition. Dichloromethane [$(CH_3)_2Cl_2$] is a powerful organic solvent to remove major organic contaminant. However, because the vapor pressure of dichloromethane is high (436 mmHg at 25°C [1]), it evaporates quickly and leaves organic residues on the quartz crystals surface. Care must be taken when handling dichloromethane (DCM). Long-term exposure of DCM can cause hepatitis. All organic cleaning procedures should be performed in a well-vented

hood. 2-propanol is used to remove minor organic contaminant. Because 2-propanol ($CH_3CH_2OHCH_3$) has a lower vapor pressure (44 mmHg at 25°C [2]), it evaporates slowly and leaves less organic residues on the quartz crystal surface. Then 200 proof ethanol (CH_3CH_2OH) is used to further remove organic residues. However, because ethanol evaporates quickly, ultra-pure Millipore H_2O (resistivity = 18.2 MΩ·cm) should be applied immediately after rinsing with ethanol to extend the evaporation time. During ultra-sonicate cleaning, Teflon tubes can place between quartz crystals to prevent inter-scratch of quartz crystals.

In the past, Cr was used as a priming layer. However, when the applied potential becomes more positive, Cr started to peel off. Since Ti has broader applied potential window than Cr does in both acidic and basic conditions (Fig. 2-3, Fig. 2-4, and Table 2-1), Ti is proven to be a better priming layer for glass (SiO_2).

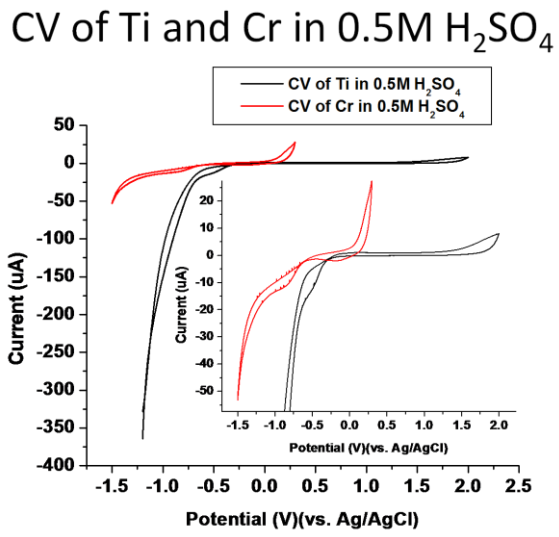

Figure 2-3: CV of Ti and Cr in 0.5M H_2SO_4.

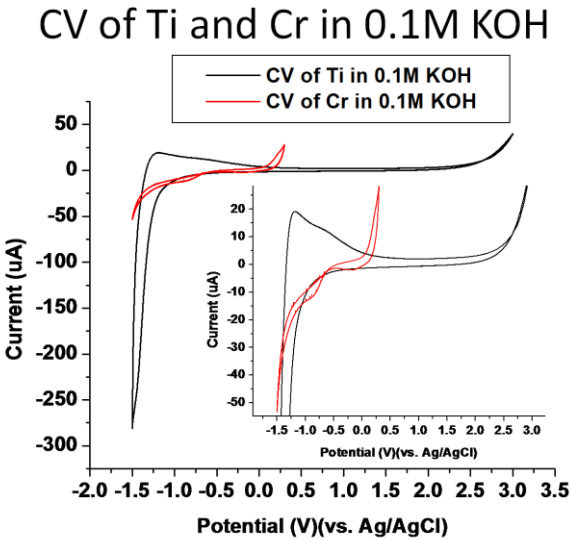

Figure 2-4: CV of Ti and Cr in 0.1M KOH.

Table 2-1: Working windows of Ti and Cr in 0.5M H_2SO_4 and in 0.1M KOH. Potentials in this table are with respected to Ag/AgCl.

	0.5M H_2SO_4 (pH 0)	**0.1M KOH (pH 13)**
Ti	[-0.5V, 2.0V]	[-1.0V, 2.5V]
Cr	[-0.5V, 0.8V]	[-0.8V, 0.2V]

From the four-point probe measurement, Ti with sputter time of 500s, which corresponds to 5 nm Ti thickness, shows a stable sheet resistivity (20 Ω/sq.) (Fig. 2-5). In this procedure, 5 to 10 nm of Ti is used as a priming layer on the quartz crystal. Then 100 nm of Ru is deposited on the Ti to make Ru EQCM electrode. The following procedures outline these cleaning steps in detail.

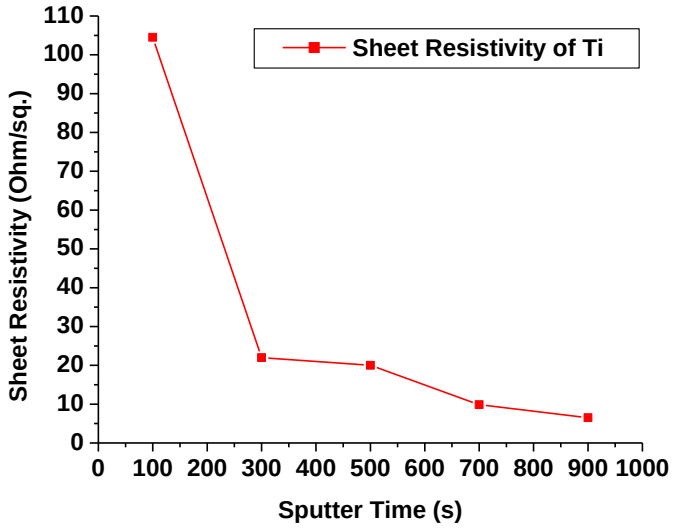

Figure 2-5: Sheet resistivity of Ti with different sputter time.

2.2. Procedure for Making Quartz Crystal Microbalance Electrode

2.2.1. Procedure for Cleaning Blank Quartz Crystals

With clean gloves and Teflon tweezers, rinse a blank quartz crystal carefully first with dichloromethane [$(CH_3)_2Cl_2$] then with 2-propanol ($CH_3CH_2OHCH_3$). Use Kimwipe to remove any visible dust and organic materials from the blank quartz crystal surface. Rinse the crystal again with 2-propanol and then with ultra-pure Millipore H_2O (18.5MΩ·cm). Dry it with $N_{2(g)}$ gas. Rinse it with ethanol (CH_3CH_2OH) and then with ultra-pure Millipore H_2O. Dry it with $N_{2(g)}$ gas. Do the same procedure for each blank quartz crystal.

In a clean beaker, place these cleaned quartz crystals between small Teflon tubes and ultra-sonicate in 2-propanol for 10 minutes (Fig. 2-6 and Fig. 2-7). Use Teflon tweezers to hold a ultra-sonicat cleaned quartz crystals. Rinse it with Millipore H_2O and dry it with $N_{2(g)}$ gas.

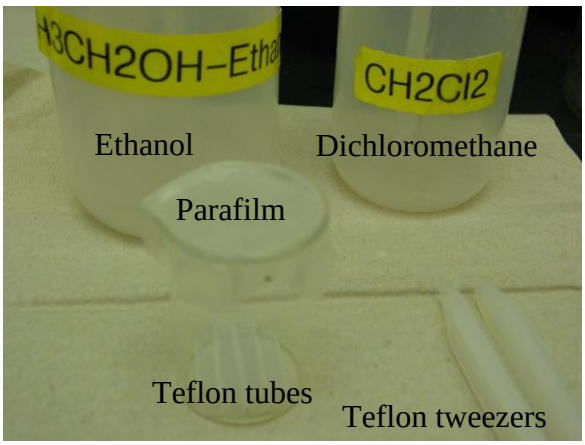

Figure 2-6: Tools for cleaning quartz crystals.

Figure 2-7: Ultra-sonicator.

Place the cleaned blank quartz crystal within the cuts of a clean sponge with the crystal-cut of the quartz crystal parallel to the surface of the sponge in order to minimize the contact area of the quartz crystal with the sponge (Fig. 2-8). Avoid the contact between the sides of quartz crystal with the sponge. These areas are for metal deposition and should avoid contamination. Do the same procedure for other ultra-sonicate cleaned quartz crystals.

Figure 2-8: Ultra-sonicate cleaned quartz crystals and cover slides stand within the sponge.

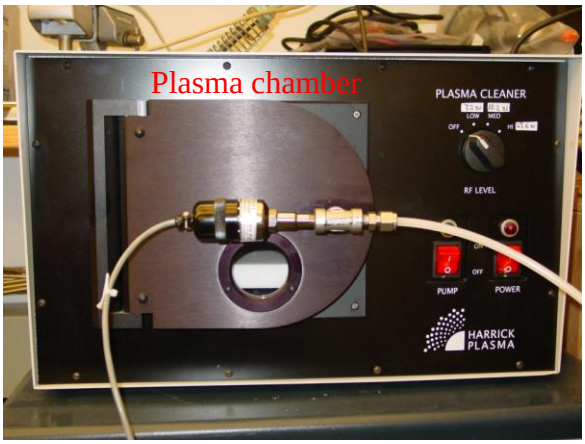

Figure 2-9: Harrick plasma cleaner.

Place the sponge along with these ultra-sonicate cleaned quartz crystals into a plasma chamber (Fig. 2-9 and Fig. 2-10). Use O_2 plasma to clean these quartz crystals for 30 minutes (Fig. 2-11). After O_2 plasma cleaned, temporarily keep these plasma-cleaned quartz crystals inside the plasma chamber.

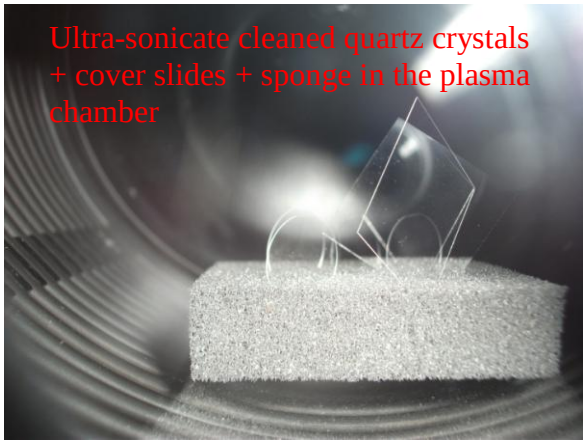

Figure 2-10: Before O_2 plasma cleaning.

Figure 2-11: O_2 plasma cleaning.

2.2.2. Procedure for Metal Deposition on Quartz Crystal

Gather the Fotofab QCM masks and spacer in clean room (Fig. 2-12). With clean gloves, take the QCM metal frame (Fig. 2-13) and place the QCM mask on the bottom piece of the metal frame (Fig. 2-14). Notice that the orientation of the flag on the QCM mask should point down. Then place the QCM spacer on the frame (Fig. 2-15). Notice that the orientation of the flat-cut on the QCM spacer should point to the right side. At this point, the numbers on the QCM spacer and on the QCM mask should overlap each other well. Carefully place the whole set on the magnetic base (Fig. 2-16).

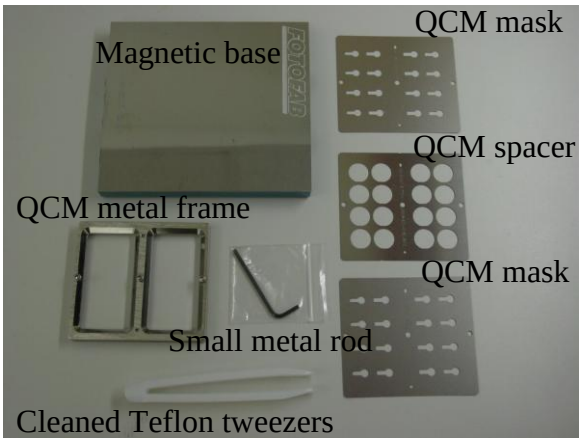

Figure 2-12: Fotofab QCM masks.

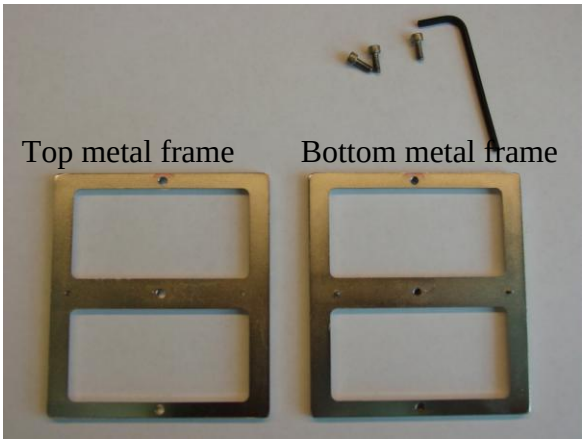

Figure 2-13: Top and bottom metal frames.

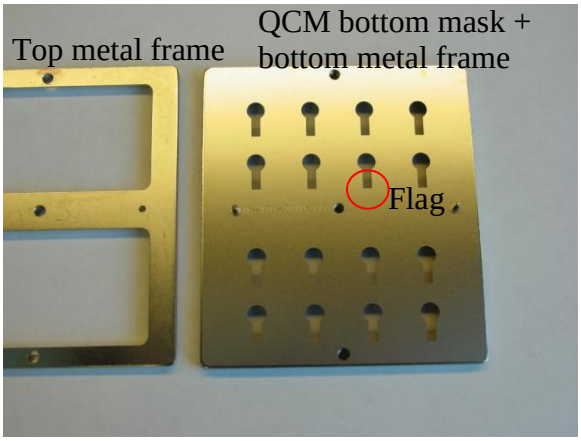

Figure 2-14: Bottom QCM mask.

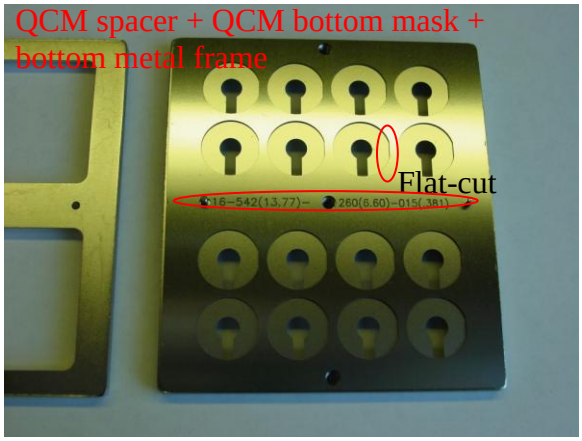

Figure 2-15: QCM spacer and bottom mask.

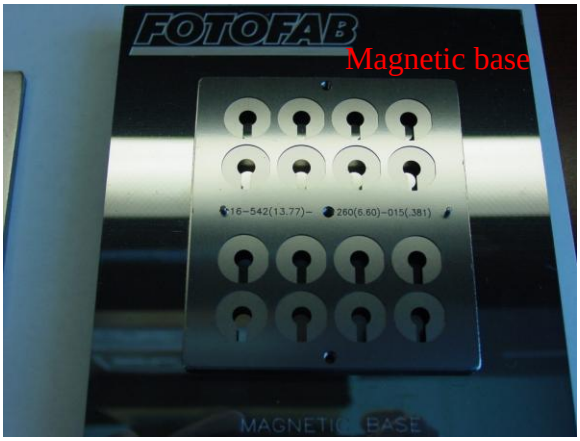

Figure 2-16: Place on the magnetic base.

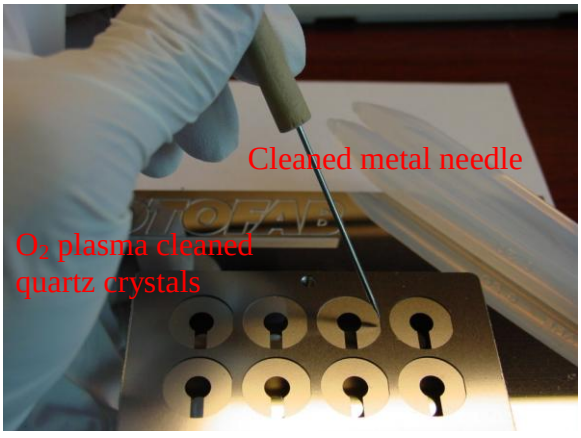

Figure 2-17: Place plasma-cleaned QCM quartz crystals in the QCM spacers.

Take out previous O_2 plasma cleaned quartz crystals from the plasma chamber and bring them into the clean room. With cleaned Teflon tweezers, carefully place the O_2 plasma cleaned quartz crystals in the QCM spacer. Make sure the crystal-cut on the quartz crystal is aligned well with the flat-cut on the QCM spacer. If needed, carefully use the tip of a cleaned metal needle to align the quartz crystal by touching the side of the quartz crystal (Fig. 2-17). Do the same procedure for other O_2 plasma cleaned quartz crystals. Place the top QCM mask on the set (Fig. 2-18). This time, notice the orientation of the flag on the top QCM mask should point up. Assemble the top piece of the QCM metal frame with the whole metal set (Fig. 2-19). Then carefully take the whole deposition set from the magnetic base (Fig. 2-20).

Figure 2-18: Place the top QCM mask.

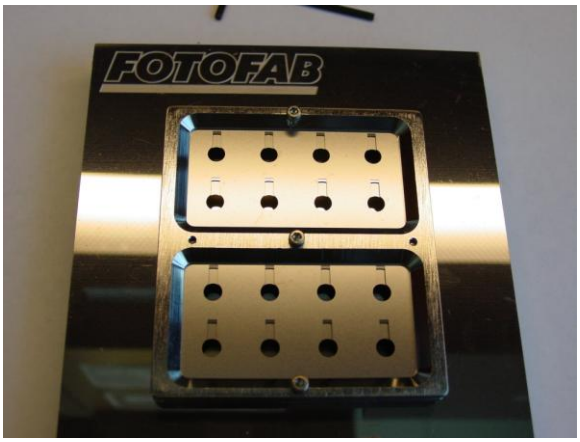

Figure 2-19: Place the top QCM metal frame.

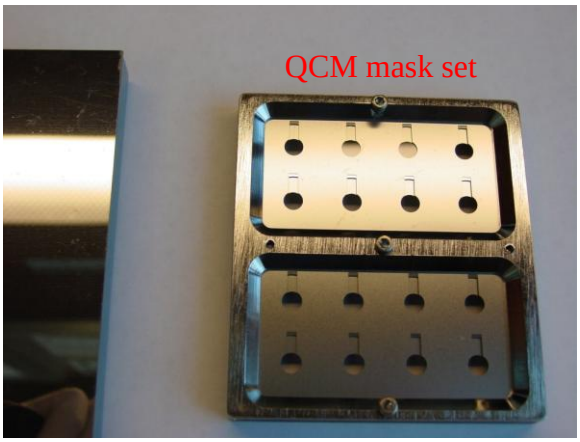

Figure 2-20: Remove from the magnetic base.

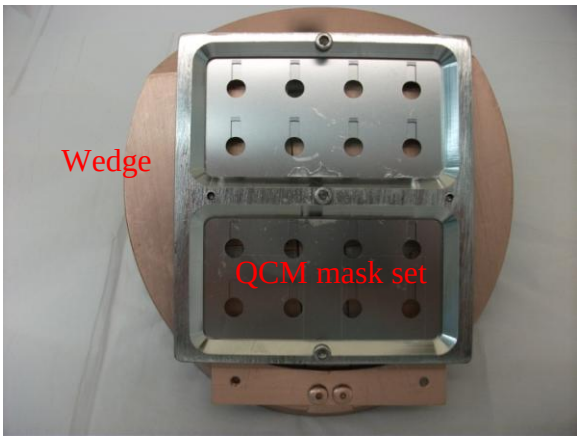

Figure 2-21: Place the mask set on the wedge.

Place the whole deposition set on a wedge and put it into the sputtering chamber (Fig. 2-21). Rotate the specimen table until the wedge surface is parallel to the sputter target (Fig. 2-22). Use the parameters in Table 2-2 for sputter deposition. After finishing sputtering, take out the QCM deposition mask set from the sputter chamber and bring them into the clean room. Carefully disassemble the top QCM deposition mask to see the EQCM electrodes (Fig. 2-23). With clean Teflon tweezers, slide an EQCM electrode into the EQCM metal holder (Fig. 2-24 and Fig. 2-25). Make sure the crystal cut of the EQCM electrode is point up and parallel to the base of the EQCM metal holder.

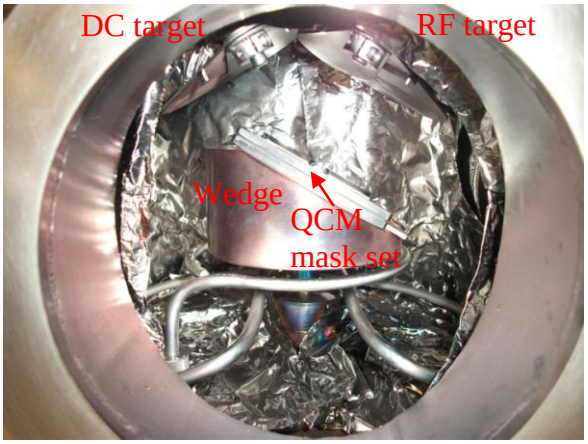

Figure 2-22: Place the wedge in the sputter machine.

Figure 2-23: EQCM electrodes.

Table 2-2: Sputter Deposition Parameters.

	RF Ti		RF Ru		DC Ru	
Wedge	Yes	No	Yes	No	Yes	No
Rotation	0 %	30 %	0 %	30 %	0 %	30 %
Power (W)	100 W	100 W	100 W	100 W	n/a	n/a
Current (mA)	n/a	n/a	n/a	n/a	270 mA	270 mA
Ar Pressure (mTorr)	5mTorr	5mTorr	5mTorr	5mTorr	5mTorr	5mTorr
Pre-Sputter Time (s) (Ar = 30 sccm)	30s	30s	30s	30s	30s	30s
Sputter Time (s) (Ar = 16 sccm)	100s	300s	200s	600s	200s	600s
Expected Deposit Thickness (nm)	5nm	5nm	100nm	100nm	100nm	100nm

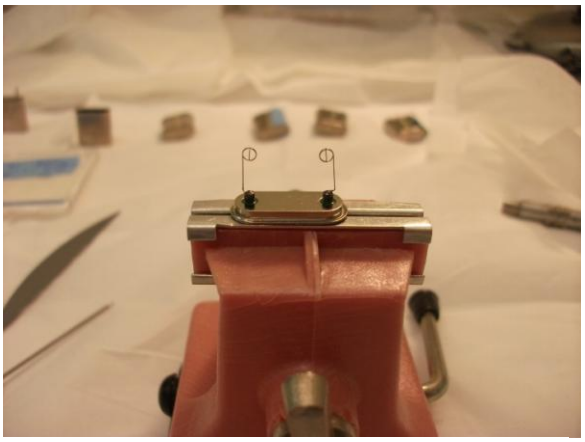

Figure 2-24: QCM holder.

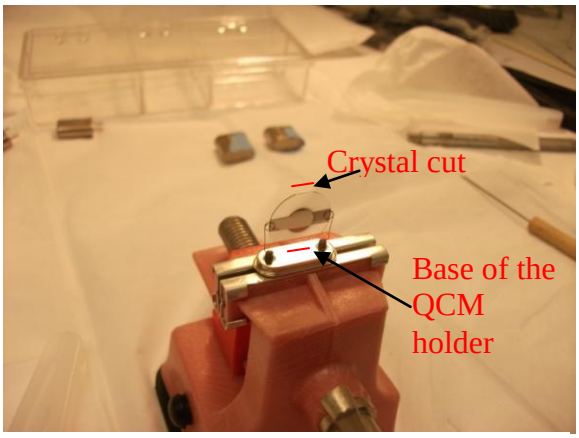

Figure 2-25: Slide the EQCM electrode in the QCM holder.

2.2.3. Procedure for Making Metal Connection

2.2.3.1. Method One: Silver Epoxy Connection

Gather the conductive Ag epoxy materials. Mix equal amounts of Ag epoxy (Part A) with Ag hardener (Part B) by the tip of a wood stick. Within 10 minutes after mixing, apply the mixed Ag epoxy inside the EQCM connection loop and on the EQCM electrode surface (Fig. 2-26). Allow the Ag epoxy to cure for 4 hours at room temperature. After 24 hours, the Ag epoxy will reach to the maximum properties and the EQCM electrode is ready to use.

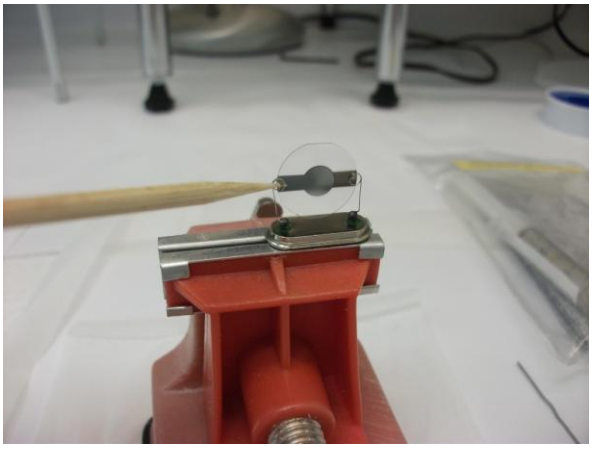

Figure 2-26: Apply Ag epoxy in the connection loop.

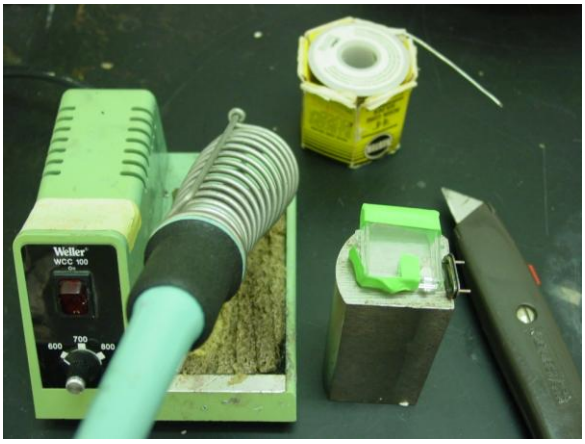

Figure 2-27: Soldering tools.

2.2.3.2. Method Two: Soldering Connection

In a well-vented hood, gather the soldering tools as in Fig. 2-27. Tape the sides of a clean small-hinged plastic box and leave one of the EQCM metal connection point to the air (Fig. 2-28 and Fig. 2-29). Make sure there is no hole in the box near the EQCM electrode to prevent the organic vapor of the resin core from contaminating the EQCM electrode surface. Cut a small piece of the soldering wire and place it inside the metal connection loop (Fig. 2-30 and Fig. 2-31). Turn on the soldering iron to 600°F and clean the iron surface before soldering (Fig. 2-32). Remember to add H_2O to moisture the sponge pad before cleaning the surface of the soldering iron. Slightly scratch off the oxide on the soldering iron with a knife and clean the iron surface with the moisture-sponge pad. Pre-heat the Ru EQCM metal surface inside the metal connection loop with the soldering iron, touch the soldering resin, and quickly slide through the loop (Fig.

2-33). Do the same procedure for the other side of the EQCM metal connection with new tapes on the box to prevent cross contamination of organic residue.

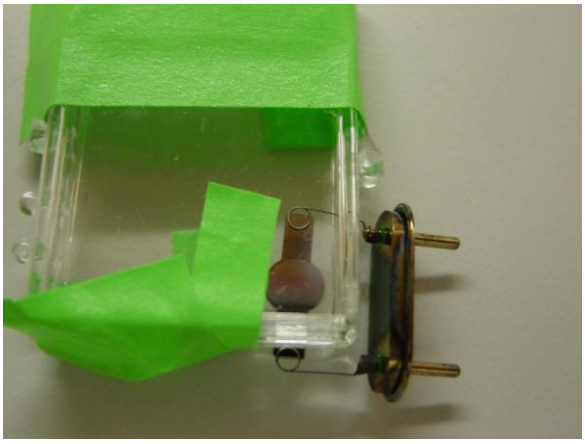

Figure 2-28: Soldering mask (top view).

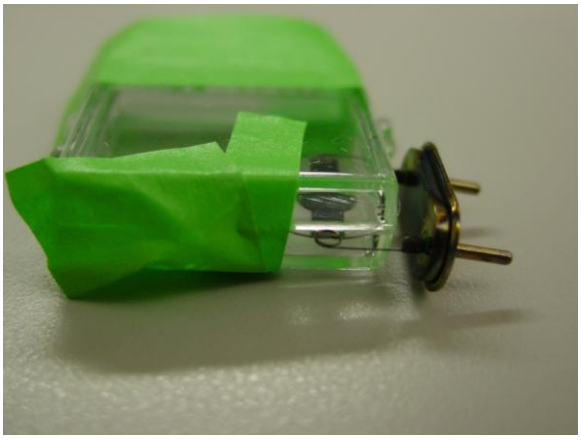

Figure 2-29: Soldering mask (side view).

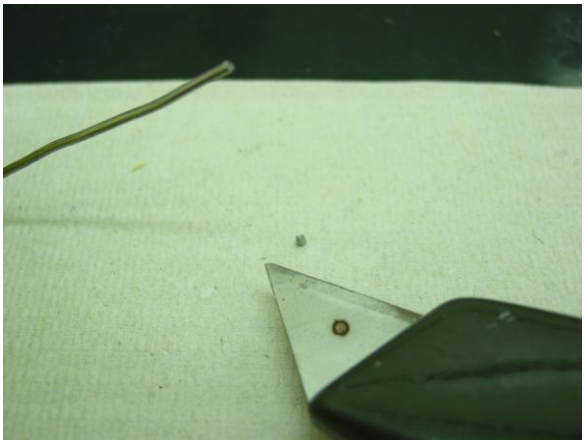

Figure 2-30: Cut a small piece of solder.

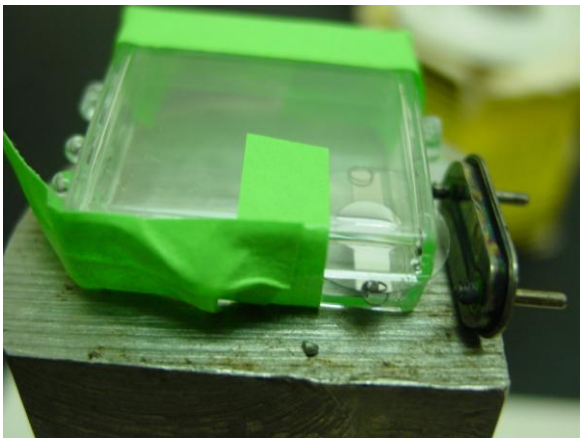

Figure 2-31: Place the solder inside the loop.

Figure 2-32: Clean the soldering iron.

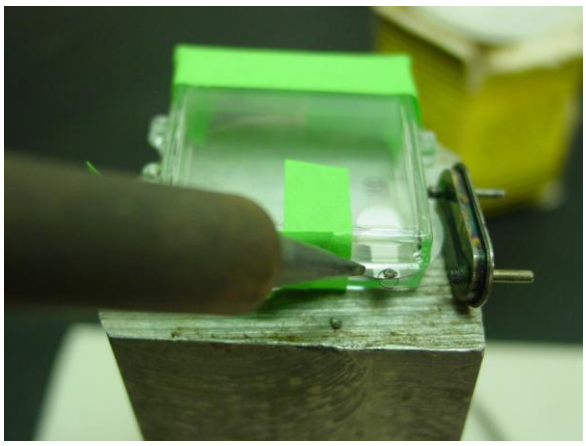

Figure 2-33: Touch the soldering material.

2.3. Assemble and Setup of EQCM Experiment

In the clean room, place a clean o-ring on a clean EQCM cell holder with clean gloves (Fig. 2-34). Place the EQCM electrode on the cell holder (Fig. 2-35). Make sure to keep some space between the cell holder and the EQCM metal contact. Carefully cover the Teflon base lid and evenly tighten in the screws (Fig. 2-36 and Fig. 2-37). Make sure the Ru EQCM electrode is in the center of the o-ring (Fig. 2-38). Cover the EQCM cell with a Teflon lid (Fig. 2-39).

Figure 2-34: Place an o-ring on the EQCM cell.

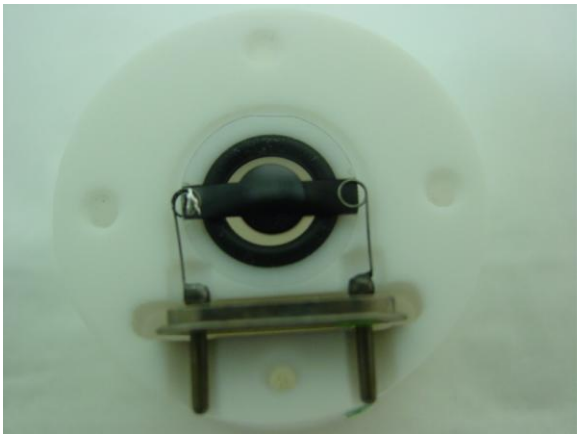

Figure 2-35: Place the EQCM electrode.

Figure 2-36: Place screws.

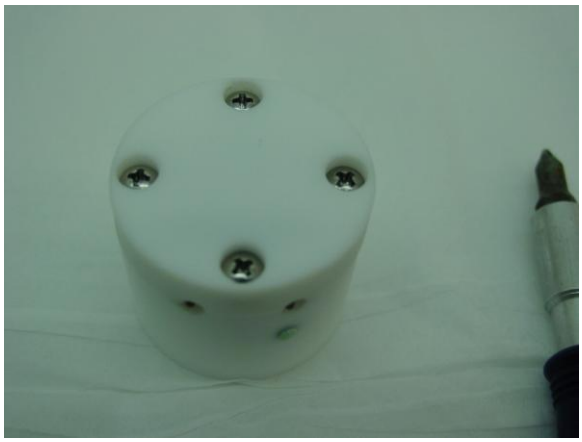

Figure 2-37: Tighten the screws.

Connect it to the CHI 440A EQCM oscillator (Fig. 2-40). Check the QCM frequency in air. The frequency drift should be ±1.0 Hz within 100s with noise level < 0.02 Hz. Add ultra-pure Millipore H_2O (18.2 MΩ·cm) in the EQCM cell and then connect a counter electrode and a reference electrode (Fig. 2-41 and Fig. 2-42). Wait for thermal equilibrium. It takes 4 hours to reach thermal equilibrium for EQCM in solution. Check the QCM frequency in solution. The frequency drift should be ±1.0 Hz within 1600s with noise level < 0.02 Hz.

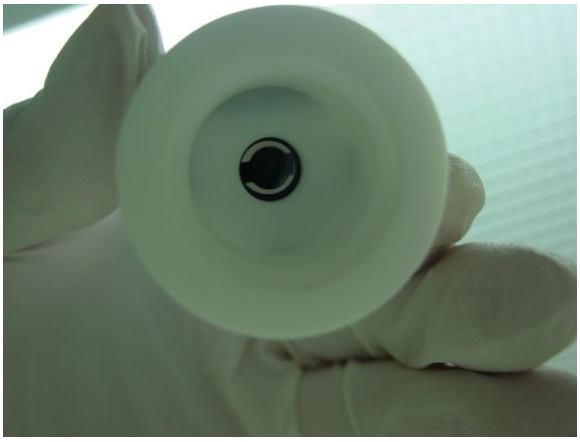

Figure 2-38: Check EQCM electrode in the center.

Figure 2-39: Cover with a lid.

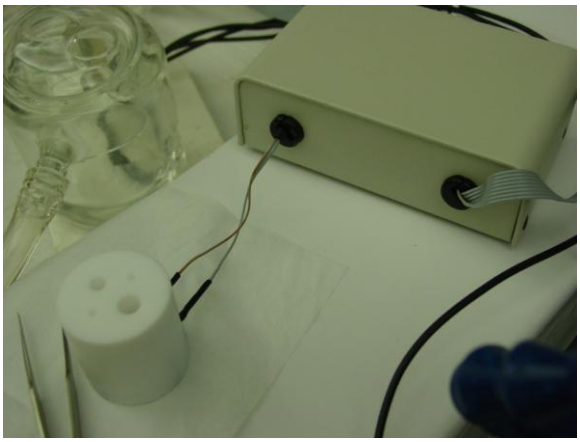

Figure 2-40: Connect it to the oscillator.

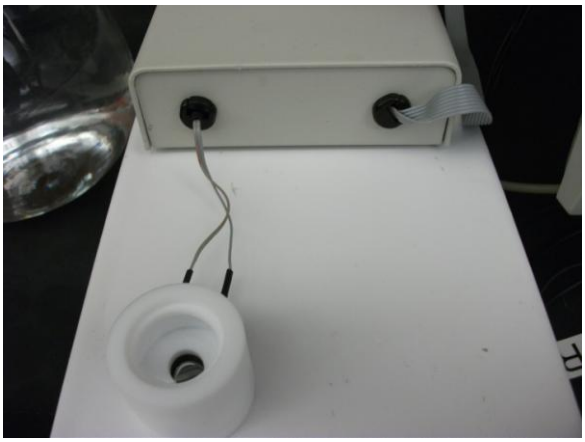

Figure 2-41: Add ultra-pure Millipore H_2O.

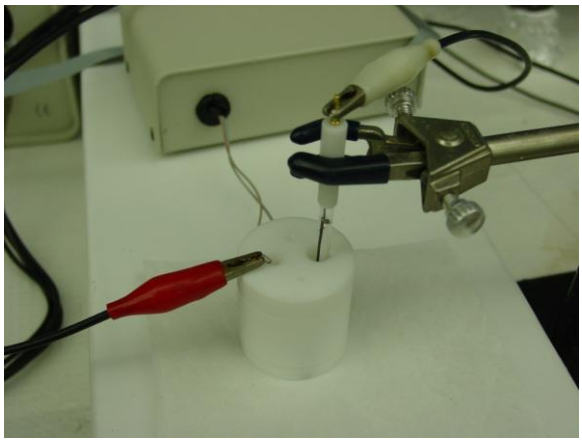

Figure 2-42: Connect a counter electrode and a reference electrode to the EQCM cell.

2.4. Procedure for Reclaiming Used Quartz Crystal

2.4.1. Remove Silver Epoxy Connection

With a blade, carefully scratch off the Ag epoxy from the metal connection (Fig. 2-43). Carefully slide the blade between the metal loops to separate Ag epoxy from the electrode surface. Do not touch the surface of the quartz crystal with the blade, or it will scratch the quartz surface. Separate the used EQCM electrode from the metal holder (Fig. 2-44). Use 600 grids sand paper to remove the oxide from the metal holder (Fig. 2-45). Do not apply too much pressure on the sand paper, or it may deform the metal loop. Place the used EQCM electrode in a concentrated sulfuric acid (H_2SO_4) for few days (Fig. 2-46). Then take the used EQCM electrode out and rinse with H_2O. On a solid flat surface, remove the Ag epoxy residue with a wetted cotton ball (Q-tip). Do not apply too much pressure with the cotton ball, or it will break the quartz. Repeat the same processes if needed.

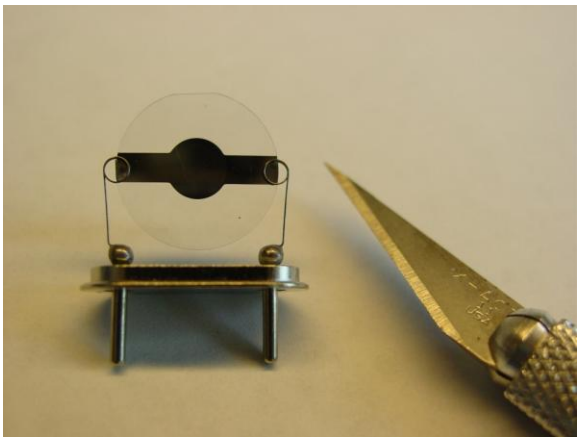

Figure 2-43: Remove the Ag epoxy by a blade.

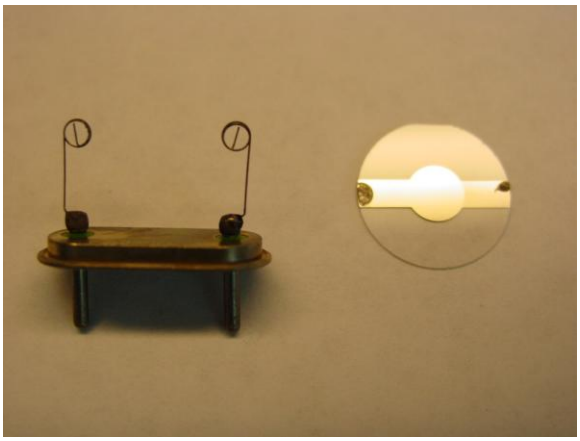

Figure 2-44: Remove quartz from the holder.

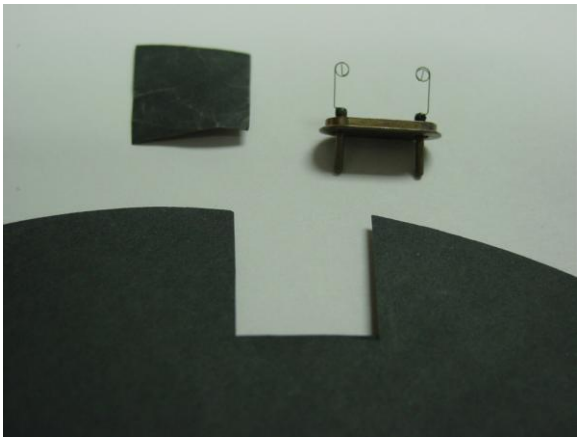

Figure 2-45: Remove metal oxide by a sand paper.

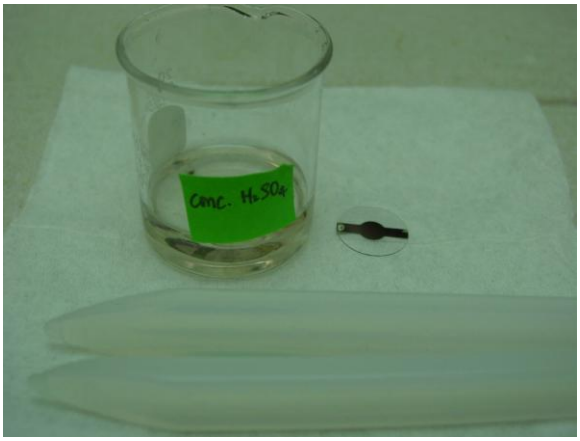

Figure 2-46: Place the quartz in conc. H_2SO_4.

2.4.2. Remove Soldering Connection

Use the Soldering iron to remove the soldering connection by slightly touching the soldering material in the EQCM metal connection. Repeat the same process for the other side of the soldering connection.

2.4.3. Remove Used EQCM Metals

After removing the Ag epoxy residues or the soldering material, place the used EQCM electrode into a freshly made aqua regia. Aqua regia is made by mixing concentrated hydrochloric acid (conc. HCl) with concentrated nitric acid (conc. HNO_3) with 3:1 volumetric ratio. In a well-vented hood, transfer conc. HCl into a small vial three times using Pasteur pipette (Fig. 2-47 and Fig. 2-48). Then transfer conc. HNO3 into the same vial one time using another Pasteur pipette (Fig. 2-49 and Fig. 2-50).

Figure 2-47: Transfer HCl 3 times by Pasteur pipette.

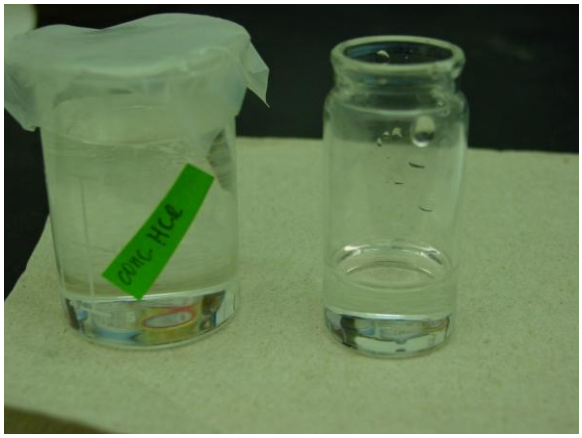

Figure 2-48: Concentrated HCl.

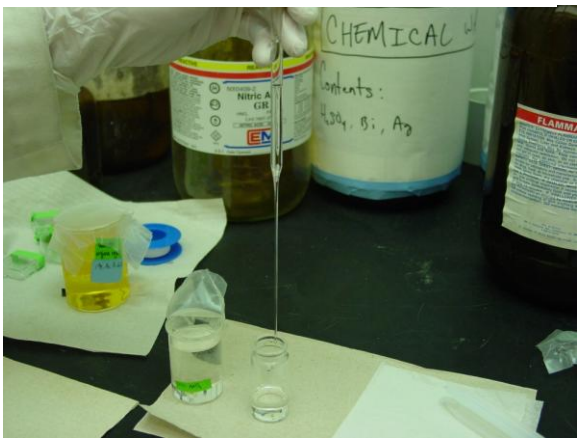

Figure 2-49: Transfer HNO_3 once by Pasteur pipette.

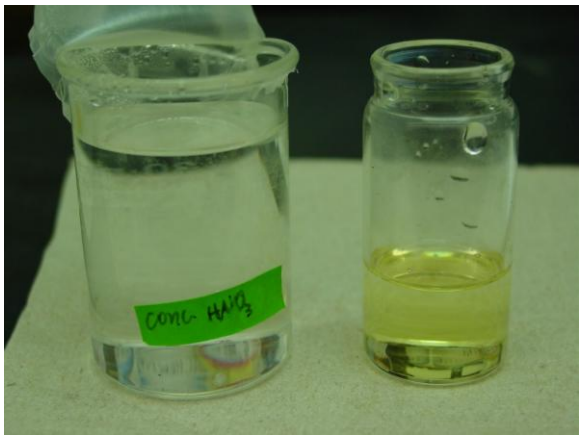

Figure 2-50: Freshly made aqua regia.

Place the used EQCM electrode into the aqua regia and immediately cover the vial with Parafilm (Fig. 2-51). Do not breathe the aqua regia vapor. The aqua regia should started changing color from transparent to light yellow, then to orange. After one week, place the used aqua regia into a waste aqua regia container. Use Teflon tweezers to take out the reclaimed QCM quartz crystal (Fig. 2-52). Rinse the QCM quartz crystal with H_2O, dry by Kimwipe, and store it in a clean container (Fig. 2-53).

Figure 2-51: Cover the vial with Parafilm.

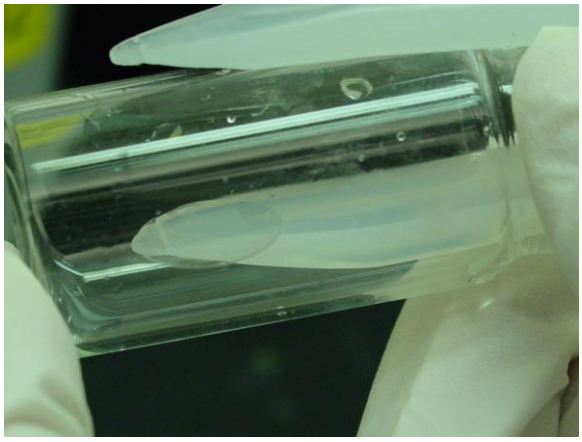

Figure 2-52: Take out the reclaimed quartz.

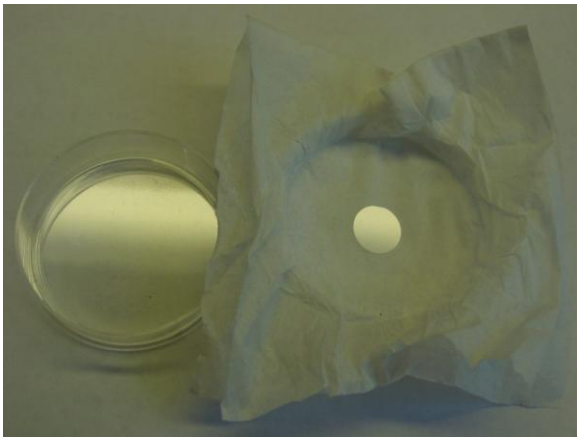

Figure 2-53: Store in a clean container.

2.5. References

1. OEHHA Water: Public Health Goals (PHGs).

   http://oehha.ca.gov/water/phg/pdf/dcm.pdf (accessed April 2011).

2. Kinetronics Corporation—Anti-Static Film Cleaning Brushes and Devices.

   http://kinetronics.com/PLCMSDSData.pdf (accessed April 2011).

CHAPTER 3

EQCM STUDY OF BISMUTH UNDERPOTENTIAL DEPOSITION ON RUTHENIUM AND ON ELECTROCHEMICALLY FORMED RUTHENIUM OXIDE

3.1. Introduction

Bismuth underpotential deposition on Ru was first discovered by Quiroz, Salgado, and Meas in 1988. [1] However, no one has done the electrochemical study of Bi UPD on Ru and Ru echem oxide by simultaneous recording the frequency change associated with Bi UPD and Bi bulk deposition on Ru and on Ru echem oxide since that time. Therefore, this experiment serves as an important foundation for further study on Bi-modified Ru or Ru echem oxide for potential fuel-cell catalysts.

3.2. Experimentation

All solutions are diluted by ultrapure Millipore H_2O (18.2 MΩ·cm). The 0.5M H_2SO_4 background solution is prepared from 96.2 % weight H_2SO_4 of Mallinckrodt Baker, Inc. The 1mM Bi UPD solution (Bi^{3+} solution) is prepared by dissolving $Bi(NO_3)_3 \cdot 5H_2O$ (made from Fisher Scientific Company) in 0.5M H_2SO_4 solution. EQCM study is performed using a CH 440A Instrument (from CH Instruments, Inc).

Three electrodes system is used throughout the experiments. Ru EQCM electrodes are made by magnetron sputter deposition as described in Chapter 2. A platinum (Pt) wire counter electrode and a reference electrode of either silver/silver chloride (Ag/AgCl) or a mercury/mercurous sulfate (Hg/Hg_2SO_4) are used. Before each experiment, the Ru EQCM electrode is electrochemically cleaned in 0.5M H_2SO_4 for several cycles until the cyclic voltammogram becomes stable. The electrochemically

formed Ru oxide (Ru echem oxide) EQCM electrode is prepared by progressive oxidation of Ru EQCM electrode in 0.5M H_2SO_4 solution with potential window of [-0.65, OCP] to [-0.65, 0.90], and then hold potential at 0.90 V (vs. Hg/Hg_2SO_4) for 1 min. The 2^{nd} time oxidation of Ru echem oxide EQCM electrode is prepared by holding potential at 0.90 V (vs. Hg/Hg_2SO_4) for additional 5 min. after the 1^{st} time oxidation of the Ru echem oxide EQCM electrode.

Open circuit potential (OCP) is used as initial applied potential for each experiment. For background CV of Ru and of Ru echem oxide, the final potentials are set to the cathodic potential limit to minimize surface oxidation. For Bi UPD study of Ru and of Ru echem oxide, the final potentials are set to the anodic potential limit to minimize residue of the Bi deposit on the EQCM electrodes. All experiments were performed at room temperature (around 73°F).

Assume the surface of the Ru EQCM electrode is smooth. The electrochemically active area of the Ru EQCM electrode is 0.2549 cm^2, and the QCM active area of the Ru EQCM electrode is 0.2043 cm^2. All cyclic voltammograms are plotted as potential (V) vs. current density ($\mu A/cm^2$). All frequency change (Δf) data from QCM are converted to mass change (Δm) data by Sauerbrey Equation, which is discussed in detail in Chapter 1. These mass change data are then converted to Bi monolayer (ML) coverage (Bi ML_{Mass}). The current density ($\mu A/cm^2$) are converted to charge density ($\mu C/cm^2$), which is used to calculate Bi monolayer (ML) coverage (Bi ML_{Charge}). All the cyclic voltammograms, Bi ML_{Mass}, and Bi ML_{Charge} are calculated from the 9^{th} and the 10^{th} segments unless specified in text.

The Bi ML coverage is calculated from van der Waals radius of Bi atom (20.7 nm [2]), and assumed the Bi monolayer on Ru or Ru echem oxide to be a close-packed ML coverage. The assumption of close-packed ML coverage with van der Waal radius gives 6.74×10^{14} Bi atoms/cm^2. One Bi ML_{Mass} has 233.87 ng/cm^2, and one Bi ML_{Charge} has 323.98 µC/cm^2.

3.3. Result and Discussion

3.3.1. Bi UPD on Ru (V vs. Ag/AgCl)

3.3.1.1. Progressive Cathodic Scan

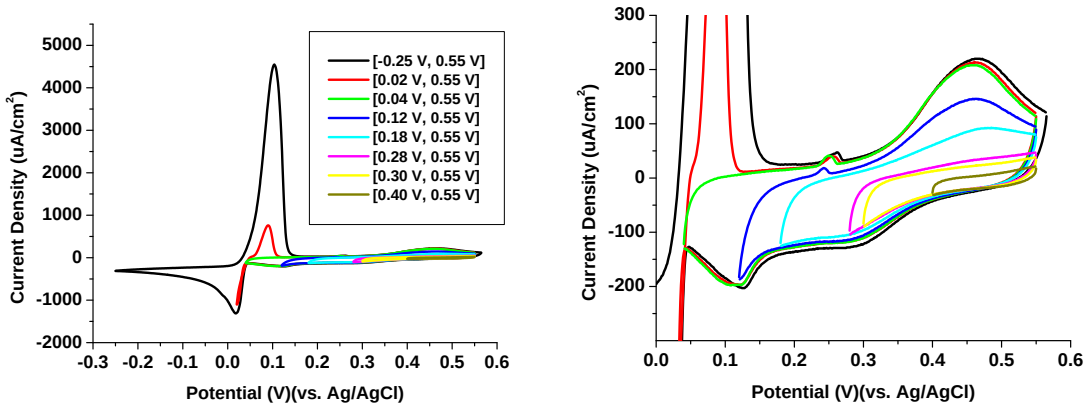

Figure 3-1: Progressive scan of Bi UPD on Ru in Bi^{3+} solution (1mM Bi^{3+} + 0.5M H_2SO_4). Scan range [x, 0.55 V](vs. Ag/AgCl). Scan rate of 50 mV/s.

Figure 3-1 demonstrates the Bi UPD on Ru substrate. When the cathodic potential scans to the 0.125 V (vs. Ag/AgCl), the Bi UPD stripping peak shows at 0.46 V (vs. Ag/AgCl). This indicates the Bi UPD on Ru at 0.125 V (vs. Ag/AgCl). The Bi bulk

deposition peak occurs at 0.018 V (vs. Ag/AgCl) and Bi bulk stripping peak occurs at 0.104 V (vs. Ag/AgCl). A small anodic stripping peak at 0.25 V (vs. Ag/AgCl) may indicate the redox couple of $RuCl_5^{2-}$ species. The Cl^- ion from the Ag/AgCl reference electrode reacts with the Ru surface causing this small anodic stripping peak. The reduction peak of the redox couple of the $RuCl_5^{2-}$ species overlaps with the Bi UPD peak. This increases the charge and current associated with the Bi UPD reduction peak potential. Therefore, the calculated Bi UPD monolayer (ML) based on charge would be higher than the true UPD monolayer coverage when using Ag/AgCl as reference electrode.

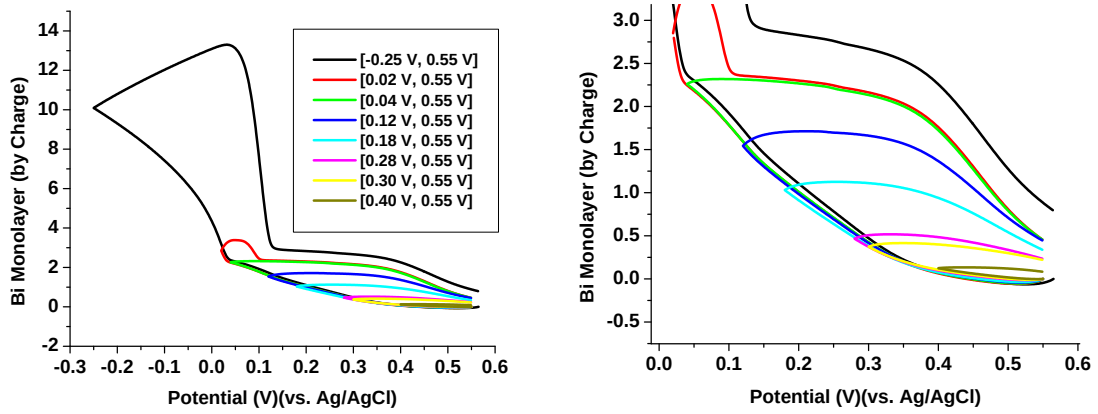

Figure 3-2: Progressive scan of Bi UPD on Ru in Bi^{3+} solution (1mM Bi^{3+} + 0.5M H_2SO_4). Scan range [x, 0.55 V](vs. Ag/AgCl). Scan rate of 50 mV/s. Bi monolayer (ML) calculated from charge vs. potential.

Figure 3-2 shows the calculated Bi monolayer coverage with different cathodic scanning windows from charge recorded from the previous progressive scan experiment. From this figure, the Bi UPD monolayer coverage increases as the cathodic potential limit extends to more negative potential. When the cathodic potential reaches

to 0.02 V (vs. Ag/AgCl), the Bi UPD monolayer seems to become stable (with 2.4 Bi ML). However, when the cathodic limit extended to Bi bulk deposition potential, the Bi UPD ML increases to a stable coverage of 2.95 Bi ML. This may indicate that the Ru surface is not fully covered by Bi adatoms before the cathodic potential limit reaches to the Bi bulk deposition potential (0.018 V vs. Ag/AgCl). The Bi UPD adatoms may not be 1:1 ratio adsorbed on the Ru substrate before the bulk deposition. The difference in the Bi UPD ML coverage (0.55 Bi ML) may indicate the partially exposed Ru atom surface with the Bi^{3+} ion before reaching the Bi bulk deposition potential. The background charging capacitance effect on the Bi UPD ML calculation may be another possible explanation for this discrepancy (0.55 Bi ML). In addition, the $RuCl_5^{2-}$ redox couple further complicates the Bi UPD ML calculation. With this in mind, a reference electrode without Cl^- ion is favored for the Bi UPD study on the Ru surface.

3.3.1.2. Progressive Anodic Scan

Figure 3-3 shows the effect of anodic potential limit on the Bi UPD on Ru surface. As the anodic potential limit becomes more positive, the Bi UPD reduction peak at 0.1 V (vs. Ag/AgCl) starts merging with the reduction peak (0.25 V vs. Ag/AgCl) of Ru reversible oxide. Although the Bi UPD reduction peak changes as the anodic potential limit increases, the Bi UPD stripping peak does not change. This indicates the Bi UPD monolayer coverage does not change when the potential scans to 0.90 V (vs. Ag/AgCl). During the anodic scan, the Bi UPD stripped completely while the Ru substrate undergoes oxidation. The Ru oxide may reduce to fresh Ru surface before or during the oxidation of the Bi UPD adatoms occurs.

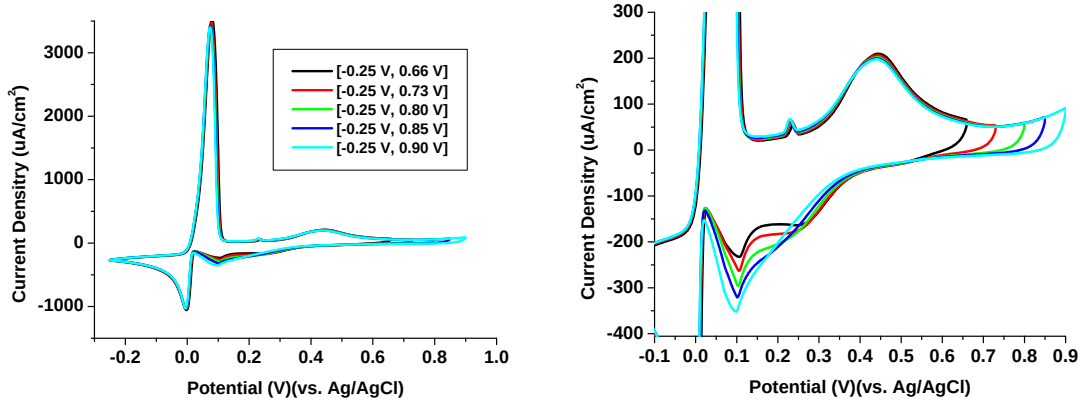

Figure 3-3: Progressive scan of Bi UPD on Ru in Bi^{3+} solution (1mM Bi^{3+} + 0.5M H_2SO_4). Scan range [-0.25, x V](vs. Ag/AgCl). Scan rate of 50 mV/s.

The reduction peak at 0.25 V (vs. Ag/AgCl) is the reduction of the reversible Ru oxide. Because the current in the cathodic scan contains reduction of $RuCl_5^{2-}$ redox couple and reduction of Ru oxide, the Bi UPD ML calculated from the cathodic charge may be higher than the true Bi UPD ML coverage. In addition, because the current in the anodic scan contains oxidation of Ru substrate, deoxygenated solution is favored for the Bi UPD studies to minimize the current associated with the oxidation of Ru substrate. Once the solution is deoxygenated, the Bi UPD ML calculated from the anodic stripping current will be closed to the true Bi UPD ML coverage.

Figure 3-4 shows the Bi monolayer coverage with different anodic potential limits. Bi UPD ML coverage calculated from cathodic charge ranges from 3.05 Bi ML to 3.75 Bi ML. Bi UPD ML coverage calculated from anodic charge ranges from 2.58 Bi ML to 3.31 Bi ML (with anodic ML correction).

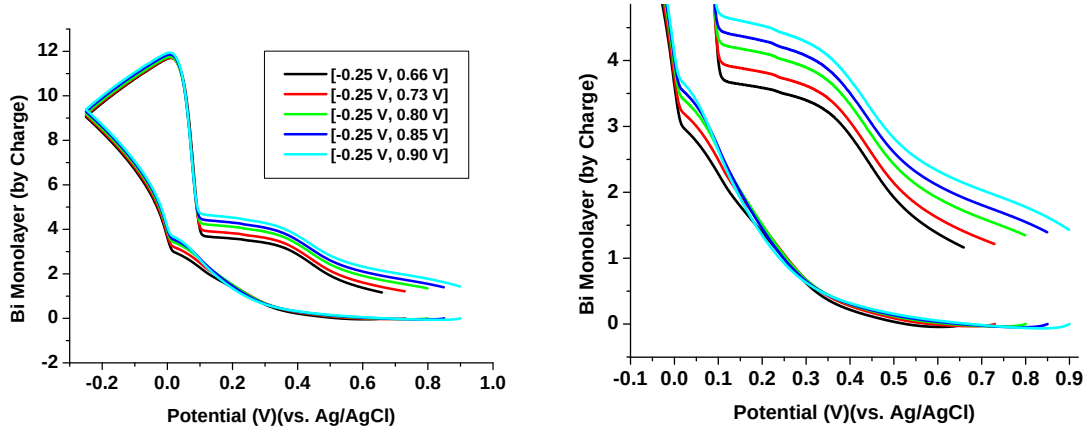

Figure 3-4: Progressive scan of Bi UPD on Ru in Bi^{3+} solution (1mM Bi^{3+} + 0.5M H_2SO_4). Scan range [-0.25, x V](vs. Ag/AgCl). Scan rate of 50 mV/s. Bi monolayer (ML) calculated from charge vs. potential.

This result supports previous prediction that the Bi UPD ML calculated from cathodic current is higher than the Bi UPD ML calculated from anodic current. Because Bi UPD reduction peak merges with the reduction of the $RuCl_5^{2-}$ redox species, the Bi UPD from cathodic current gives higher ML coverage than from anodic current. The Bi bulk ML does not affect by the anodic potential limit (10.5 Bi ML with anodic ML correction). The stable of Bi bulk ML coverage can also be predicted from Figure 3-3 because the Bi bulk current does not change as the anodic potential limit increases. This result gives the working window, [-0.25, 0.73](V vs. Ag/AgCl), for the Bi UPD on Ru when using Ag/AgCl reference electrode. The summary of Bi ML coverage in the progressive Bi UPD scan is in Table 3-1.

Table 3-1: Bi ML Coverage (by Charge) in Progressive Bi UPD Scan.

Scan Range (V vs. Ag/AgCl)	**Bi Bulk ML (with Anodic Mass Correction)**	**Bi UPD ML (Cathodic Mass with Cathodic Mass Correction)**	**Bi UPD ML (Anodic Mass with Anodic Mass Correction)**
[-0.25, 0.66]	10.534	3.05	2.58
[-0.25, 0.73]	10.503	3.27	2.78
[-0.25, 0.80]	10.412	3.50	2.96
[-0.25, 0.85]	10.460	3.64	3.13
[-0.25, 0.90]	10.521	3.75	3.31
Average	10.486	3.442	2.952
Standard Deviation	0.050	0.283	0.286

3.3.2. Background CV of Ru (V vs. Hg/Hg_2SO_4)

3.3.2.1. Progressive Scan

Figure 3-5 shows the progressive scan of Ru in the background solution (0.5M H_2SO_4) with Hg/Hg_2SO_4 reference electrode. Figure 3-5 (a.) is used to find the cathodic potential limit and Figure 3-5 (b.) is used to find the anodic potential limit. The reduction peak of Ru in Figure 3-5 (a.) overlaps well with other cathodic limit scans. However, the reduction peak of Ru in Figure 3-5 (b.) starts to deviate from other peaks when the anodic limit scans over 0.20 V (vs. Hg/Hg_2SO_4). When the anodic potential scans over 0.30 V (vs. Hg/Hg_2SO_4), the reduction peak for the Ru oxide starts shifting to more negative potential. Therefore, the working window for the Ru with Hg/Hg_2SO_4 reference electrode in the background solution is found to be [-0.65, 0.20](V vs. Hg/Hg_2SO_4),

which is closely related to the working window with Ag/AgCl reference electrode, [-0.25, 0.73](V vs. Ag/AgCl).

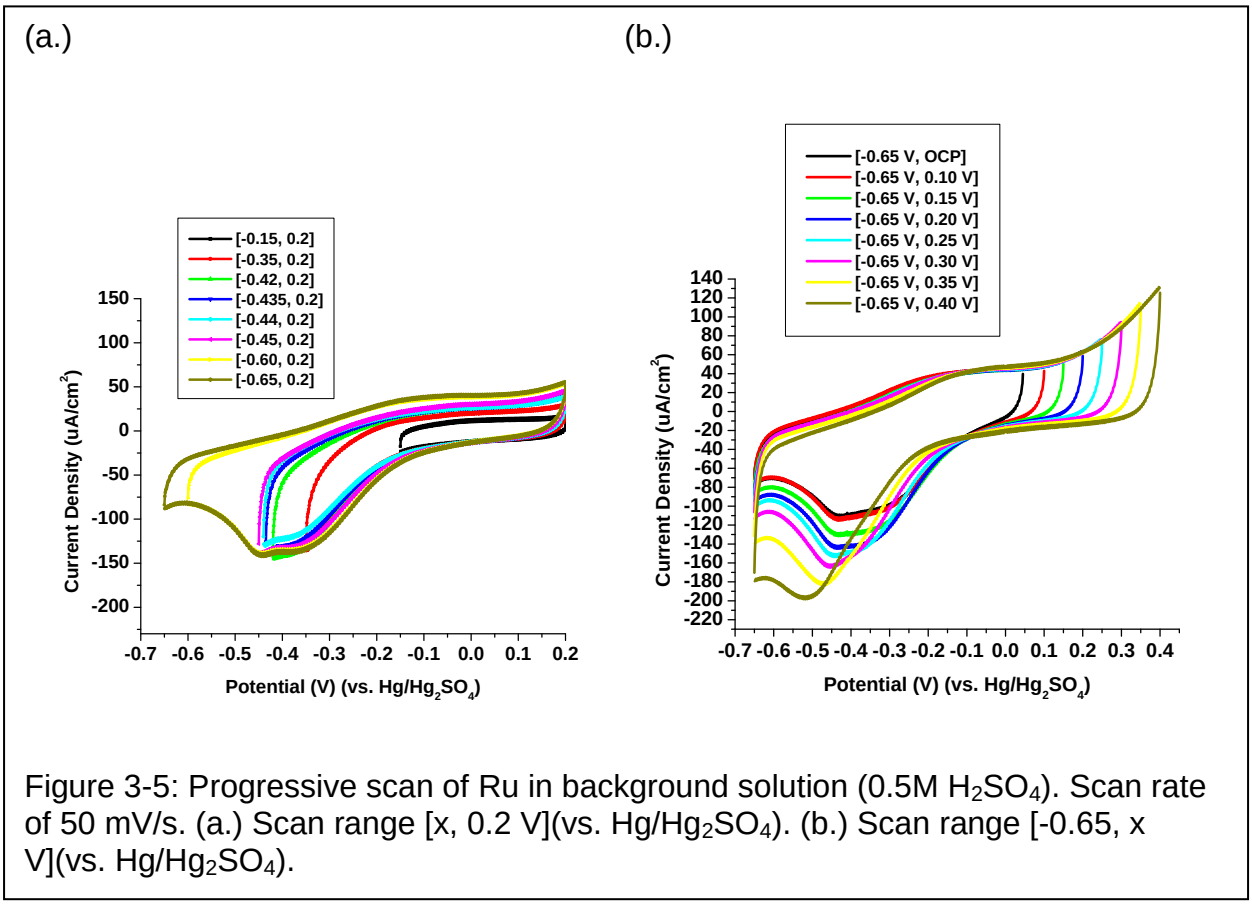

Figure 3-5: Progressive scan of Ru in background solution (0.5M H_2SO_4). Scan rate of 50 mV/s. (a.) Scan range [x, 0.2 V](vs. Hg/Hg_2SO_4). (b.) Scan range [-0.65, x V](vs. Hg/Hg_2SO_4).

To account the background effect on the Bi UPD ML calculation, the background current for Ru is converted to equivalent Bi ML coverage as shown in Figure 3-6 (b.) and Figure 3-7 (b.), and the background frequency change for Ru is converted to equivalent Bi ML coverage by mass as shown in Figure 3-6 (a.) and Figure 3-7 (a.). The scale for both Bi ML by mass and Bi ML by charge in Figure 3-6 and Figure 3-7 are set to the same range in order to perform parallel analysis.

(a.) (b.)

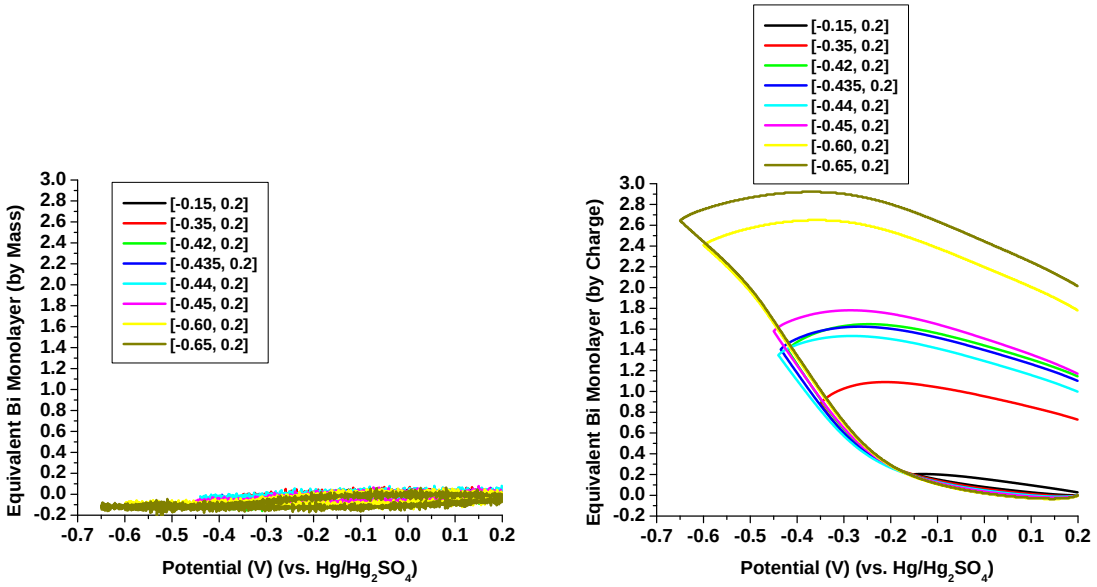

Figure 3-6: Progressive cathodic scan of Ru in background solution (0.5M H_2SO_4) with scan range [x, 0.2 V](vs. Hg/Hg_2SO_4). Scan rate of 50 mV/s. (a.) Equivalent Bi monolayer coverage calculated from mass. (b.) Equivalent Bi monolayer coverage calculated from charge.

Figure 3-6 shows the equivalent Bi ML coverage calculated from frequency change and from charge for the progressive cathodic scan [x, 0.20](V vs. Hg/Hg_2SO_4). In [-0.65, 0.20](V vs. Hg/Hg_2SO_4) working window, the equivalent Bi ML calculated from frequency change is within 0.12 Bi ML, and the equivalent Bi ML calculated from charge is within 2.93 Bi ML.

(a.)

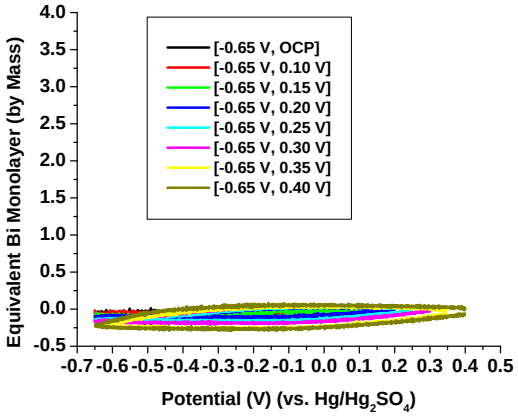

(b.)

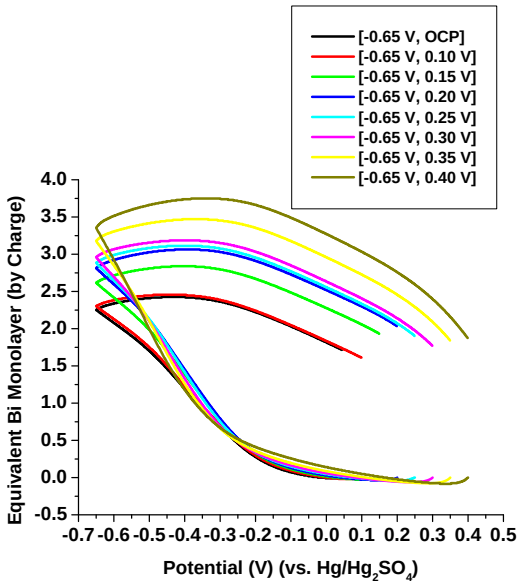

Figure 3-7: Progressive anodic scan of Ru in background solution (0.5M H_2SO_4) with scan range [-0.65, x V](vs. Hg/Hg_2SO_4). Scan rate of 50 mV/s. (a.) Equivalent Bi monolayer coverage calculated from mass. (b.) Equivalent Bi monolayer coverage calculated from charge.

Figure 3-7 shows the equivalent Bi ML coverage calculated from frequency change and from charge for the progressive anodic scan [-0.65, x](V vs. Hg/Hg_2SO_4). In [-0.65, 0.40](V vs. Hg/Hg_2SO_4) working window, the equivalent Bi ML calculated from frequency change is within 0.32 Bi ML, and the equivalent Bi ML calculated from charge is within 3.74 Bi ML.

3.3.2.2. Progressive Oxidation

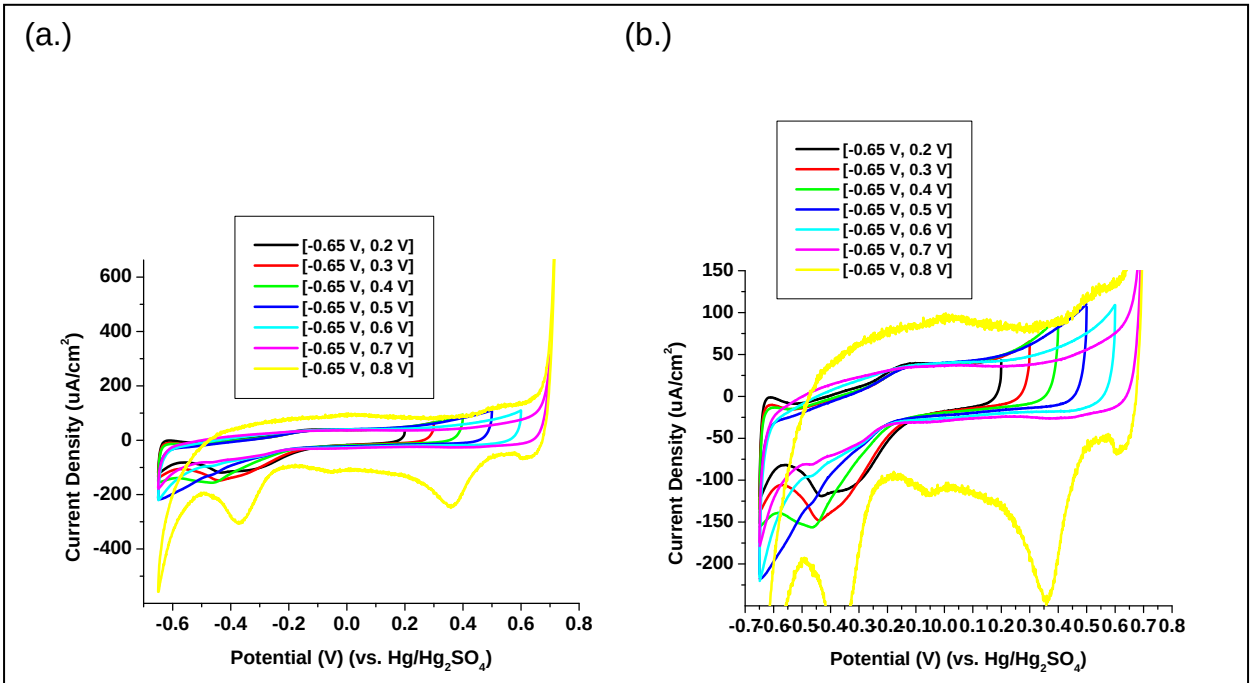

Figure 3-8: (a.) Progressive oxidation of Ru in background solution (0.5M H_2SO_4) with scan range [-0.65, x V](vs. Hg/Hg_2SO_4). Scan rate of 50 mV/s. (b.) A closer look at the reduction region.

Figure 3-8 shows the progressive oxidation of Ru in the background solution (0.5M H_2SO_4) with scan range [-0.65, x](V vs. Hg/Hg_2SO_4). The two broad reduction peaks at -0.43 V and -0.33 V (vs. Hg/Hg_2SO_4) merges into one reduction peak at -0.45 V (vs. Hg/Hg_2SO_4) with anodic potential limit of 0.4 V (vs. Hg/Hg_2SO_4). When the anodic potential scans over 0.4 V (vs. Hg/Hg_2SO_4), the reduction peak starts decreasing and shifting to more negative potential. When the anodic potential reaches to 0.6 V (vs. Hg/Hg_2SO_4), the reduction peak is almost disappeared. This may indicate that the Ru surface changes and gradually becomes unreducible when the anodic potential scans

above 0.4 V (vs. Hg/Hg_2SO_4). However, the shape of anodic scan does not change greatly until the potential limit reaches to 0.68 V (vs. Hg/Hg_2SO_4).

Oxygen evolution starts to occur when the anodic potential scans above 0.7 V (vs. Hg/Hg_2SO_4). When the anodic potential reaches the oxygen evolution potential, 0.75 V (vs. Hg/Hg_2SO_4), the feature of reduction peaks is different from other Ru reduction peaks feature. The capacitance current increases when the anodic potential scans to 0.8 V. This indicates irreversible Ru oxide has formed on the Ru surface. Reduction peaks at 0.608 V, 0.359 V, -0.050 V, -0.371 V, and -0.65 V (vs. Hg/Hg_2SO_4) with oxidation peaks at 0.019 V and 0.537 V (Hg/Hg_2SO_4) is observed. The different number of reduction peaks to the oxidation peaks in scan range [-0.65, 0.80](V vs. Hg/Hg_2SO_4) clearly indicates an irreversible redox process on the Ru surface.

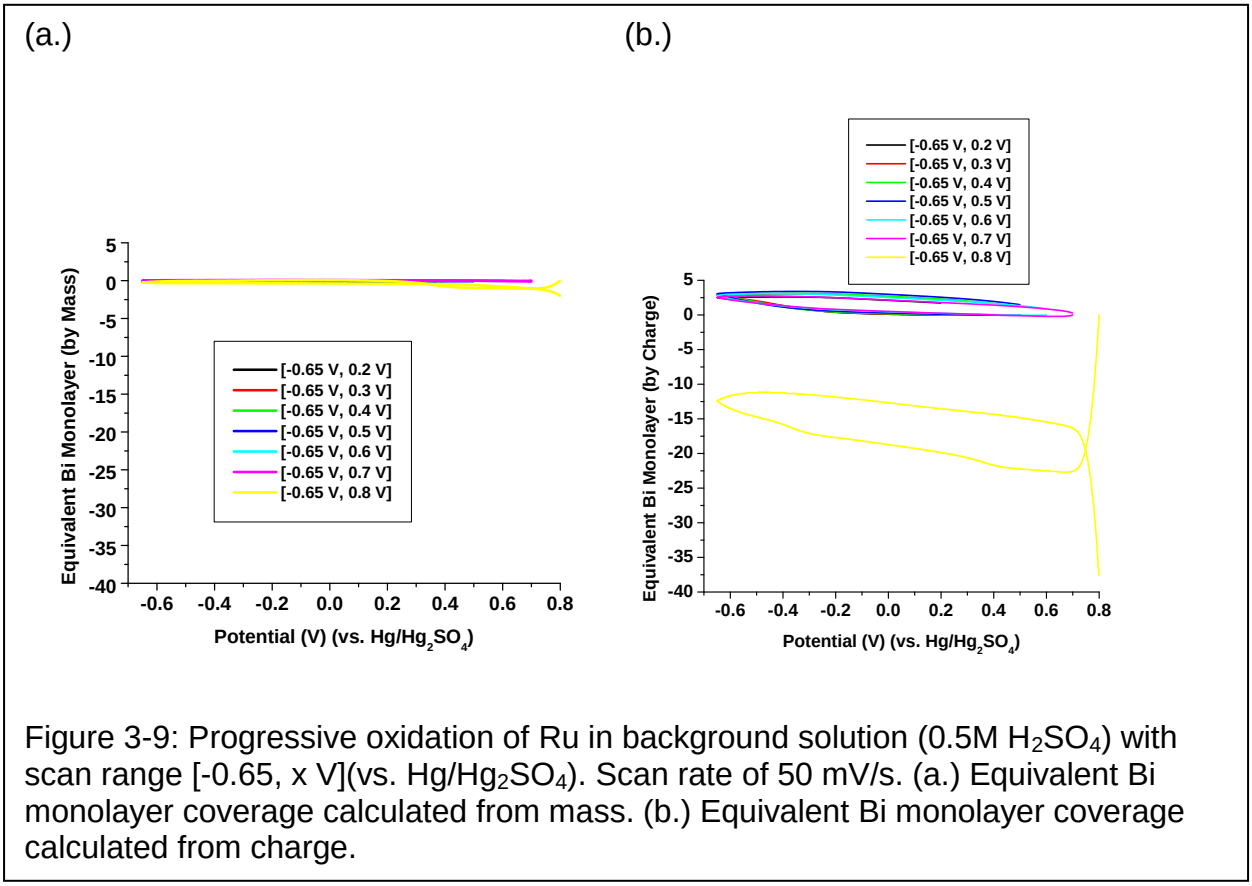

Figure 3-9: Progressive oxidation of Ru in background solution (0.5M H_2SO_4) with scan range [-0.65, x V](vs. Hg/Hg_2SO_4). Scan rate of 50 mV/s. (a.) Equivalent Bi monolayer coverage calculated from mass. (b.) Equivalent Bi monolayer coverage calculated from charge.

To account the background effect on the Bi UPD ML calculation, the background current for Ru is converted to equivalent Bi ML coverage as shown in Figure 3-9 (b.), and the background frequency change for Ru is converted to equivalent Bi ML coverage by mass as shown in Figure 3-9 (a.). The scale for both Bi ML by mass and Bi ML by charge in Figure 3-9 are set to the same range in order to perform parallel analysis.

Figure 3-9 shows the equivalent Bi ML coverage calculated from frequency change and from charge for the progressive anodic scan [-0.65, x](V vs. Hg/Hg_2SO_4). In [-0.65, 0.20](V vs. Hg/Hg_2SO_4) working windows, the equivalent Bi ML calculated from frequency change is within 0.085 Bi ML, and the equivalent Bi ML calculated from charge is within 2.586 Bi ML.

Table 3-2: Summary of the Equivalent Bi ML for the Progressive Oxidation of Ru in 0.5M H_2SO_4.

Scan Range (V vs. Hg/Hg_2SO_4)	**Equivalent Bi ML Range (by Mass)**	**Equivalent Bi ML (by Mass)**	**Equivalent Bi ML (by Charge)**
[-0.65, 0.20]	-0.079 to -0.006	0.085	2.586
[-0.65, 0.30]	-0.111 to 0.020	0.131	3.035
[-0.65, 0.40]	-0.146 to 0.035	0.181	3.132
[-0.65, 0.50]	-0.146 to 0.036	0.182	3.399
[-0.65, 0.60]	-0.045 to 0.051	0.096	3.048
[-0.65, 0.70]	-0.131 to 0.085	0.216	2.740
Average	-0.110 to 0.037	0.149	2.990
Standard Deviation	0.041 to 0.030	0.053	0.289
[-0.65, 0.80]	-1.977 to 0.084	2.057	37.512

In [-0.65, 0.60](V vs. Hg/Hg_2SO_4) working window, the equivalent Bi ML calculated from frequency change is within 0.096 Bi ML, and the equivalent Bi ML calculated from charge is within 3.048 Bi ML. In [-0.65, 0.70](V vs. Hg/Hg_2SO_4) working window, the equivalent Bi ML calculated from frequency change is within 0.216 Bi ML, and the equivalent Bi ML calculated from charge is within 2.740 Bi ML. The summary of the equivalent Bi ML both from mass and from charge is in Table 3-2.

3.3.3. Bi UPD on Ru (V vs. Hg/Hg_2SO_4)

3.3.3.1. Background vs. Bi UPD

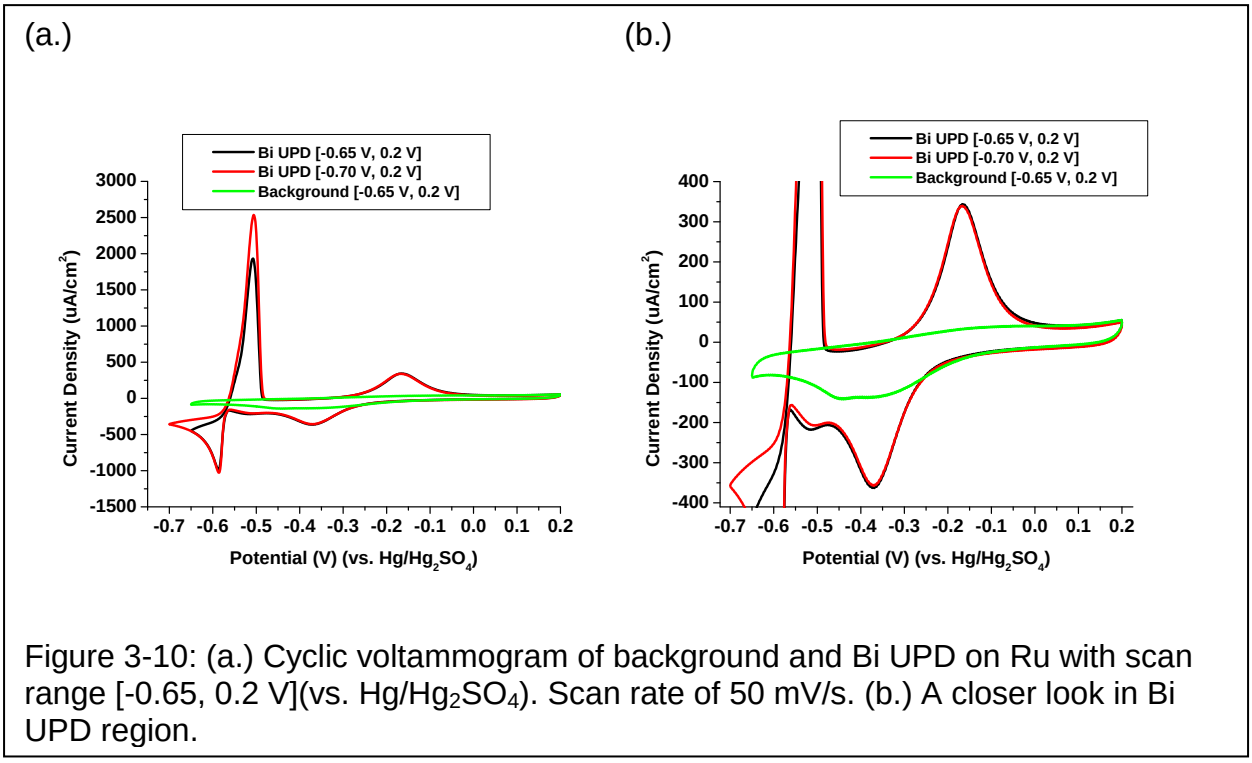

Figure 3-10: (a.) Cyclic voltammogram of background and Bi UPD on Ru with scan range [-0.65, 0.2 V](vs. Hg/Hg_2SO_4). Scan rate of 50 mV/s. (b.) A closer look in Bi UPD region.

Figure 3-10 compares the background CV and Bi deposition CVs on Ru. When comparing Bi deposition and background CVs in [-0.65, 0.20](V vs. Hg/Hg_2SO_4), the

peaks indicates the Bi UPD and Bi bulk redox peaks. When comparing the CVs of [-0.65, 0.20] and [-0.70, 0.20](V vs. Hg/Hg_2SO_4), the elevation of peak height in anodic current ($I_{anodic\ peak}$) indicates Bi bulk stripping peak. This gives the Bi-bulk reduction peak at -0.586 V (vs. Hg/Hg_2SO_4) and Bi-bulk oxidation peak at -0.506 V (vs. Hg/Hg_2SO_4). Note that the constant peak height for the redox peaks at more positive potential strongly indicates the Bi UPD redox peaks. The Bi UPD reduction peaks locate at -0.37 V and -0.506 V (vs. Hg/Hg_2SO_4), and the Bi UPD oxidation peak locates at -0.166 V (vs. Hg/Hg_2SO_4). The cathodic current increases near -0.57 V during cathodic scan indicates the surface has been completely covered by Bi UPD adatoms, and the surface is significantly different from the fresh Ru surface.

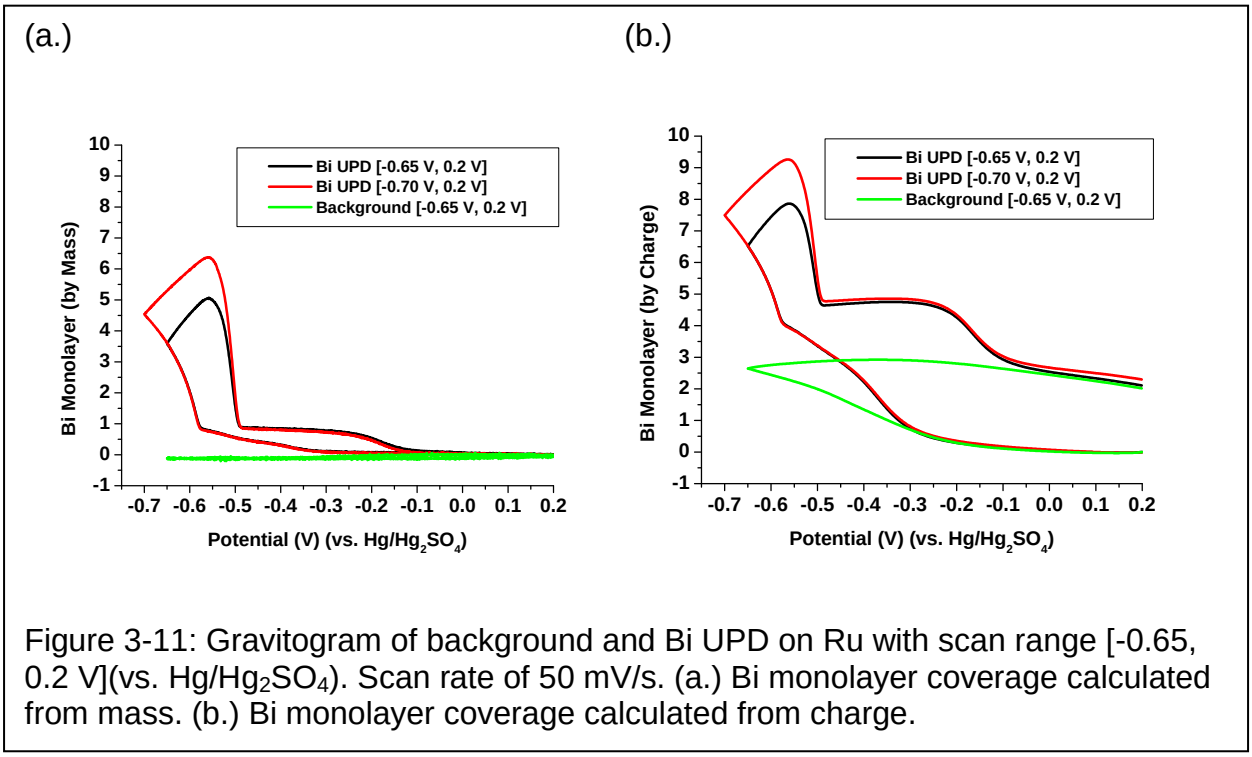

Figure 3-11: Gravitogram of background and Bi UPD on Ru with scan range [-0.65, 0.2 V](vs. Hg/Hg_2SO_4). Scan rate of 50 mV/s. (a.) Bi monolayer coverage calculated from mass. (b.) Bi monolayer coverage calculated from charge.

Figure 3-11 shows the Bi monolayer coverage during Bi deposition on Ru. Approximate one Bi monolayer (0.85 Bi ML) in Bi UPD region and five Bi monolayer (5.05 Bi ML) in Bi bulk region within [-0.65, 0.20](V vs. Hg/Hg_2SO_4) when calculating Bi ML from frequency change [Figure 3-11 (a.)]. When the cathodic scan extend to [-0.70, 0.20](V vs. Hg/Hg_2SO_4), 6.38 Bi ML is in Bi bulk region.

After subtracting the charge from Ru background in Figure 3-11 (b.), approximate 1.80 Bi monolayer in Bi UPD region and 5.07 Bi monolayer in Bi bulk region within [-0.65, 0.20](V vs. Hg/Hg_2SO_4). With charge correction in anodic background, approximate 5.94 Bi monolayer is in Bi bulk region within [-0.70, 0.20](V vs. Hg/Hg_2SO_4).

After Ru background correction, the Bi bulk ML coverage calculated from mass and from charge are almost the same, but the Bi UPD ML coverage is about 1 Bi ML different. This may indicate other electron transfer process in the Bi UPD region. One possible explanation may be the reaction of submonolayer Bi adatoms with oxygen or other solvent molecule. Another explanation may be that the Bi adatoms enhance the electron transfer process from the Ru electrode surface to the solution. This increase in current density may support the catalytic property of Bi UPD adatoms on Ru surface. Notice that the Bi UPD adatoms may not be 1:1 ratio adsorbed on Ru surface. Since this discrepancy in Bi ML coverage does not observe in the Bi bulk region, the interface between the partially exposed Ru atom with Bi submonolayer adatoms may play a role in this catalytic enhancement.

However, without subtracting the charge from Ru background in Figure 3-11 (b.), 2.55 Bi monolayer (with anodic charge correction) in Bi UPD region and 5.76 Bi

monolayer (with anodic charge correction) in Bi bulk region is calculated within [-0.65, 0.20](V vs. Hg/Hg_2SO_4).

In addition, without subtracting the charge from Ru background in Figure 3-11 (b.), 2.50 Bi monolayer (with anodic charge correction) in Bi UPD region and 6.67 Bi monolayer (with anodic charge correction) in Bi bulk region is calculated within [-0.70, 0.20](V vs. Hg/Hg_2SO_4).

This result indicates that the Bi ML coverage by charge without Ru background subtraction will give additional 0.75 Bi monolayer in Bi UPD region and additional 0.70 Bi monolayer (0.69 to 0.73 Bi ML) in Bi bulk region. The result is summarized in Table 3-3.

Table 3-3: Summary of Bi ML Coverage on Ru.

	Background Subtraction	**[-0.65, 0.20](V vs. Hg/Hg_2SO_4)**	**[-0.70, 0.20](V vs. Hg/Hg_2SO_4)**
Bi Bulk ML	No	5.76	6.67
	Yes	5.07	*5.94
Bi UPD ML	No	2.55	2.50
	Yes	1.80	*1.42

<Note>: * means background subtraction based on [-0.65, 0.20](V vs. Hg/Hg_2SO_4) background.

3.3.3.2. Bi UPD on Ru

(a.) (b.)

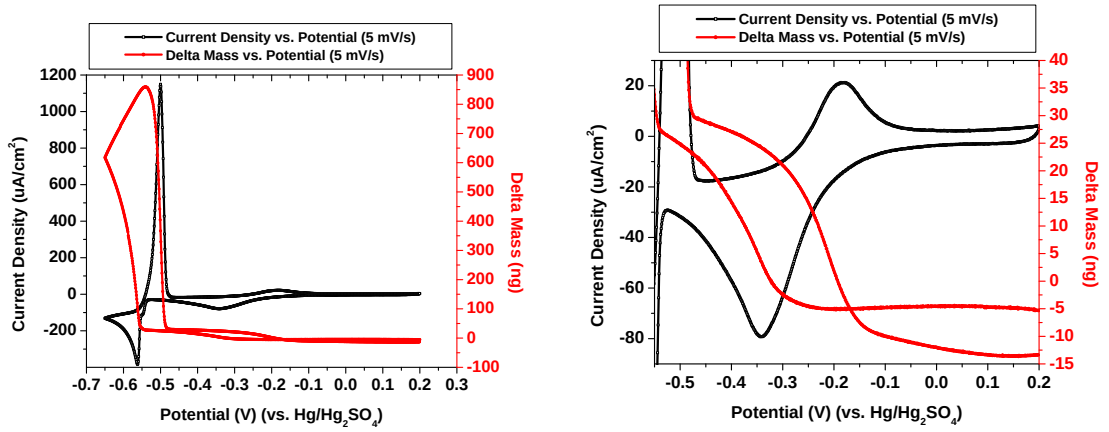

Figure 3-12: Double y-plot of Bi UPD on Ru with scan range [-0.65, 0.20](V vs. Hg/Hg_2SO_4). Scan rate of 5 mV/s. (a.) Overview of Bi bulk and Bi UPD on Ru. (b.) A closer look at the Bi UPD region.

Figure 3-12 overlaps the CV with mass respond of Bi UPD on Ru. In the cathodic scan, the onset potential for mass increases in Bi UPD region is at -0.217 V (vs. Hg/Hg_2SO_4), but the onset potential for the reduction current is at -0.022 V (vs. Hg/Hg_2SO_4). This difference in the onset potential of Bi UPD from mass responds and current may be caused by the coulomb attraction of Bi^{3+} ion near the Ru surface, thereby increase the concentration of Bi^{3+} ion near the electrode surface and increase in current before initiating of Bi underpotential deposition on Ru. Another possible explanation for this early onset potential for Bi UPD reduction current may indicate the overlapping region of the oxygen reduction reaction (ORR) region, reduction of Ru oxide, and Bi underpotential deposition region.

The maximum Bi UPD reduction current at -0.340 V (vs. Hg/Hg_2SO_4) locates coincident with the reflection point of mass increase in the Bi UPD region indicates the maximum rate of Bi underpotential deposition. The exposed-site of fresh Ru surface for Bi adatom adsorption is decreasing during the Bi UPD on Ru. After -0.340 V in the cathodic scan, the relative surface area of fresh Ru surface to the Bi adatoms reaches to a limiting point that makes the subsequent Bi UPD adatoms harder to deposit on the Ru surface. This effect is the same as if the concentration of Bi^{3+} ion near the Ru electrode surface starts depleting, which require to apply higher reduction energy (more negative potential) to increase the concentration of Bi^{3+} ion near the electrode surface to keep the constant reaction rate. This causes the cathodic current starts decreasing.

The onset potential for mass increases in Bi bulk region is at -0.536 V (vs. Hg/Hg_2SO_4), which corresponds to the onset potential of Bi bulk reduction current at -0.532 V (vs. Hg/Hg_2SO_4). The slightly delay in the onset current of Bi bulk deposition may indicates a brief coulomb attraction for the Bi^{3+} ion near the surface immediately after the first layer of Bi UPD adatoms has formed on the Ru surface.

The maximum reduction peak current occurs at -0.562 V (vs. Hg/Hg_2SO_4). This may indicate the concentration of Bi^{3+} ion at the electrode surface has reached to a maximum concentration, and the maximum rate of the Bi bulk deposition occurs. The increase in cathodic current with negligible mass increase during the cathodic scan from -0.532 V to -0.562 V (vs. Hg/Hg_2SO_4) may indicate the coulomb attraction of Bi^{3+} ion onto the Bi adatom-modified Ru surface and increase the concentration of Bi^{3+} ion near the electrode surface. In addition, the sharp increases in the cathodic current near -

0.562 V (vs. Hg/Hg_2SO_4) may also indicate the coverage of the partially exposed Ru surface with Bi adatoms and the initial of the Bi deposition on the Bi adatoms surface.

The mass and reduction current keep increasing at the cathodic scan after scanning over -0.532 V (vs. Hg/Hg_2SO_4). At the reverse scan (anodic scan), the mass keeps increasing and reach the maximum mass at anodic potential of -0.541 V (vs. Hg/Hg_2SO_4), which is the same potential when the current starts become positive current (anodic current).

The mass decrease sharply immediately after anodic potential of -0.541 V (vs. Hg/Hg_2SO_4) indicates the initiation of the Bi bulk stripping. The maximum anodic current occurs at -0.500 V (vs. Hg/Hg_2SO_4), which is approximate the reflection point of the curvature from the mass response in the Bi bulk stripping region. The zero anodic current occurs at -0.480 V (vs. Hg/Hg_2SO_4), which is the same as the end of the Bi bulk stripping potential, -0.480 V (vs. Hg/Hg_2SO_4). The current becomes negative between -0.480 V to -0.250 V (vs. Hg/Hg_2SO_4) during the anodic scan although the mass does not change. This may indicate some reduction event occurs without mass increases on the Bi UPD ML surface in that anodic potential region. Another zero anodic current occurs at more positive potential, -0.250 V (vs. Hg/Hg_2SO_4). The local maximum anodic current for Bi UPD stripping occurs at -0.190 V (vs. Hg/Hg_2SO_4). This potential is the reflection point of the curvature from the mass responds in Bi UPD stripping region. Then the current decreases to zero as the applied potential approaches to 0.200 V (vs. Hg/Hg_2SO_4).

Since the separation of peak potential for both Bi bulk and Bi UPD are greater than 0.020 V (= 0.059 V/3), both Bi bulk and Bi UPD are quasi-reversible electron

transfer reaction when scan rate is greater than or equal to 5 mV/s. Table 3-4 summarizes the result.

Table 3-4: Summary of the Bi UPD on Ru [-0.65, 0.20](V vs. Hg/Hg_2SO_4) (5 mV/s).

	Ep (anodic)	**Ep (cathodic)**	**∆Ep (anodic-cathodic)**
Bi Bulk	-0.500 V	-0.562 V	0.062 V
Bi UPD	-0.190 V	-0.340 V	0.150 V

The difference in free energy (∆G) between Bi bulk deposition and Bi UPD on Ru can be calculated from the difference in the corresponding Bi peak potentials. With scan rate of 5 mV/s, the Bi bulk stripping peak is at -0.500 V and the Bi UPD stripping peak is at -0.190 V (Table 3-4). Using $\Delta G = -nF \cdot \Delta E_P$ and $\Delta E_P = E_{Anodic\ Bulk} - E_{Anodic\ UPD}$, the free energy difference between Bi bulk and Bi UPD is found to be 89.75 kJ/mol. This means the Bi UPD adatoms require 89.75 kJ/mol more energy than the Bi bulk does to strip away from Ru surface. Comparing the $\Delta G_{Bi\ UPD\ on\ Ru}$ (89.75 kJ/mol) to the $\Delta G_{Cu\ UPD\ on\ Ru}$ (21.23 kJ/mol) shows that the binding interaction between Bi and Ru is much stronger than the binding interaction between Cu and Ru by 4.23 fold.

Figure 3-13 compares the Bi ML coverage on Ru with scan rate of 5 mV/s and 50 mV/s. With slow scan rate (5 mV/s), the Bi bulk deposition gives 13 Bi ML (by mass) more than the Bi ML with faster scan rate (50 mV/s). Since the scan rate is voltage per second, the x-axis for potential can be thought as an x-axis for time by dividing the potential by the scan rate. The integration of current with slow scan rate gives higher

current in Bi bulk region than with faster scan rate. This explains the higher Bi bulk ML coverage with slow scan rate.

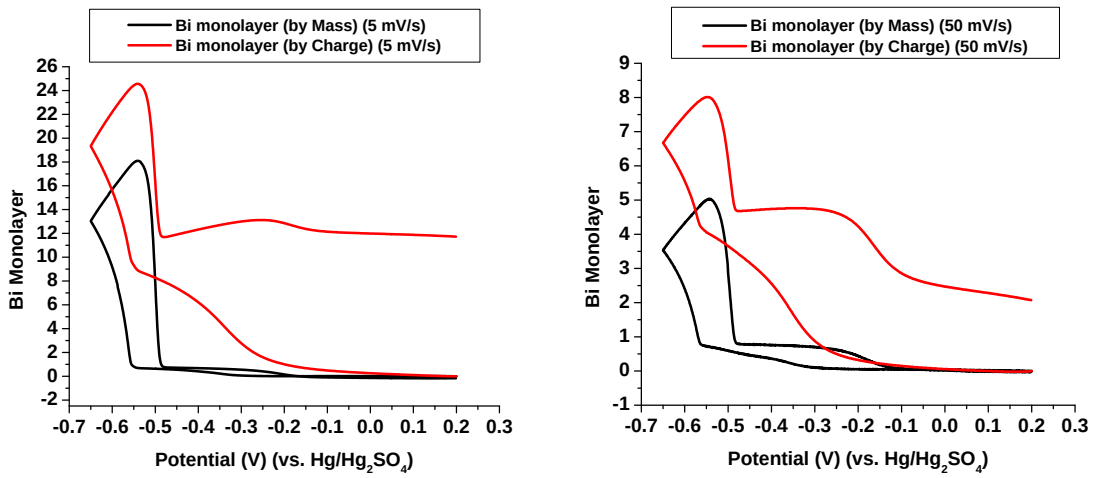

Figure 3-13: Bi monolayer coverage of Bi UPD on Ru with scan range [-0.65, 0.2 V](vs. Hg/Hg_2SO_4). (a.) Scan rate of 5 mV/s. (b.) Scan rate of 50 mV/s.

However, the Bi UPD ML (by mass) for slow scan rate and fast scan rate gives approximately similar Bi ML coverage, with 0.76 Bi ML for 5 mV/s and 0.83 Bi ML for 50 mV/s. Since Bi UPD ML is usually approximately a single monolayer or submonolayer on a substrate, slow scan rate (5 mV/s) and faster scan rate (50 mV/s) will give approximately the same Bi monolayer coverage.

With anodic charge correction, the Bi ML (by charge) for scan rate of 5 mV/s gives -0.0087 Bi UPD ML and 12.86 Bi bulk ML. With anodic charge correction, the Bi ML (by charge) for scan rate of 50 mV/s gives 2.64 Bi UPD ML and 5.95 Bi bulk ML. The negative Bi UPD ML coverage (by charge) for 5 mV/s may be explain by the large

background charge associated with the slow scan rate (5 mV/s) compared with faster scan rate (50 mV/s).

Since the large background current for slow scan rate (5 mV/s) may mask the true Bi UPD ML coverage, two types of background correction are used: anodic charge correction and Ru background charge subtraction. The following analysis of Bi ML by charge are based on anodic charge correction unless otherwise states specifically in the figure description.

3.3.3.3. Scan Rate Effect (Scan Rate ≤ 250 mV/s)

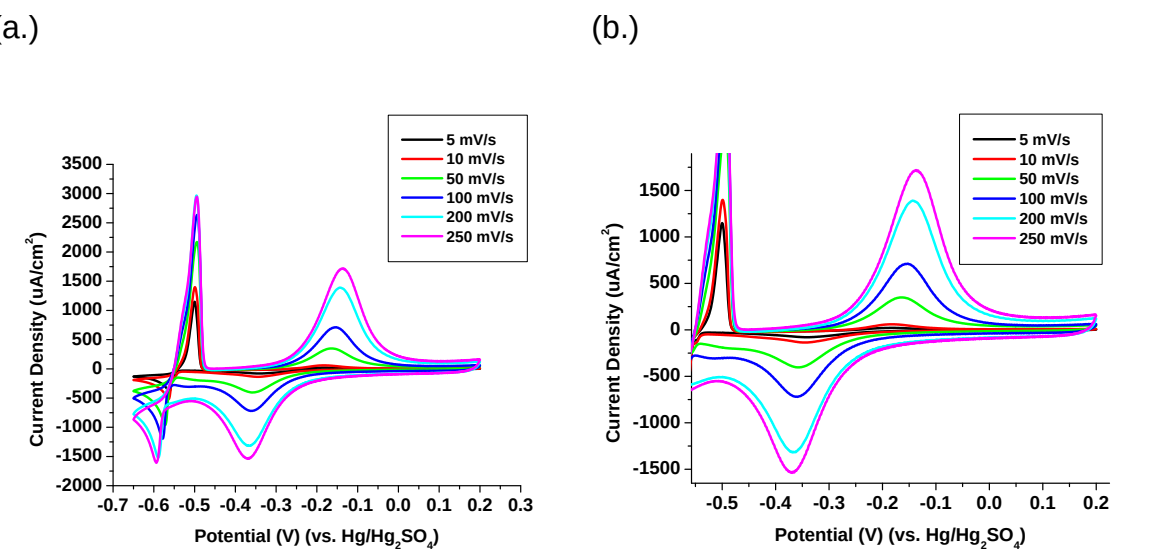

Figure 3-14: Scan rate effect of Bi UPD on Ru with scan range [-0.65, 0.2 V](vs. Hg/Hg_2SO_4). Scan rate range from 5 mV/s to 250 mV/s. (a.) Cyclic Voltammogram of Bi UPD on Ru. (b.) A closer look of CV in the Bi UPD region.

Figure 3-14 shows the scan rate effect of Bi UPD on Ru. As the scan rate increases, the Bi UPD and Bi bulk currents increase.

Figure 3-15 summarizes the scan rate effect of Bi UPD and Bi bulk on the peak potentials and peak current densities. Because the $\Delta E_{Bulk\ Peak}$ and $\Delta E_{UPD\ Peak}$ are larger than 0.020 V (or 0.059 V/3) and |Ipa/Ipc| ≠ 1, both redox processes of Bi UPD and Bi bulk are quasi-reversible electron transfer reaction when the scan rate is 5 mV/s or above.

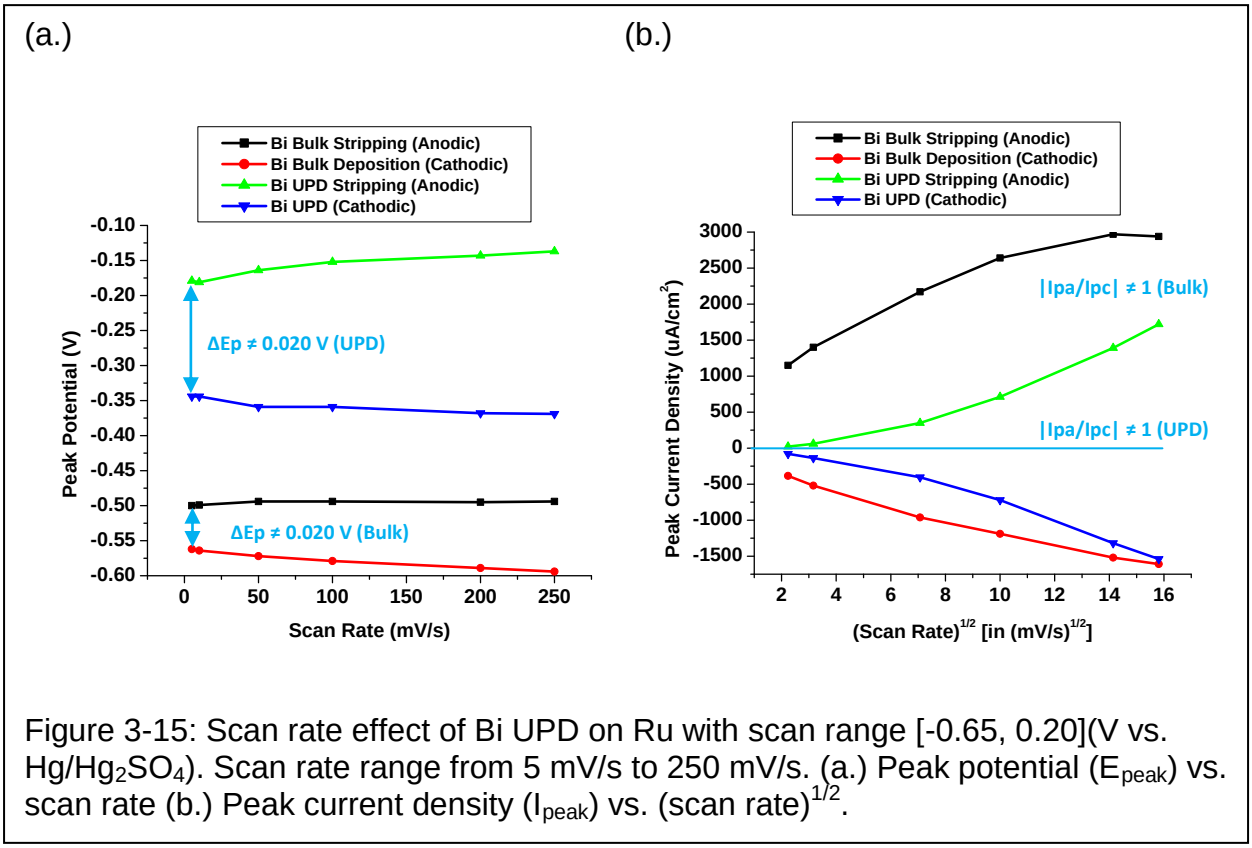

Figure 3-15: Scan rate effect of Bi UPD on Ru with scan range [-0.65, 0.20](V vs. Hg/Hg_2SO_4). Scan rate range from 5 mV/s to 250 mV/s. (a.) Peak potential (E_{peak}) vs. scan rate (b.) Peak current density (I_{peak}) vs. $(scan\ rate)^{1/2}$.

The quasi-reversible electron transfer behavior of Bi UPD can be reasoned by decreasing in the mass transfer of Bi^{3+} ion to the Ru electrode surface. As the potential becomes more negative in the cathodic scan, the Bi^{3+} ions first diffuse and adsorb onto the surface of the Ru electrode. This increases the concentration of local Bi^{3+} ion near the Ru surface, thereby forming a double layer consisting of a layer of Bi^{3+} ions and

surface layer of Ru electrode. This layer of Bi^{3+} ions in the double layer region hinders the diffusion of Bi^{3+} ions from the bulk solution region to the Ru electrode surface. This decreases in mass transfer of the Bi^{3+} ions from bulk region to the double layer region decreases to a point that the rate of replacing Bi^{3+} ions near the Ru surface is much slower than the electron transfer rate from Ru surface to the Bi^{3+} ion. Since the concentration of Bi^{3+} ions is not constant near the Ru electrode surface, the Nernst equation for a reversible electron transfer reaction cannot maintain. This explains the quasi-reversible electron transfer behavior for the Bi underpotential deposition.

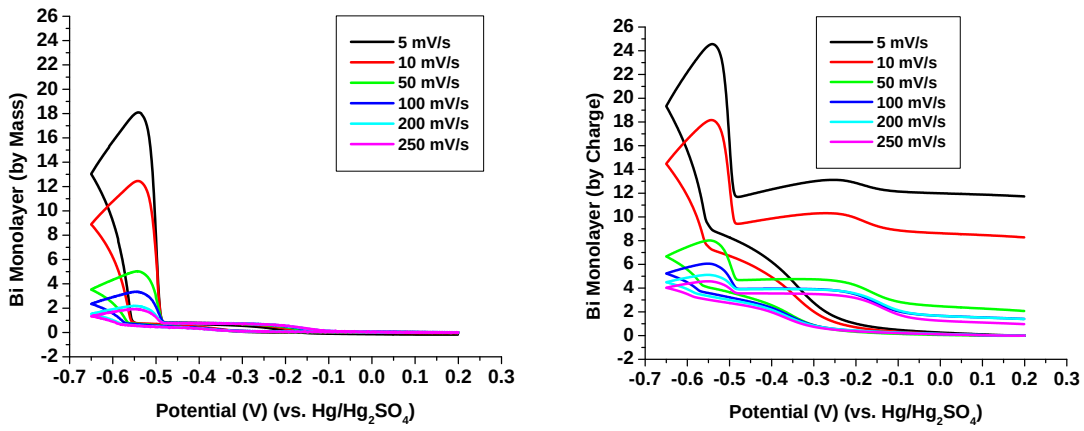

Figure 3-16: Scan rate effect of Bi UPD on Ru with scan range [-0.65, 0.20](V vs. Hg/Hg_2SO_4). Scan rate range from 5 mV/s to 250 mV/s. (a.) Gravitogram of Bi monolayer coverage calculated from mass. (b.) Gravitogram of Bi monolayer coverage calculated from charge. Bi ML by charge in this figures are presented based on cathodic charge correction.

Figure 3-16 to Figure 3-19 show the scan rate effect of Bi ML coverage on Ru. Figure 3-16 gives a parallel comparison of the Bi ML coverage calculated by mass (M)

in Figure 3-16 (a.) and by charge (Q) in Figure 3-16 (b.) with scan rates of 5, 10, 50, 100, 200, and 250 mV/s. The scales of both axes are set to the same range for parallel comparison.

(a.) (b.)

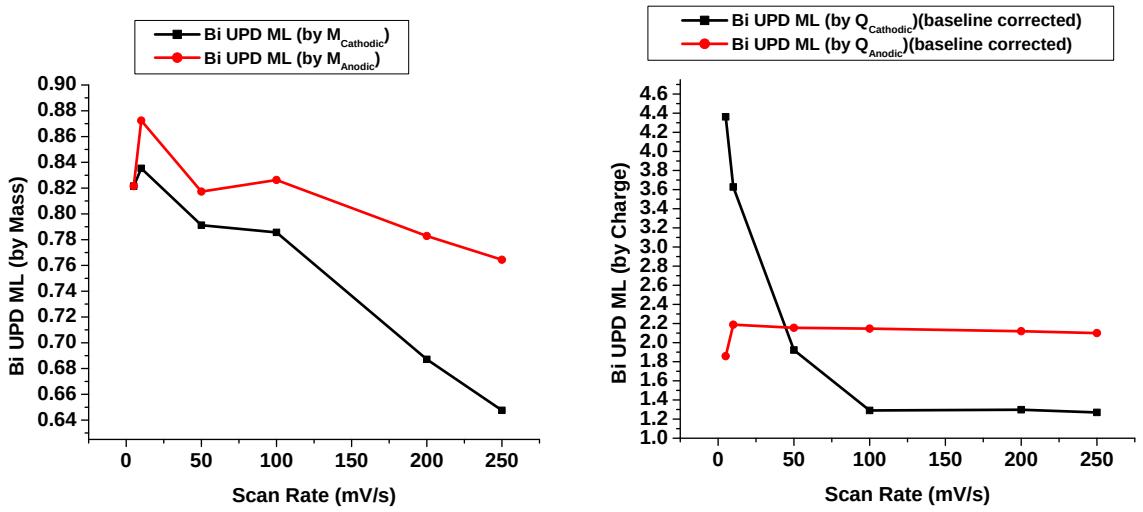

Figure 3-17: Scan rate effect of Bi UPD monolayer on Ru with scan range [-0.65, 0.20](V vs. Hg/Hg_2SO_4). Scan rate range from 5 mV/s to 250 mV/s. (a.) Bi UPD ML coverage calculated from mass (M). (b.) Bi UPD ML coverage calculated from charge (Q).

Figure 3-17 (a.) compares the Bi UPD ML coverage from anodic mass (M_{Anodic}) and from cathodic mass ($M_{Cathodic}$) in Figure 3-16 (a.) with different scan rates. Similarly, Figure 3-17 (b.) compares the Bi UPD ML coverage by anodic charge (Q_{Anodic}) and by cathodic charge ($Q_{Cathodic}$) in Figure 3-16 (b.) with different scan rates.

The general trends of Bi UPD ML by anodic mass (M_{Anodic}) and by cathodic mass ($M_{Cathodic}$) with scan rates in Figure 3-17 (a.) are similar. The maximum Bi UPD ML coverage occurs at the scan rate of 10 mV/s, and then generally decreases as the scan

rate increases to 250 mV/s. Notice that the Bi UPD ML (by M_{Anodic}) gives higher ML coverage than with Bi UPD ML (by $M_{Cathodic}$).

The general trends of Bi UPD ML by anodic charge (Q_{Anodic}) and by cathodic charge ($Q_{Cathodic}$) with scan rates are shown in Figure 3-17 (b.). Bi UPD ML calculated by Q_{Anodic} and $Q_{Cathodic}$ are different greatly at slow scan rate (by 2.6 Bi ML in 5 mV/s and by 1.4 Bi ML in 10 mV/s) and then the difference becomes stable at the higher scan rate (by 1 Bi ML when scan rate is 100 mV/s or more). It is interesting to note that the Bi UPD ML by charge give similar ML coverage when the scan rate is at 50 mV/s. In addition, when the scan rate is 100 mV/s or above, the Bi UPD $ML_{Chathodic\ Charge}$ gives approximately one Bi ML coverage.

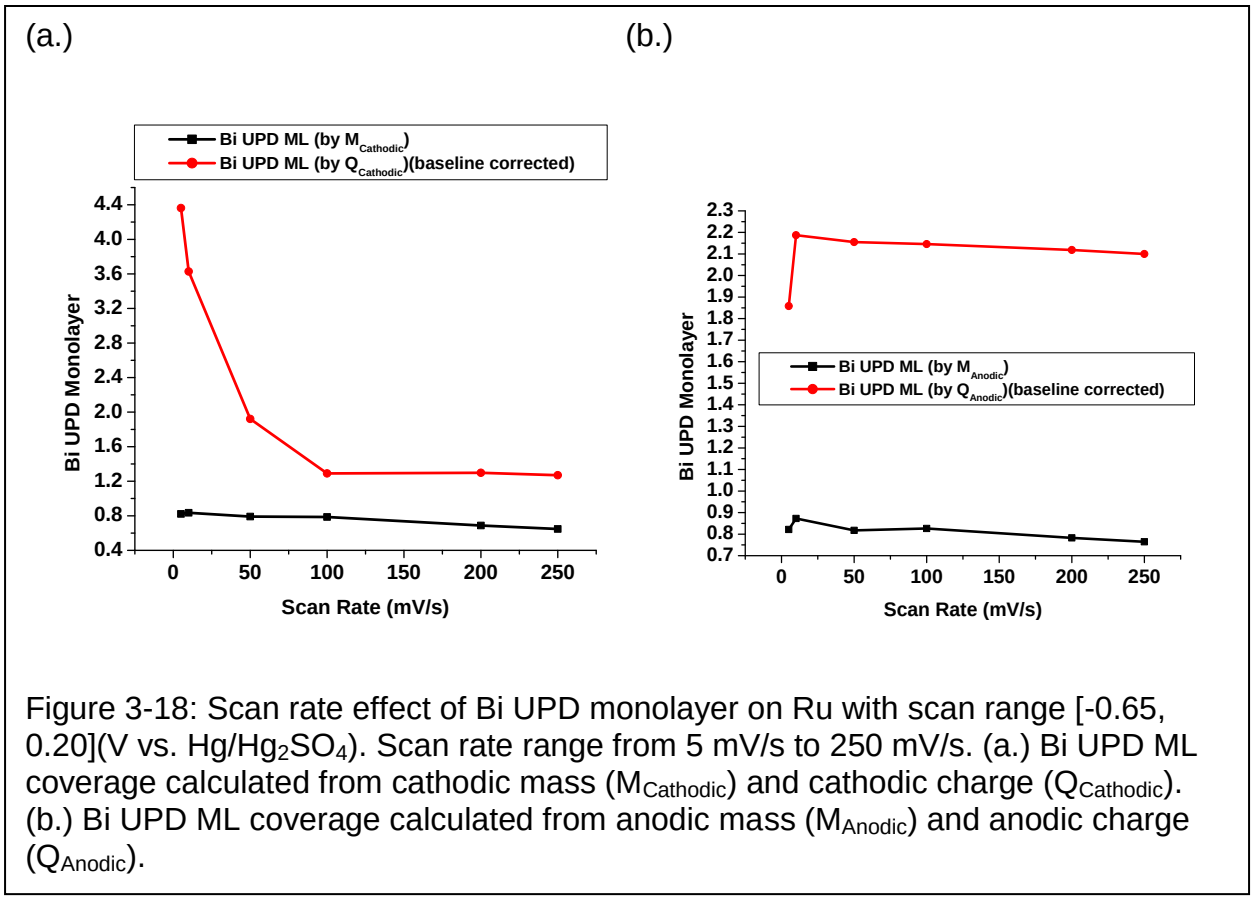

Figure 3-18: Scan rate effect of Bi UPD monolayer on Ru with scan range [-0.65, 0.20](V vs. Hg/Hg_2SO_4). Scan rate range from 5 mV/s to 250 mV/s. (a.) Bi UPD ML coverage calculated from cathodic mass ($M_{Cathodic}$) and cathodic charge ($Q_{Cathodic}$). (b.) Bi UPD ML coverage calculated from anodic mass (M_{Anodic}) and anodic charge (Q_{Anodic}).

Figure 3-18 (a) compares the Bi UPD ML by cathodic mass ($M_{Cathodic}$) in Figure 3-16 (a) and by cathodic charge ($Q_{Cathodic}$) in Figure 3-16 (b) with different scan rates. Similarly, Figure 3-18 (b) compares the Bi UPD ML by anodic mass (M_{Anodic}) in Figure 3-16 (a) and by anodic charge (Q_{Anodic}) in Figure 3-16 (b) with different scan rates.

The Bi UPD ML by $M_{Cathodic}$ is stable at around 0.8 Bi ML at slow scan rate and 0.6 Bi ML (<100 mV/s) at higher scan rate (>200 mV/s); whereas the Bi UPD ML by $Q_{Cathodic}$ is around 4 Bi ML at slow scan rate (<10 mV/s) and around 1.5 Bi ML at higher scan rate (>100 mV/s). The Bi UPD ML by $M_{Cathodic}$ always gives lower ML coverage than Bi UPD ML by $Q_{Cathodic}$.

The trends for Bi UPD ML by M_{Anodic} and Q_{Anodic} are the similar. The lowest Bi UPD ML coverage is at the slowest scan rate (5 mV/s), and the maximum Bi UPD ML coverage is at 10 mV/s. When the scan rate is larger than 10 mV/s, the Bi UPD ML coverage become stable, around 2.1 Bi ML for Bi UPD ML by Q_{Anodic} and 0.8 Bi ML for Bi UPD ML by M_{Anodic}. Similar to the result of comparing Bi UPD ML by $M_{Cathodic}$ and by $Q_{Cathodic}$, Bi UPD ML by Q_{Anodic} always gives higher ML coverage than by M_{Anodic}. The Bi UPD ML by mass always gives lower ML coverage than Bi UPD ML by charge.

Figure 3-19 (a) compares the Bi bulk ML by anodic mass (M_{Anodic}) in Figure 3-16 (a) and anodic charge (Q_{Anodic}) in Figure 3-16 (b). Figure 3-19 (b.) compares the Bi UPD and Bi bulk ML coverage by mass and by charge.

The trends for Bi bulk ML coverage by $M_{AnodicBulk}$ and by $Q_{Anodic\ Bulk}$ are similar. Bi bulk ML coverage decrease as the scan rate increases. Notice that when the scan rates is 50 mV/s or more, the Bi bulk ML by $M_{Anodic\ Bulk}$ and by $Q_{Anodic\ Bulk}$ only differ by about one Bi ML. In addition, the Bi bulk ML coverage by mass is higher than Bi bulk ML by

charge. This result is opposite to the result from the Bi UPD ML coverage. One possible reason may be error from the manual baseline correction for the Bi bulk stripping peaks, which may not include the complete Bi bulk stripping region.

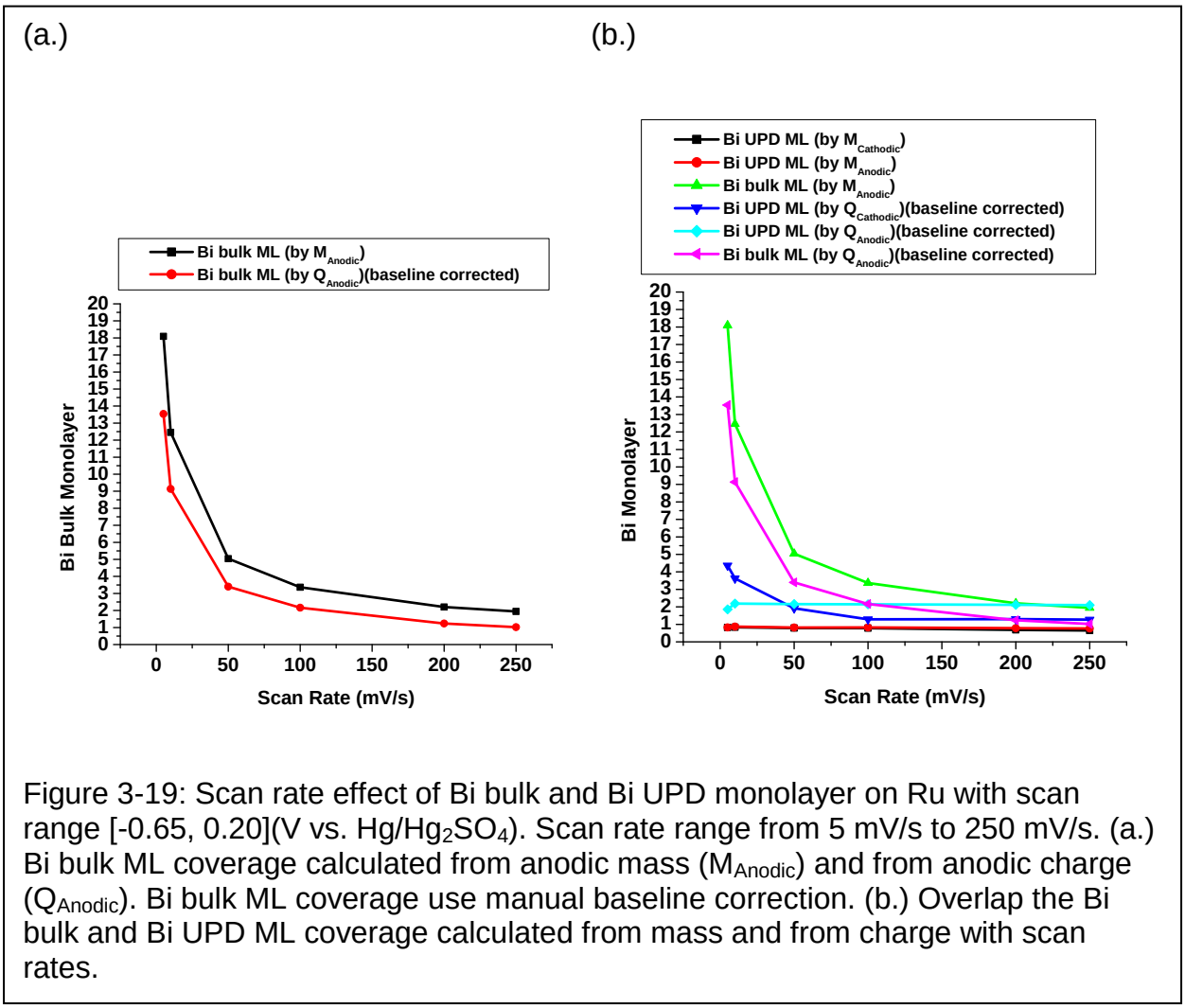

Figure 3-19: Scan rate effect of Bi bulk and Bi UPD monolayer on Ru with scan range [-0.65, 0.20](V vs. Hg/Hg_2SO_4). Scan rate range from 5 mV/s to 250 mV/s. (a.) Bi bulk ML coverage calculated from anodic mass (M_{Anodic}) and from anodic charge (Q_{Anodic}). Bi bulk ML coverage use manual baseline correction. (b.) Overlap the Bi bulk and Bi UPD ML coverage calculated from mass and from charge with scan rates.

3.3.3.4. Scan Rate Effect (Scan Rate > 250 mV/s)

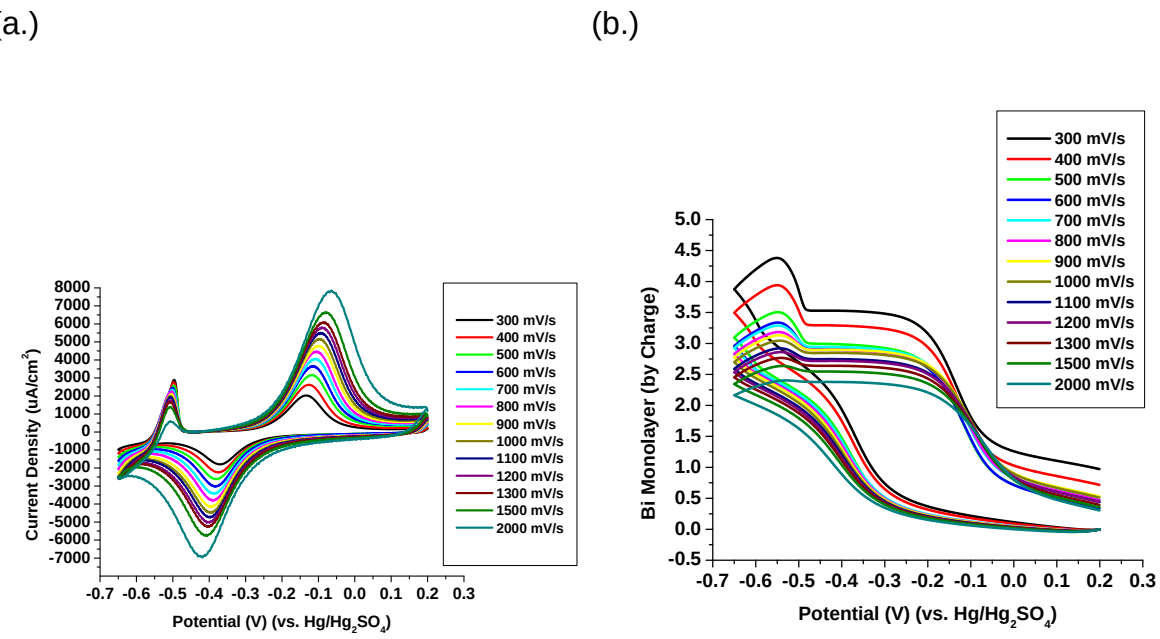

Figure 3-20: Scan rate effect of Bi UPD monolayer on Ru with scan range [-0.65, 0.20](V vs. Hg/Hg_2SO_4). Scan rate range from 300 mV/s to 2000 mV/s. (a.) Cyclic voltammogram of Bi UPD on Ru. (b.) Bi monolayer coverage calculated from charge.

Figure 3-20 to Figure 3-23 shows the scan rate effect on Bi UPD and Bi bulk ML coverage on Ru with scan rate greater than 250 mV/s. Because the EQCM cannot record the frequency change when the scan rate is greater than 250 mV/s, the following Bi UPD and Bi bulk ML coverage are calculated from charge only.

As expected from previous result, the Bi bulk ML coverage decreases when the scan rate increases. Notice that when scan rate is 500 mV/s or more, the peak current density of the Bi bulk stripping peak ($I_{Pa\ Bulk}$) becomes lower than the peak current density of the Bi UPD stripping peak ($I_{Pa\ UPD}$). When the scan rate reaches to 2000 mV/s, the Bi bulk ML coverage is so small that most of the Bi ML coverage is from the Bi UPD

ML. In addition, the peak current density of the Bi bulk deposition peak ($I_{Pc\ Bulk}$) is lower than the peak current density for the Bi UPD deposition peak ($I_{Pc\ UPD}$) when the scan rate is 300 mV/s or more.

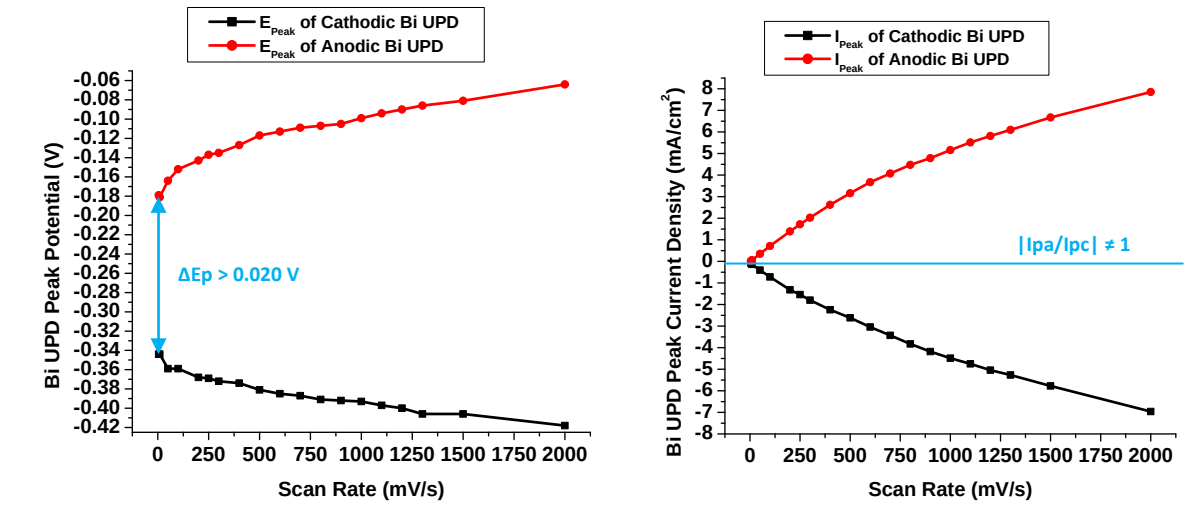

Figure 3-21: Scan rate effect of Bi UPD monolayer on Ru with scan range [-0.65, 0.20](V vs. Hg/Hg_2SO_4). Scan rate range from 5 mV/s to 2000 mV/s. (a.) Peak potentials (E_P) of Bi UPD on Ru vs. scan rate. (b.) Peak current density (I_P) of Bi UPD on Ru vs. scan rate.

Figure 3-21 shows the Bi UPD peak potential and Bi UPD peak current density with different scan rates. Since the separation of peak potential ($\Delta E_{P\ UPD}$) is greater than 0.020 V (avg. $\Delta E_{P\ UPD}$ = 0.261 V), the Bi UPD is a quasi-reversible electron transfer process. Although the average of $|I_{Pa\ UPD}/I_{Pc\ UPD}|$ = 1.04 is closed to one, the ratio of current densities may be masked by the non-faraday charge and give a pseudo-reversible electron transfer process.

(a.) (b.)

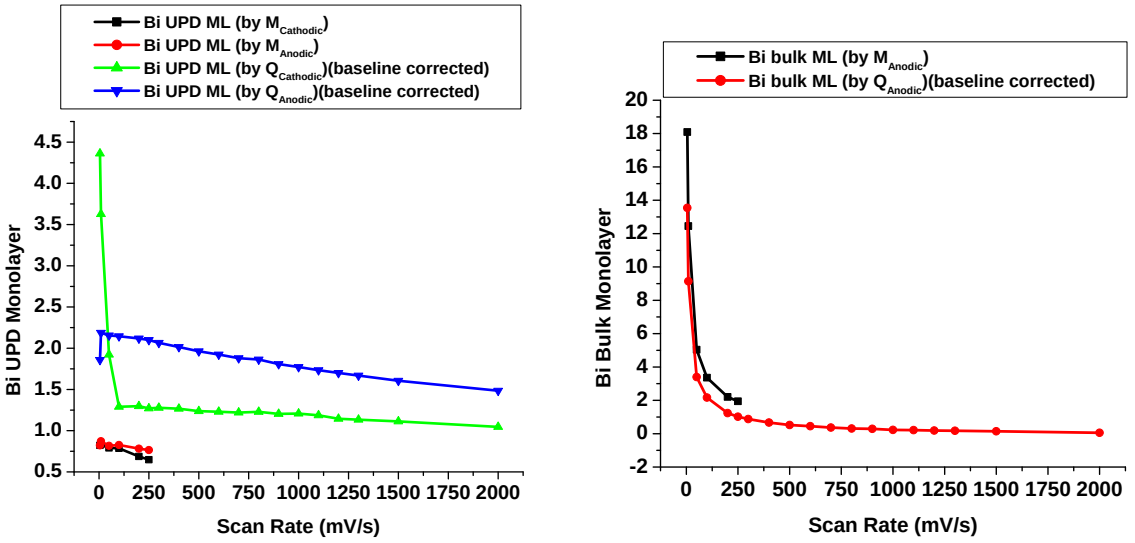

Figure 3-22: Scan rate effect of Bi UPD monolayer on Ru with scan range [-0.65, 0.20](V vs. Hg/Hg_2SO_4). Scan rate range from 5 mV/s to 2000 mV/s. (a.) Bi UPD ML coverage calculated from mass (M) and from charge (Q) (with manual background correction) vs. scan rate. (b.) Bi bulk ML coverage calculated from mass (M) and from charge (Q) (with manual background correction) vs. scan rate. Both Bi UPD and Bi bulk ML use manual baseline correction.

Figure 3-22 shows the Bi UPD and Bi bulk ML coverage with scan rate up to 2000 mV/s. Figure 3-22 (a.) compares the Bi UPD ML coverage calculated by mass and by charge. Generally, Bi UPD ML calculated by charge gives higher ML coverage than Bi UPD ML calculated by mass. Figure 3-22 (b.) compares the Bi bulk ML coverage calculated by mass and by charge. Bi bulk ML by $M_{Anodic\ Bulk}$ and $Q_{Anodic\ Bulk}$ decrease as the scan rate increases. Note that the Bi bulk ML by $Q_{Anodic\ Bulk}$ is closed to one Bi ML when the scan rate is 250 mV/s.

3.3.3.5. Scan Rate Effect (Standard Curve)

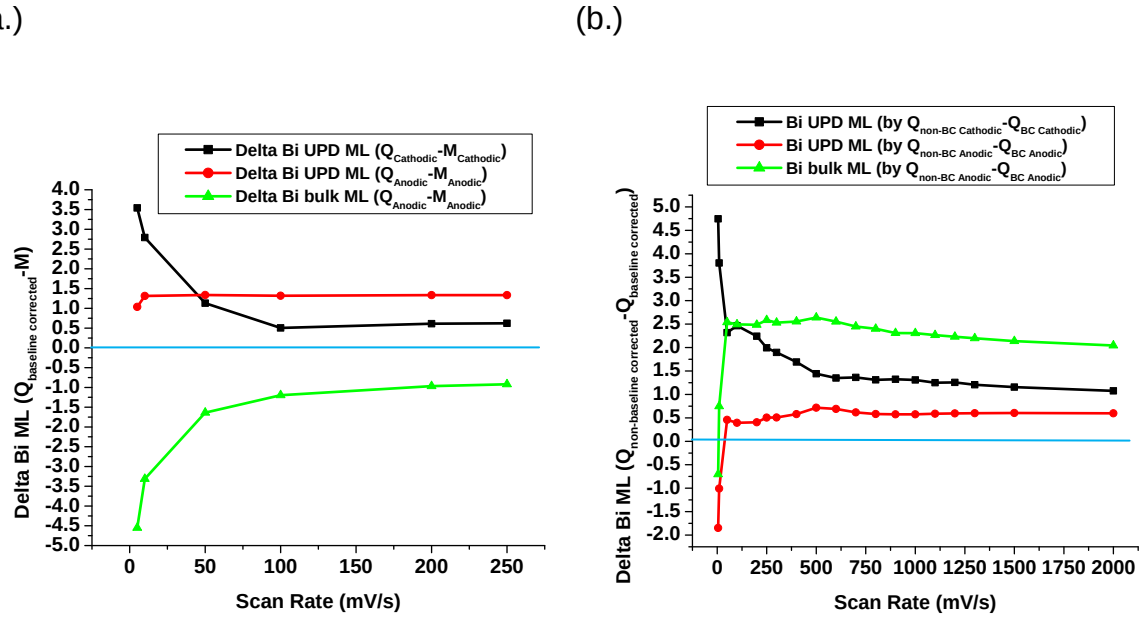

Figure 3-23: Scan rate effect of Bi UPD monolayer on Ru with scan range [-0.65, 0.20](V vs. Hg/Hg_2SO_4). Scan rate range from 5 mV/s to 2000 mV/s. (a.) ΔBi ML ($Q_{baseline\ corrected}$-M) vs. scan rate. (b.) ΔBi ML ($Q_{non\text{-}baseline\ corrected}$-$Q_{baseline\ corrected}$) vs. scan rate. $Q_{non\text{-}baseline\ corrected}$ is calculated by anodic charge correction as a background correction method.

Figure 3-23 (a.) compares the difference in Bi ML coverage calculated by baseline corrected charge ($Q_{baseline\ corrected}$) and by mass (M). This figure can act as a standard correction curve for the Bi ML by $Q_{baseline\ corrected}$ and by mass when the QCM data is not available. The ΔML coverage of Bi UPD calculated from cathodic mass ($M_{Cathodic\ UPD}$) and cathodic charge ($Q_{Cathodic\ UPD}$) gives higher ML coverage difference than the ΔML of Bi UPD calculated from anodic mass ($M_{Anodic\ UPD}$) and anodic charge ($Q_{Anodic\ UPD}$) at slow scan rate (5 and 10 mV/s).

At scan rate of 50 mV/s, the two ΔML coverage of Bi UPD are approximately the same, with the ΔML coverage in anodic Bi UPD ML slightly higher than it in cathodic Bi UPD ML. Notice that the general trend of ΔML for Bi UPD and Bi bulk ML calculated from M_{Anodic} and Q_{Anodic} are similar. Both of these standard curves are concave down. When the scan rate is 100 mV/s or more, the ΔML becomes stable for all of them ($\Delta ML_{UPD\ Cathodic}$ = 0.6 Bi ML, $\Delta ML_{UPD\ Anodic}$ = 1.3 Bi ML, and $\Delta ML_{Bulk\ Anodic}$ =1.0 Bi ML).

Notice that the differences between Bi UPD by anodic charge and by anodic mass ($\Delta ML_{Anodic\ UPD}$) is the most stable curve with approximate 1.3 ΔML of Bi UPD within the scan rate of 5 mV/s and 250 mV/s. Therefore, the Bi UPD ML coverage calculated from anodic mass ($M_{Anodic\ UPD}$) or anodic charge ($Q_{Anodic\ UPD}$) will give more consistent Bi UPD ML coverage than from cathodic mass ($M_{Cathodic\ UPD}$) or cathodic charge ($Q_{Cathodic\ UPD}$).

Figure 3-23 (b.) compares the difference in Bi ML coverage calculated by baseline corrected charge ($Q_{baseline\ corrected}$) and by non-baseline corrected charge ($Q_{non-baseline\ corrected}$). This figure can act as a standard baseline correction curve to give a rough estimate for Bi UPD and Bi bulk ML coverage when baseline corrected charge is not available.

The general trends for ΔML calculated from anodic charge ($Q_{Anodic\ UPD}$ and $Q_{Anodic\ Bulk}$) are similar. Both of these standard curves are concave down. When the scan rate is 50 mV/s or more, the $\Delta ML_{Anodic\ UPD}$ and $\Delta ML_{Anodic\ Bulk}$ become stable ($\Delta ML_{Anodic\ UPD}$ = 0.5 to 0.6 Bi ML and $\Delta ML_{Anodic\ Bulk}$ = 2.0 to 2.5 Bi ML). The $\Delta ML_{Cathodic\ UPD}$ becomes stable with a scan rate of 500 mV/s or more ($\Delta ML_{Cathodic\ UPD}$ = 1.1 to 1.4 Bi ML). Since the $\Delta ML_{Anodic\ UPD}$ is the lowest and the most stable standard curve, Bi ML of Q_{UPD} should

calculate from anodic charge to give consistent Bi UPD ML coverage with different scan rate for parallel comparison.

3.3.3.6. Stability of Bi UPD Adatoms

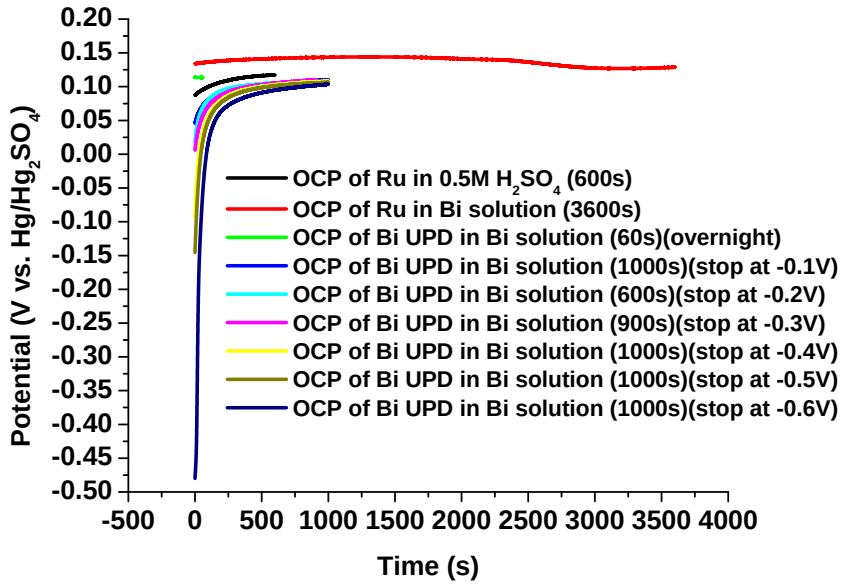

Figure 3-24: Stability of Bi UPD adatoms on Ru in Bi^{3+} solution (1mM Bi^{3+} + 0.5M H_2SO_4 solution) after stopped at different potentials during CV scan. Stability of different Bi ML coverage is measured by open circuit potential (OCP) with time in Bi solution.

Figure 3-24 and Figure 3-25 show the stability of Bi UPD adatoms in Bi solution with different Bi UPD submonolayer coverage. Various Bi ML coverage are obtained by first CV scan several cycles to obtain a reproducible cyclic voltammogram, and then stop at different potentials during the cathodic scan. Figure 3-24 measures the open circuit potential (OCP) with time immediately after CV stopped at various cathodic

potentials. Similarly, Figure 3-25 measures the frequency change with time immediately after CV stopped at various cathodic potentials.

Figure 3-24 shows that the OCP of electrochemically cleaned Ru surface has 0.12 V (vs. Hg/Hg_2SO_4) in 0.5M H_2SO_4 solution, and 0.14 V (vs. Hg/Hg_2SO_4) in Bi^{3+} solution [1mM Bi^{3+} + 0.5M H_2SO_4 solution] without any CV treatment. After CV cleaned in Bi^{3+} solution and placed in Bi^{3+} solution overnight, the OCP becomes 0.11 V (vs. Hg/Hg_2SO_4). The OCPs of Bi adatoms-modified Ru surface all converge to 0.10 to 0.11 V (vs. Hg/Hg_2SO_4) after 1000s. Notice that the Bi ML coverage after stopped at -0.6 V (vs. Hg/Hg_2SO_4) is in the region of Bi bulk deposition. This OCP also increases to 0.10 V after 1000s. This indicates that the surface of Bi bulk and Bi UPD adatoms are oxidized to similar electrochemical properties, which gives the similar OCP values. This may indicate that the Bi ML adatoms are oxidized and dissolve gradually in the Bi^{3+} solution, and the electrode surface is gradually reaches to a thermodynamically stable state.

Notice that the OCP of Ru in Bi solution without any CV treatment in Bi^{3+} solution has more positive OCP value (0.14 V vs. Hg/Hg_2SO_4) than the OCPs of Ru surface after CV treatment in Bi^{3+} solution (0.11 V vs. Hg/Hg_2SO_4). This may indicate that the Ru surface does change after CV treatment in Bi^{3+} solution, and this surface change or Bi adatoms modification may not be easily reversible.

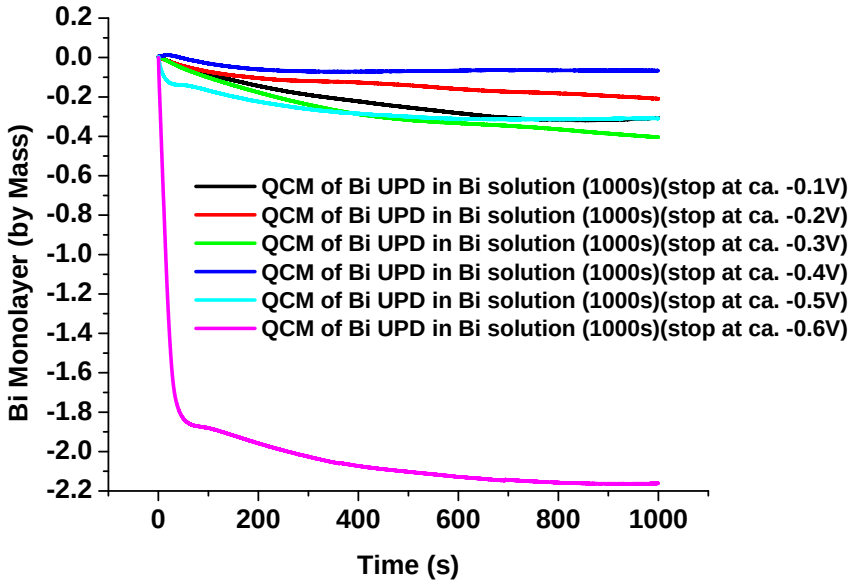

Figure 3-25: Stability of Bi UPD adatoms on Ru in Bi^{3+} solution (1mM Bi^{3+} + 0.5M H_2SO_4 solution) after CV scan stopped at different potentials. Stability of different Bi ML coverage is measured by Bi ML (by mass) loss with time in Bi^{3+} solution.

Figure 3-25 measures the frequency change with time and then converts the frequency change to Bi ML coverage. This figure shows that the surface of Bi bulk and Bi UPD ML coverage decreases overtime. This supports the previous hypothesis that the Bi ML adatoms dissolve gradually in Bi^{3+} solution overtime and reach to a thermodynamically stable state.

Notice that the amount of Bi ML coverage change does not corresponds well with the amount of OPC change in cathodic potential. Since the amount of frequency drifts are difficult to predict, the frequency drifts may cause this happened during the QCM measurement. The stability of Bi ML coverage in Bi^{3+} solution by OCP and by frequency change is summarized in Table 3-5.

Table 3-5: Stability of Bi ML adatoms in Bi^{3+} solution. All potentials are with respected to Hg/Hg_2SO_4.

Condition	Initial OCP (V)	Final OCP (V)	ΔML of Bi
No CV treatment	0.134	0.128	n/a
After CV treatment	0.114	0.114	n/a
Stop at -0.1 V	0.046	0.110	-0.306
Stop at -0.2 V	0.018	0.106	-0.210
Stop at -0.3 V	0.006	0.110	-0.404
Stop at -0.4 V	-0.094	0.108	-0.066
Stop at -0.5 V	-0.146	0.1063	-0.309
Stop at -0.6 V	-0.480	0.104	-2.161
Average	-0.050	0.111	-0.576
Standard Deviation	0.198	0.0076	0.785

3.3.4. Bi UPD on RuOx (V vs. Hg/Hg_2SO_4)

3.3.4.1. Background vs. Bi UPD

Figure 3-26 shows the Bi UPD on Ru echem oxide (electrochemically formed Ru oxide). Since the background current density of Ru oxide (125 uA/cm^2) is large compared to that of Ru (50 uA/cm^2), the Bi UPD current density is masked largely by the background current. Nevertheless, the E_{Peak} of Bi UPD stripping peak is observe at -0.183 V (vs. Hg/Hg_2SO_4), and the E_{Peak} of Bi bulk stripping are observed at -0.487 V (vs. Hg/Hg_2SO_4). The Bi UPD deposition peak is difficult to be distinguished from the cyclic voltammogram. The E_{Peak} of Bi bulk deposition is observed at -0.574 V (vs. Hg/Hg_2SO_4).

(a.) (b.)

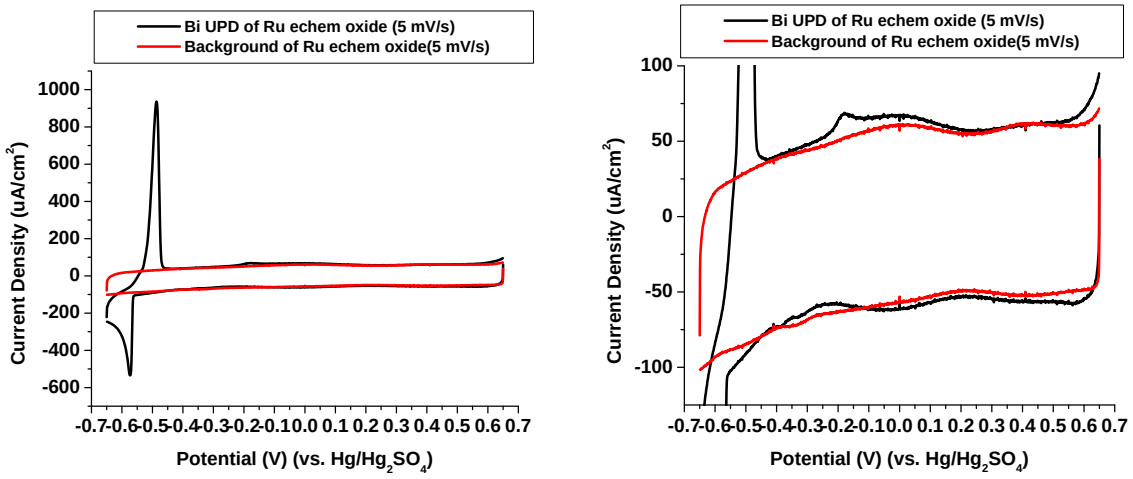

Figure 3-26: (a.) CV of background and Bi deposition on Ru echem oxide with scan range [-0.65, 0.65](V vs. Hg/Hg_2SO_4). Scan rate of 5 mV/s. (b.) A closer look in Bi UPD region.

(a.) (b.)

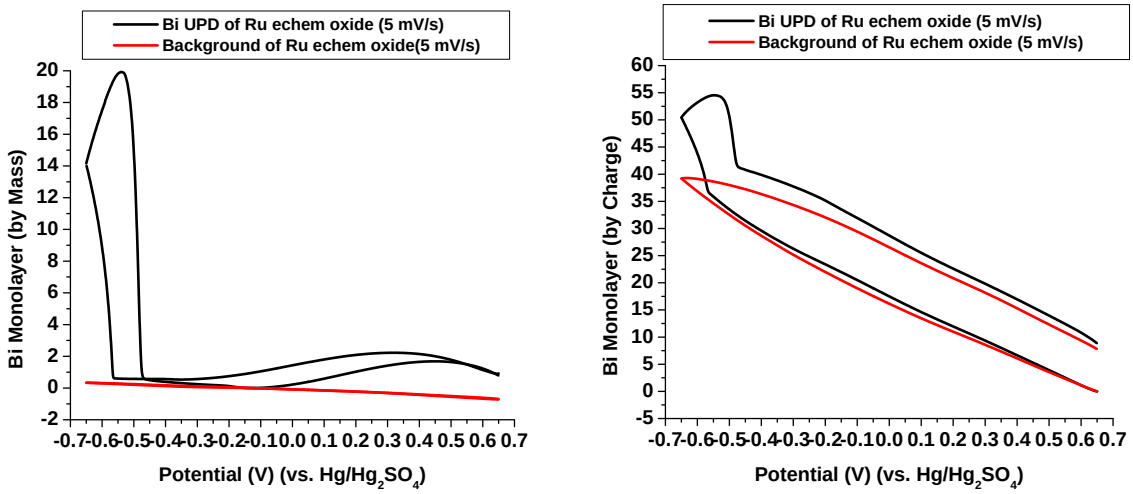

Figure 3-27: Bi monolayer coverage of background and Bi deposition on Ru echem oxide with scan range [-0.65, 0.65](V vs. Hg/Hg_2SO_4). Scan rate of 5 mV/s. (a.) Bi ML (by mass) vs. potential. (b.) Bi ML (by charge) vs. potential.

Figure 3-27 compares the Bi ML coverage on Ru echem oxide. Figure 3-27 (a.) shows the Bi ML coverage calculated from frequency change (Bi ML_{Mass}), and Figure 3-27 (b.) shows the Bi ML coverage calculated from charge (Bi ML_{Charge}). Bi ML_{Mass} shows more distinct Bi UPD and Bi bulk region than Bi ML_{Charge} does. Because the background current for Ru echem oxide is large, the Bi ML_{Charge} is unavoidably masked by the background charge. Due to this high background charge, the following Bi ML coverage on Ru echem oxide is calculated only from the Bi ML_{Mass} unless otherwise stated in the text.

3.3.4.2. Bi UPD on RuOx

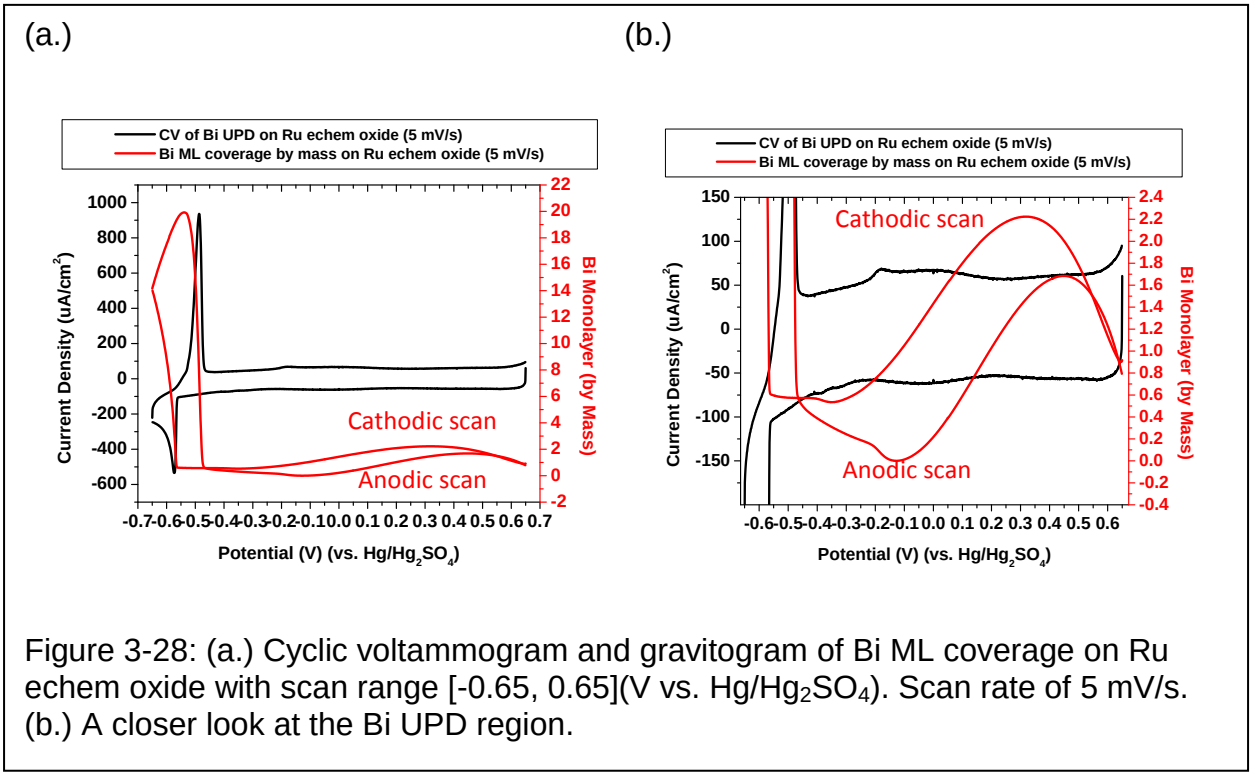

Figure 3-28: (a.) Cyclic voltammogram and gravitogram of Bi ML coverage on Ru echem oxide with scan range [-0.65, 0.65](V vs. Hg/Hg_2SO_4). Scan rate of 5 mV/s. (b.) A closer look at the Bi UPD region.

Figure 3-28 overlaps the CV and Bi ML coverage with potential. Notice that in cathodic scan, mass first increases in [0.32, 0.65](V vs. Hg/Hg_2SO_4), decreases in [-0.35, 0.32](V vs. Hg/Hg_2SO_4), Bi UPD in [-0.56, -0.35](V vs. Hg/Hg_2SO_4), and then Bi bulk deposition in [-0.65, -0.56](V vs. Hg/Hg_2SO_4).

The Bi bulk keeps depositing in the anodic scan until the potential reaches to -0.54 V (vs. Hg/Hg_2SO_4). In the anodic scan, Bi bulk stripping occurs in [-0.54, -0.46](V vs. Hg/Hg_2SO_4), Bi UPD stripping in [-0.46, -0.13](V vs. Hg/Hg_2SO_4), mass increases in [-0.13, 0.45](V vs. Hg/Hg_2SO_4), and then mass decreases in [-0.45, -0.65](V vs. Hg/Hg_2SO_4).

Notice that a small mass respond curve occurs at -0.41 V (vs. Hg/Hg_2SO_4) in cathodic scan, and a small mass respond curve occurs at -0.21 V (vs. Hg/Hg_2SO_4) in anodic scan. The anodic mass curve corresponds well with the initiation of Bi UPD stripping peak. However, the cathodic mass curve does not show a distinct Bi UPD reduction peak. Two possible explanations can account for this observation. First, the mass increases may indicate the neutral charge Bi atoms adsorbed onto the Ru echem oxide surface, hence no current generated during the adsorption of Bi adatoms. Another possible explanation may be that the oxidation and reduction taking place at the same time during Bi underpotential deposition on Ru echem oxide. Soon after the Bi adatoms adsorbed on the Ru oxide surface, the Bi adatoms were oxidized by Ru oxide. Since the reduction potential for the Ru oxide (RuO_4) is more positive than the reduction potential for the BiO^+ or $BiOH^{2+}$, the Ru oxide and Bi adatoms can undergo redox reaction by transferring oxygen from Ru oxide to oxidize Bi adatoms, meanwhile, transferring

electrons from Bi adatoms to reduce the Ru oxide. This redox process can decrease the current response during the Bi UPD region.

The possible mechanism of Bi UPD on Ru oxide (RuO_4) is proposed as following. During cathodic scan, anions (possibly anions of the sulfuric acid) adsorbed onto the Ru oxide surface in [0.32, 0.65](V vs. Hg/Hg_2SO_4), thereby increases the electrode mass. Then the anion expulsion and Ru oxide surface reduction occur in [-0.35, 0.32](V vs. Hg/Hg_2SO_4), decreasing the mass of the Ru oxide electrode. Bi UPD occurs in [-0.56, -0.35](V vs. Hg/Hg_2SO_4), and Bi bulk deposition takes place in [-0.65, -0.56](V vs. Hg/Hg_2SO_4). When the potential reverses, the Bi bulk deposition still takes place until the potential reaches to -0.54 V (vs. Hg/Hg_2SO_4). The Bi bulk stripping occurs in [-0.54, -0.46](V vs. Hg/Hg_2SO_4), and the Bi UPD stripping takes place in [-0.46, -0.13](V vs. Hg/Hg_2SO_4). During the Bi UPD stripping, the first few layers of the Ru oxide surface may just be fresh Ru surface. When the anodic potential scans over -0.13 V (vs. Hg/Hg_2SO_4), the first few layers of fresh Ru were oxidized to Ru oxide; meanwhile, anions (possibly anions of the sulfuric acid) adsorbed onto the Ru oxide surface. This explains the mass increases in [-0.13, 0.45](V vs. Hg/Hg_2SO_4) during anodic scan. Then anion expulsion from Ru oxide surface occurs in [-0.45, -0.65](V vs. Hg/Hg_2SO_4), decreasing the surface mass of Ru oxide.

3.3.4.3. Bi UPD on Ru vs. Bi UPD on RuOx (with Background Subtraction)

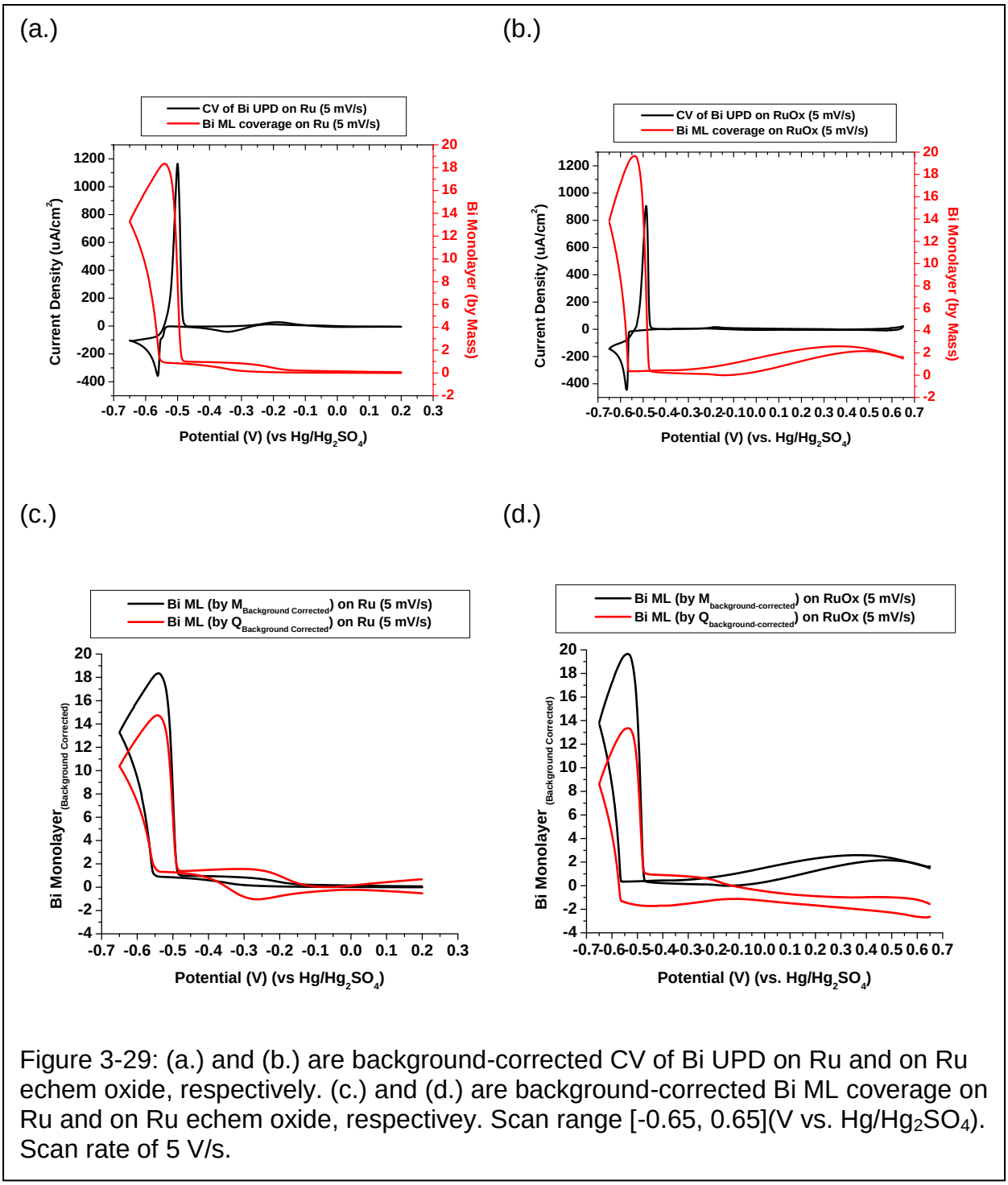

Figure 3-29: (a.) and (b.) are background-corrected CV of Bi UPD on Ru and on Ru echem oxide, respectively. (c.) and (d.) are background-corrected Bi ML coverage on Ru and on Ru echem oxide, respectivey. Scan range [-0.65, 0.65](V vs. Hg/Hg_2SO_4). Scan rate of 5 V/s.

Figure 3-29 compares the cyclic voltammogram of Bi deposition [Figure 3-29 (a.) and (b.)], Bi ML_{Mass}, and Bi ML_{Charge} [Figure 3-29 (c.) and (d.)] coverage on Ru and on RuOx after subtracting from background CV, equivalent Bi ML_{Mass}, and equivalent Bi ML_{Charge}, respectively. The axis scale for both cyclic voltammogram and Bi ML coverage of Ru and of RuOx are set to the same for parallel comparison. In addition, the same scan rate of 5 mV/s are used for both Ru and RuOx.

After subtracting from background current, the redox peaks of Bi UPD and Bi bulk are clearly showed in CV of Ru. Notice there are three Bi reduction peaks (at -0.344 V, -0.546 V, and -0.562 V vs Hg/Hg_2SO_4) and two Bi oxidation peaks (at -0.186 V and -0.500 V vs. Hg/Hg_2SO_4) are observed in Figure 3-29 (a.). This background-corrected CV of Bi deposition shows an irreversible electron transfer process on the Ru surface.

The following Bi species are proposed for each reduction and oxidation peaks in the Bi UPD region. The reduction peak at -0.344 V and the oxidation peak at -0.186 V may represent the redox couple of BiO^+ ion and Bi atom. The reduction peak at -0.546 V may represent the reduction of Bi^{3+} ion to Bi^+ ion, which is an irreversible electron transfer process. The reduction peak at -0.562 V may represent the reduction of Bi^+ ion to Bi atom.

In Figure 3-29 (c.), notices that the Bi $ML_{Charge\ Bulk}$ (14.75 Bi ML) has lower Bi ML coverage than the Bi $ML_{Mass\ Bulk}$ (18.28 Bi ML). This lower Bi ML_{Charge} coverage may due to the over-subtraction from the Ru background current in the Bi bulk stripping region. However, the Bi $ML_{Charge\ UPD}$ (1.47 Bi ML) is slightly higher than the Bi $ML_{Mass\ UPD}$ (1.00

Bi ML). This may indicate some electron transfer process without mass change in the Bi UPD region.

Figure 3-29 (a.) and (b.) compare the cyclic voltammogram of Bi deposition on Ru and on RuOx, respectively. Notice that the oxidation peak current for Bi bulk peak of Ru (1165 μA/cm^2) is higher than that of RuOx (900 μA/cm^2) by 265 μA/cm^2, which represents 0.82 Bi ML_{Charge} coverage. However, the Bi $ML_{Mass\ Bulk}$ coverage on Ru (15.28 Bi ML) is smaller than that on RuOx (19.67 Bi ML) by 4.39 Bi ML_{Mass}. This discrepancy in Bi $ML_{Mass\ Bulk}$ may indicate that the lowest point of Bi ML_{Mass} in RuOx may not be the fresh RuOx surface. Bi ML adatoms are not stripped away completely. Another explanation would be that the reduction of RuOx and Bi UPD happened at the same time that the mass decreases for the reduction of RuOx masks the mass increases for the reduction of Bi ions, making the lowest point of Bi ML_{Mass} in RuOx different from the true zero Bi ML_{Mass} coverage.

Figure 3-29 (c.) and (d.) compare the Bi ML coverage on Ru and on RuOx. The Bi $ML_{Charge\ Bulk}$ is slightly higher for Ru (14.20 Bi ML) than for RuOx (13.34 Bi ML) by 0.86 Bi ML, which is closed to the Bi ML coverage for 265 μA/cm^2 (or 0.82 Bi ML_{Charge}) from Bi bulk stripping peak current.

3.3.4.4. Progressive Scan

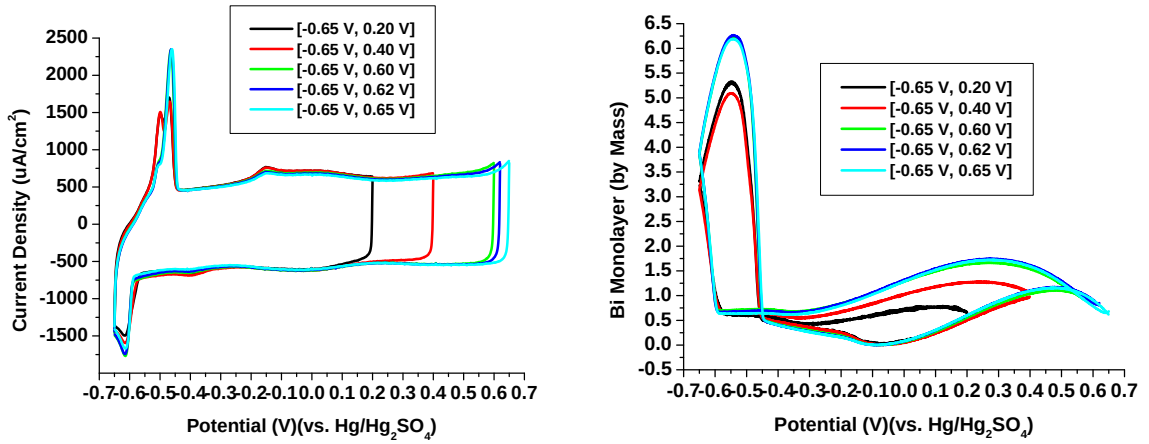

Figure 3-30: Progressive scan of Bi ML coverage on Ru echem oxide with scan range [-0.65, x](V vs. Hg/Hg_2SO_4). Scan rate of 50 mV/s. (a.) Current density vs. potential. (b.) Bi ML coverage (by mass) vs. potential.

Figure 3-30 shows the progressive anodic scan of Bi UPD on Ru echem oxide. The scanning sequence is the same sequence as the limit of anodic potential increases. Notice that two anodic peaks in the Bi bulk stripping region are observed at -0.500 V and -0.468 V (vs Hg/Hg_2SO_4) when scan within [-0.65, 0.20] and [-0.65, 0.40](V vs Hg/Hg_2SO_4), but not in other scanning ranges.

Though the CV was not shown, the peak current for the -0.500 V (vs Hg/Hg_2SO_4) anodic peak increases in the first several CV cycles then decreases as the number of CV cycle increases. In contrast, the peak current for the -0.468 V (vs Hg/Hg_2SO_4) anodic peak decrease as the -0.500 V (vs Hg/Hg_2SO_4) peak increases then increases as the -0.500 V (vs Hg/Hg_2SO_4) peak decreases. After several CV cycles, the peak on -

0.500 V (vs Hg/Hg_2SO_4) is disappeared and was not observed in the later experiments. These two anodic peaks may indicate that the Ru oxides are undergone a surface morphology change, and this surface change is not reversible, both chemically and thermodynamically. Notice that the peak current for [-0.65, 0.20] at -0.468 V is higher than the peak current for [-0.65, 0.40](V vs Hg/Hg_2SO_4), whereas the peak current for [-0.65, 0.20] at -0.500 V is lower than the peak current for [-0.65, 0.40](V vs Hg/Hg_2SO_4).

Figure 3-30 (b.) shows progressive scan effect of the Bi ML_{Mass} coverage on Ru echem oxide. Notice that as the anodic potential limit increases, the Bi UPD ML_{Mass} coverage does not change. This indicates that the reduction potential for Bi UPD is more negative than 0.20 V (vs. Hg/Hg_2SO_4). In addition, notice that the Bi bulk ML_{Mass} coverage increases as the limit of the anodic potential increases, except for the potential range [-0.65, 0.20] and [-0.65, 0.40](V vs Hg/Hg_2SO_4). The Bi bulk ML_{Mass} in [-0.65, 0.20](V vs. Hg/Hg_2SO_4) is higher than it in [-0.65, 0.40](V vs Hg/Hg_2SO_4) by 0.20 Bi ML coverage. This strongly supports that the Bi bulk stripping peak potential is at -0.468V instead of at -0.500 V (vs Hg/Hg_2SO_4). Although the Bi bulk ML_{Mass} increases as the limit of anodic potential increases, further experiments must be done to eliminate the effect of surface morphology change on Bi bulk deposition.

3.3.4.5. Scan Rate Effect

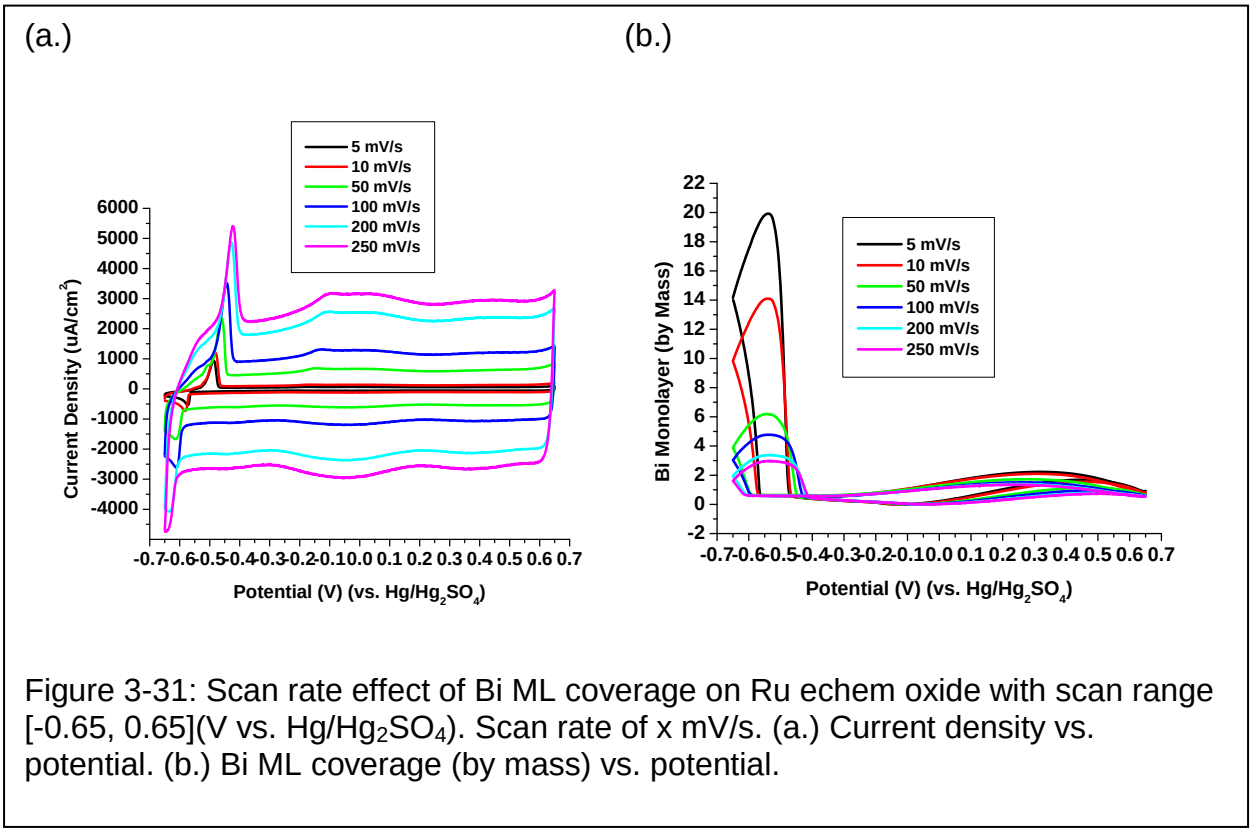

Figure 3-31: Scan rate effect of Bi ML coverage on Ru echem oxide with scan range [-0.65, 0.65](V vs. Hg/Hg_2SO_4). Scan rate of x mV/s. (a.) Current density vs. potential. (b.) Bi ML coverage (by mass) vs. potential.

Figure 3-31 shows the scan rate effect of the Bi ML coverage on Ru echem oxide. As the scan rate increases, the Bi bulk ML_{Mass} coverage decreases. In contrast, the Bi UPD ML_{Mass} coverage stays constant as the scan rate increases. Notice that the peak potential of the Bi bulk deposition peak shifts to more negative potential and the peak potential of the Bi bulk stripping peak shifts to more positive potential as the scan rate increases. This indicates that the Bi bulk redox reaction is a quasi-reversible electron transfer process. The Bi UPD peaks of the Ru echem oxide are difficult to be distinguished from the background current on the cyclic voltammogram.

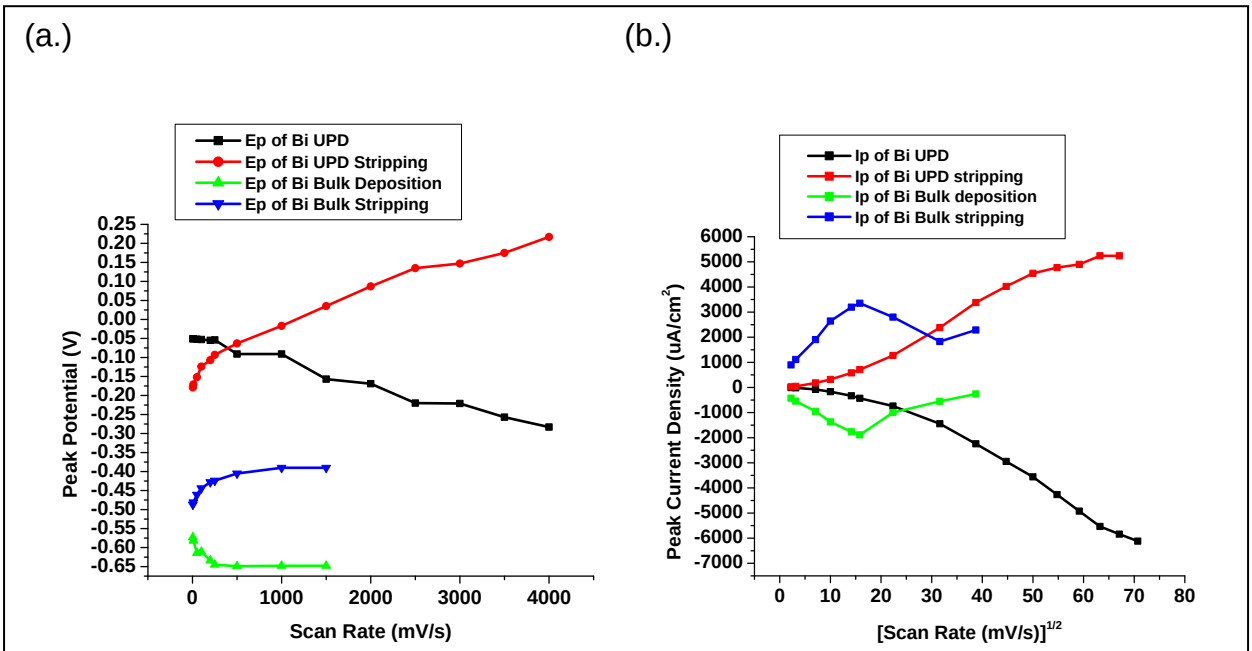

Figure 3-32: Scan rate effect of Bi UPD ML and Bi bulk ML on Ru echem oxide with scan range [-0.65, 0.65](V vs. Hg/Hg_2SO_4). Scan rate range from 5 mV/s to 4000 mV/s. (a.) Peak potentials (E_{Peak}) of Bi ML vs. scan rate. (b.) Peak currents density (I_{Peak}) of Bi ML vs. $(\text{scan rate})^{1/2}$.

Figure 3-32 shows the peak potential (E_P) and peak current (I_P) of the Bi bulk and Bi UPD on Ru echem oxide. Because the $\Delta E_{P\ UPD}$ is larger than 0.020 V and the $E_{P\ UPD}$ and $I_{P\ UPD}$ are not independent of the scan rate, Bi UPD on Ru echem oxide is a quasi-reversible electron transfer process when the scan rate is greater than 5 mV/s. Similarly, since $\Delta E_{P\ Bulk}$ is larger than 0.020 V and the $E_{P\ Bulk}$ and $I_{P\ Bulk}$ are not independent of the scan rate, Bi bulk on Ru echem oxide is a quasi-reversible electron transfer process when the scan rate is greater than 5 mV/s.

(a.) (b.)

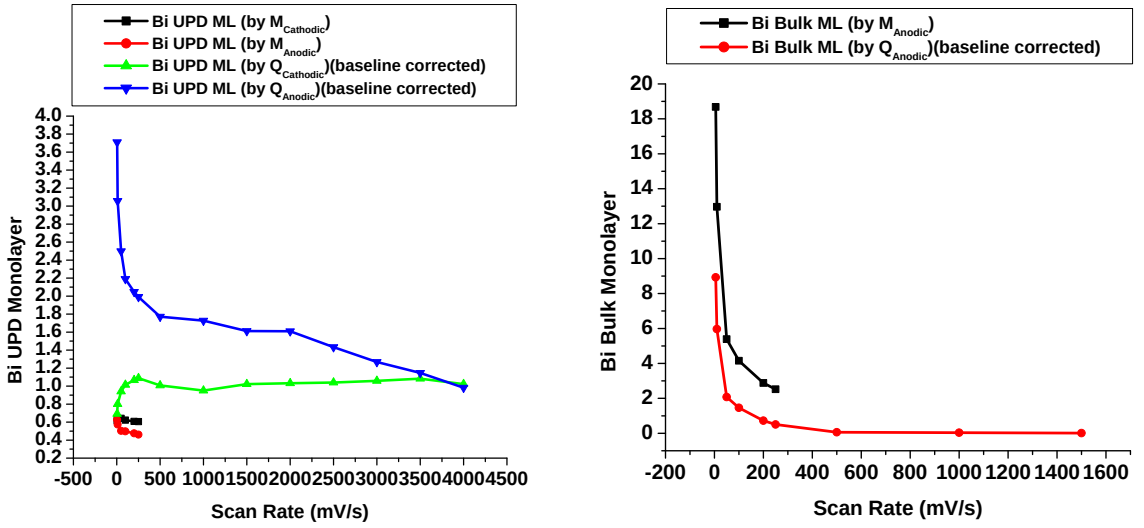

Figure 3-33: Scan rate effect of Bi ML coverage on Ru echem oxide with scan range [-0.65, 0.65](V vs. Hg/Hg_2SO_4). Scan rate of x mV/s. (a.) Bi UPD ML coverage vs. scan rate. (b.) Bi bulk monolayer coverage vs. scan rate.

Figure 3-33 shows the scan rate effect on the Bi ML coverage of the Ru echem oxide. Figure 3-33 (a.) shows the Bi UPD ML_{Charge} has higher ML coverage than the Bi UPD ML_{Mass}. However, Figure 3-33 (b.) shows that the Bi bulk ML_{Charge} has lower ML coverage than the Bi bulk ML_{Mass}. This may caused by the systematic error when performing the manual baseline correction for the charge in the Bi bulk stripping region. Nevertheless, the general trends of the Bi bulk ML coverage are the same, with the higher ML coverage in slow scan rate and lower ML coverage in higher scan rate. When the scan rate is 250 mV/s or higher, the Bi bulk ML coverage becomes stable. When the scan rate is 1500 mV/s or higher, the Bi bulk peak current is difficult to be distinguished from the background current; therefore, Bi bulk ML_{Charge} is calculated until 1500 mV/s. Similarly, when the scan rate faster than 4000 mV/s, the Bi UPD peak current is difficult

to be distinguished from the background current; therefore, the Bi UPD ML_{Charge} is calculated until 4000 mV/s. Notice that the EQCM can detect the frequency change only when the scan rate is 250 mV/s or slower; therefore, no Bi ML_{Mass} was obtained with scan rate higher than 250 mV/s.

3.3.4.6. Scan Rate Effect on Ru vs. on RuOx

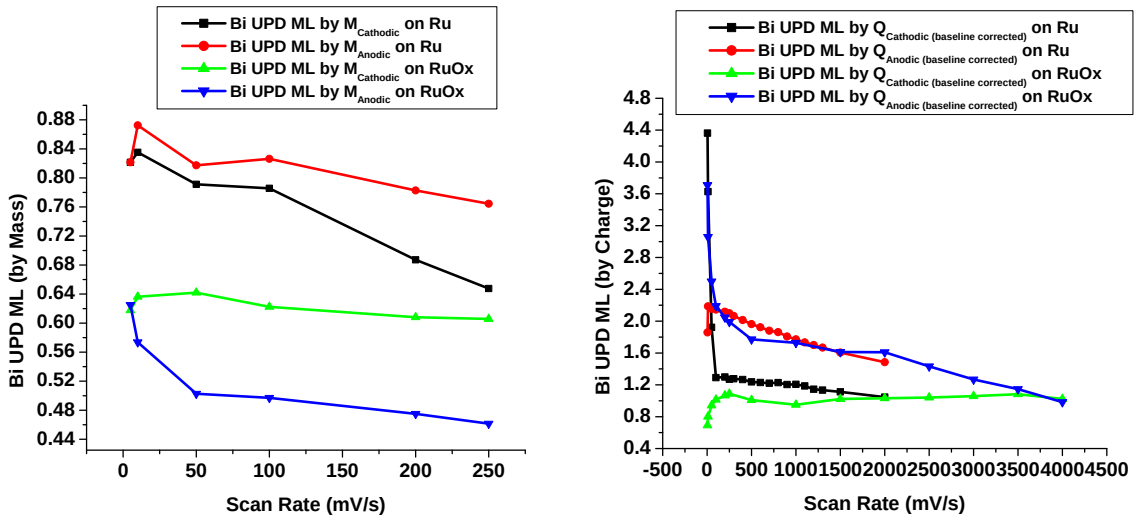

Figure 3-34: Comparison of Bi UPD ML coverage on Ru and Ru echem oxide with scan range [-0.65, 0.65](V vs. Hg/Hg_2SO_4). Scan rate of x mV/s. (a.) Bi UPD ML_{Mass} vs. scan rate. (b.) Bi UPD ML_{Charge} vs. scan rate.

Figure 3-34 compares the Bi UPD ML coverage of Ru with it of Ru echem oxide. Figure 3-34 (a.) compares the Bi UPD ML_{Mass} coverage of Ru and it of Ru echem oxide. The Bi UPD ML_{Mass} of Ru has higher ML coverage than the Bi UPD ML_{Mass} of Ru echem oxide (by 0.20 Bi ML). This shows that the Ru echem oxide has lower Bi UPD ML

plating efficiency than Ru does. This lower plating efficiency may due to high electronegativity of oxygen atoms of the RuO_2 holding the surface electron tighter than the Ru metal surface does. The tighter the surface electrons hold onto the electrode surface, the harder for the electron transfer process to occur from the electrode surface to the metal cations; therefore, decreasing the efficiency of Bi UPD on RuO_2. Notice that both Bi UPD ML_{Mass} coverage and Bi UPD ML_{Charge} coverage decrease as the scan rate increases.

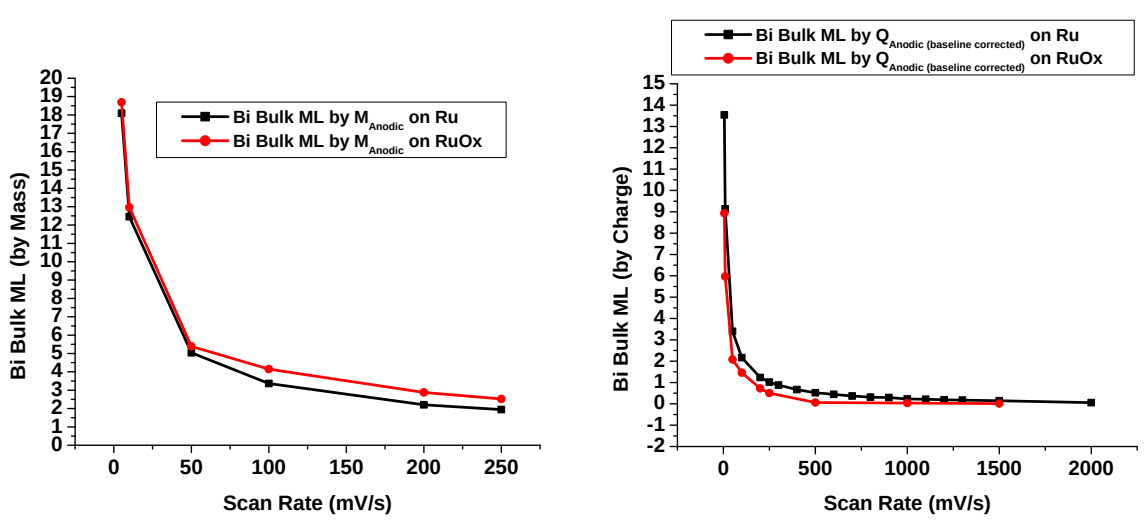

Figure 3-35: Comparison of Bi bulk ML coverage on Ru and Ru echem oxide with scan range [-0.65, 0.65](V vs. Hg/Hg_2SO_4). Scan rate of x mV/s. (a.) Bi bulk ML_{Mass} vs. scan rate. (b.) Bi bulk ML_{Charge} vs. scan rate.

Figure 3-35 compares the Bi bulk ML coverage of Ru with it of Ru echem oxide. The general trend of Bi bulk ML coverage decreases as the scan rate increases. Notice that the Bi bulk ML_{Mass} for Ru and for Ru echem oxide almost overlap with each other.

This indicates that the surface of Bi bulk for Ru are almost the same as the surface of Bi bulk for Ru echem oxide. Figure 3-35 (a.) suggests that the surface of Ru and of Ru echem oxide in Bi bulk region are the same when the Bi bulk ML coverage is more than 5 Bi ML. When the Bi bulk ML coverage is less than 5 Bi ML, approximate 0.5 Bi ML difference between Bi bulk on Ru and on Ru echem oxide.

3.3.4.7. Oxidation Time Effect (with Background Subtraction)

(a.) (b.)

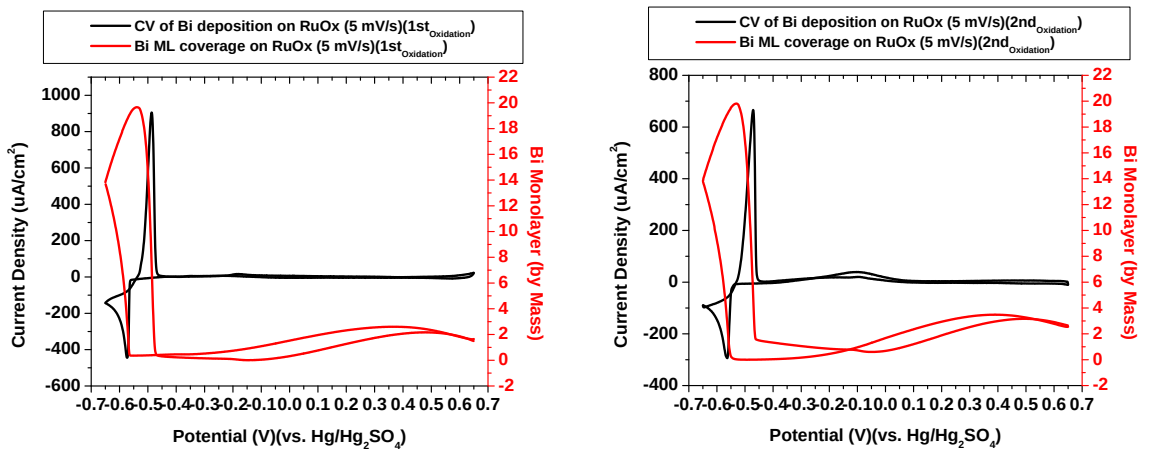

Figure 3-36: Comparison of background-corrected CV and background-corrected Bi ML coverage on Ru echem oxide (RuOx) with different oxidation times. The 1st oxidation is made by progressive oxidation and then hold at 0.9 V (vs. Hg/Hg_2SO_4) for 1 min. The 2nd oxidation is made from the 1st oxidation and then hold at 0.9 V (vs. Hg/Hg_2SO_4) for additional 5 min. Scan range [-0.65, 0.65](V vs. Hg/Hg_2SO_4). Scan rate of 5 mV/s. (a.) The 1st oxidation of RuOx. (b.) The 2nd oxidation of RuOx.

Figure 3-36 compares the Bi deposition on the background-corrected of the 1st-time oxidation of RuOx and on the background-corrected of the 2nd-time oxidation of RuOx. Notice that the Bi bulk peak currents ($I_{P\ Bulk}$) for the 1st oxidation of RuOx is

higher than the Bi bulk peak currents ($I_{P\ Bulk}$) for the 2nd oxidation of RuOx. Although the difference between the CVs in the Bi UPD region is not easily observed, the Bi UPD ML_{Mass} coverage does show some differences. Notice that the anodic region of Bi UPD ML_{Mass} for the 1st oxidation of RuOx has lower stripping slop than the anodic region of Bi UPD ML_{Mass} for the 2nd oxidation of RuOx. In addition, the Bi UPD ML_{Mass} for the 1st oxidation of RuOx has lower Bi ML coverage than the Bi UPD ML_{Mass} for the 2nd oxidation of RuOx by 0.96 Bi ML. This indicates that as the oxidation time increases, the Bi UPD ML_{Mass} also increases. Notice also that the peak stripping current Bi UPD region ($I_{P\ UPD}$) of the 2nd oxidation of RuOx is slightly higher than the peak stripping current ($I_{P\ UPD}$) of 1st oxidation of RuOx.

However, the Bi bulk ML_{Mass} does not change as the oxidation time increases even thought the peak currents ($I_{P\ Bulk}$) in Bi bulk region are different. This indicates that the surface of Bi bulk region for the 1st oxidation and the 2nd oxidation of RuOx are similar due to a complete coverage of Bi adatoms on the RuOx surface before the Bi bulk deposition on the electrode. The peak currents (I_P) differences in Bi bulk region may be caused by systematic error on background correction due to the true background currents for the Bi ML coverage near Bi bulk region are not the same as the background current for the RuOx near the Bi bulk potential region. The current of the Bi UPD adatoms on RuOx may has increased before reaching the Bi bulk region, making the background currents of the RuOx in 0.5M H_2SO_4 solution unavoidably lower than the background current of the RuOx in Bi^{3+} solution.

(a.) (b.)

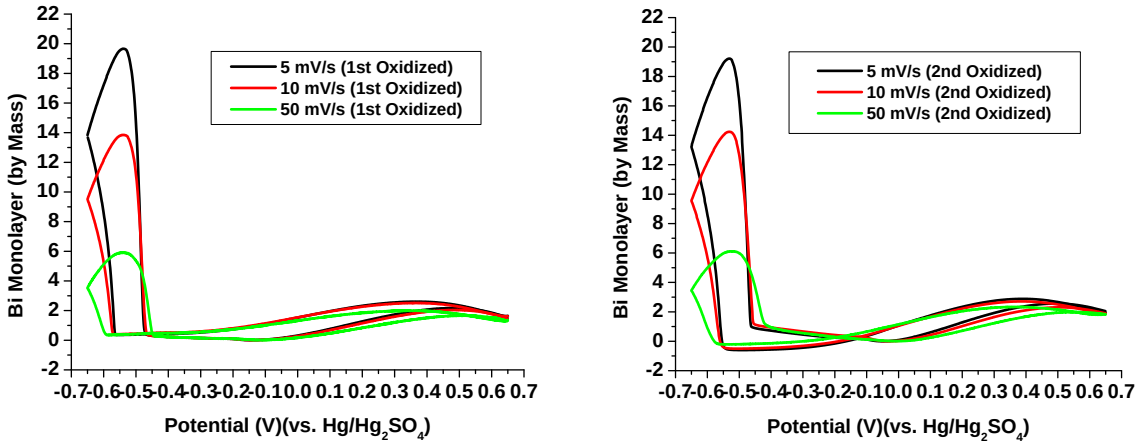

Figure 3-37: Comparison of the scan rate effect on the background-corrected Bi ML_{Mass} coverage of Ru echem oxide (RuOx) with different oxidation times. The 1st oxidation is made by progressive oxidation and then hold at 0.9 V (vs. Hg/Hg_2SO_4) for 1 min. The 2nd oxidation is made from the 1st oxidation and then hold at 0.9 V (vs. Hg/Hg_2SO_4) for additional 5 min. Scan range [-0.65, 0.65](V vs. Hg/Hg_2SO_4). Scan rate of 5, 10, and 50 mV/s. (a.) The 1st oxidation of RuOx. (b.) The 2nd oxidation of RuOx.

Figure 3-37 compares the scan rate effect of the background-corrected Bi ML_{Mass} coverage on the 1st-time oxidation of RuOx and on the 2nd-time oxidation of RuOx. The Bi UPD ML_{Mass} coverage does not change as the scan rate increases, both for the 1st oxidation and for the 2nd oxidation of RuOx. However, the Bi UPD ML_{Mass} from the 2nd oxidation of RuOx has higher Bi ML coverage than the Bi UPD ML_{Mass} from the 1st oxidation of RuOx by 0.60 Bi ML. In addition, the Bi UPD ML_{Mass} stripping slop is higher for the 2nd oxidation than for the 1st oxidation of RuOx. As expected before, the Bi bulk ML_{Mass} does not change for different oxidation times due to a similar surface of Bi adatoms on RuOx before reaching the Bi bulk deposition.

(a.) (b.)

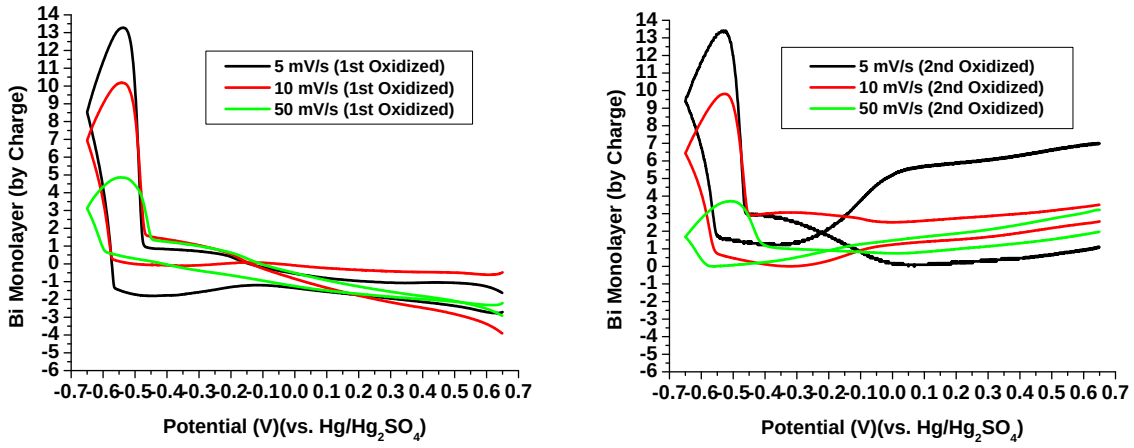

Figure 3-38: Comparison of the scan rate effect on the background-corrected Bi ML_{Charge} coverage of Ru echem oxide (RuOx) with different oxidation times. The 1st oxidation is made by progressive oxidation and then hold at 0.9 V (vs. Hg/Hg_2SO_4) for 1 min. The 2nd oxidation is made from the 1st oxidation and then hold at 0.9 V (vs. Hg/Hg_2SO_4) for additional 5 min. Scan range [-0.65, 0.65](V vs. Hg/Hg_2SO_4). Scan rate of 5, 10, and 50 mV/s. (a.) The 1st oxidation of RuOx. (b.) The 2nd oxidation of RuOx.

Figure 3-38 compares the scan rate effect of the background-corrected Bi ML_{Charge} coverage on the 1st-time oxidation of RuOx and on the 2nd-time oxidation of RuOx. Since the background current for RuOx is higher for longer oxidation time, the Bi ML_{Charge} for the 2nd oxidation RuOx affects larger than the Bi ML_{Charge} for the 1st oxidation RuOx does. Table 3-6 summarizes the Bi ML_{Charge} for the 1st and for the 2nd oxidation of RuOx.

Table 3-6: Summary of Bi ML_{Charge} Coverage for the 1st and for the 2nd oxidation of RuOx.

1st Oxidation RuOx	**Bi Bulk ML_{Charge}**	**Bi UPD ML_{Charge}**
5 mV/s	13.275*	0.995*
10 mV/s	10.195*	1.662*
50 mV/s	4.876*	1.367*
2nd Oxidation RuOx	**Bi Bulk ML_{Charge}**	**Bi UPD ML_{Charge}**
5 mV/s	13.420	3.05
10 mV/s	9.817	2.96
50 mV/s	3.713	1.23

*The zero Bi ML_{Charge} coverage of the 1st oxidation of RuOx was adjusted to be at the same potential as the minimum Bi ML_{Mass} coverage of the 1st oxidation of RuOx.

3.4. Summary

In summary, Bi underpotential deposition was observed both on Ru and on electrochemically formed Ru oxide. Since $RuCl_5^{2-}$ redox species overlap with Bi UPD potential region, Cl^- ion containing solution or reference electrode (Ag/AgCl) are not used in the initial investigation of Bi UPD on Ru and on Ru oxide. The following potentials are with respected to Hg/Hg_2SO_4 reference electrode with scan rates range from 5 mV/s to 250 mV/s.

3.4.1. Bi UPD on Ru

The average Bi UPD ML_{Mass} (0.81 Bi ML) coverage has lower Bi UPD ML coverage than the average Bi UPD ML_{Charge} (2.09 Bi ML). The average difference between Bi UPD ML_{Charge} and Bi UPD ML_{Mass} is 1.28 Bi ML. As the scan rate increases,

the Bi UPD ML stays constant, with the change in Bi UPD ML_{Mass} relatively more stable (average of -0.01 Bi ML_{Mass} with 0.04 Bi ML_{Mass} standard deviation) than the change in Bi UPD ML_{Charge} (average of 0.04 Bi ML_{Charge} with 0.16 Bi ML_{Charge} standard deviation). In addition, the average difference between the peak potential of Bi UPD_{Anodic} and the peak potential of Bi $UPD_{Cathodic}$ (ΔE_P) is 0.20 V with standard deviation of 0.03 V as the scan rate increases. Since the $|\Delta E_P|$ is larger than 0.02 V, the Bi UPD on Ru is a quasi-reversible electron transfer process when the scan rate is 5 mV/s or more. The Bi UPD adatoms on Ru is unstable because the OCPs keep increasing and Bi ML_{Mass} coverage keeps decreasing after stopped at various cathodic potentials. This indicates Bi UPD adatoms and Bi bulk on Ru keep oxidizing and dissolving overtime until they reach a thermodynamically stable state.

3.4.2. Bi UPD on RuOx

The average Bi UPD ML_{Mass} (0.52 Bi ML) coverage has lower Bi UPD ML coverage than the average Bi UPD ML_{Charge} (2.58 Bi ML). The average difference between Bi UPD ML_{Charge} and Bi UPD ML_{Mass} is 2.06 Bi ML. As the scan rate increases, the Bi UPD ML stays constant, with the change in Bi UPD ML_{Mass} relatively more stable (average of -0.03 Bi ML_{Mass} with 0.03 Bi ML_{Mass} standard deviation) than the change in Bi UPD ML_{Charge} (average of -0.34 Bi ML_{Charge} with 0.26 Bi ML_{Charge} standard deviation). In addition, the average difference between the peak potential of Bi UPD_{Anodic} and the peak potential of Bi $UPD_{Cathodic}$ (ΔE_P) is -0.085 V with standard deviation of 0.037 V as the scan rate increases. Since the $|\Delta E_P|$ is larger than 0.02 V, the Bi UPD on Ru echem oxide is a quasi-reversible electron transfer process when the scan rate is 5 mV/s or more. As the oxidation time increases, the Bi UPD ML_{Mass} coverage increases.

3.4.3. Bi UPD on Ru vs. on RuOx

Bi UPD ML_{Mass} on Ru has higher Bi ML coverage than Bi UPD ML_{Mass} on Ru echem oxide, with an average ΔML_{Mass} of 0.29 Bi ML and standard deviation of 0.05 Bi ML. However, Bi UPD ML_{Charge} on Ru has lower Bi ML coverage than Bi UPD ML_{Charge} on Ru echem oxide, with an average ΔML_{Mass} of -0.49 Bi ML and standard deviation of 0.76 Bi ML. Since the background charge of Ru echem oxide is more than 0.76% of the peak current of Bi UPD on Ru echem oxide (5 mV/s), significant error can be introduced when drawing the baseline charge correction. This error in calculating Bi UPD ML_{Charge} on Ru echem oxide can be significant, especially with higher scan rates. Since the Bi UPD ML_{Mass} is higher on Ru than on Ru echem oxide, Ru has higher Bi plating efficiency than Ru echem oxide. The average difference between the anodic peak potential ($\Delta E_{P\ Anodic}$) of Bi UPD on Ru echem oxide and on Ru is 0.021 V with standard deviation of 0.017V, while the average difference between the cathodic peak potential ($\Delta E_{P\ Cathodic}$) of Bi UPD on Ru echem oxide and on Ru is 0.305 V with standard deviation of 0.010V. Both $E_{P\ Anodic}$ and $E_{P\ Cathodic}$ of Bi UPD on Ru shift to positive potentials after electrochemically oxidized of Ru.

3.5. Future Work

In this experiment, the scan rate effect, stability, and oxidation time effect of Bi UPD on Ru and on Ru echem oxide have been investigated. The next stage is to study the purging gas effect, pH effect, solution effect, anion effect, and cation effect of Bi UPD on Ru and on Ru echem oxide.

3.6. References

1. Quiroz, M.; Salgado, L.; Meas, Y. Arrangement of Bismuth on a Ruthenium Electrode. *Electrochim. Acta*. **1988**, *33*, 435-437.

2. Periodic Table of Elements: Los Alamos National Laboratory. http://periodic.lanl.gov/83.shtml (accessed April 2011).

REFERENCE LIST

Applied Research Laboratory at Penn State. http://www.arl.psu.edu/capabilities/mm_mp_ct_sd.html (accessed April 2011).

Bard. A.J.; Faulkner, L.R. *Electrochemical Methods: Fundamentals and Applications*, 2nd ed.; John Wiley & Sons: Chicester, U.K., 2001; Chapter 6.

Buttry, D.A.; Ward. M.D. Measurement of Interfacial Processes at Electrode Surfaces with the EQCM. *Chem. Rev.* **1992**, *92*, 1355-1379.

Cheng, T.J.; Li, K.F.; Chang, H.C. The Principle and Application of Electrochemical Quartz Crystal Microbala. *Chemistry (The Chinese Chem. Soc., Taipei)*, **2001**, *59*, 219~233.

Chung, S.Y.; Uhm, S.H.; Lee, J.K.; Kang, S.J.; Tak, Y.S.; Lee, J.Y. Electrocatalytic Oxidation of HCOOH on Pt-based Anodes. *J. Ind. Eng. Chem.* **2007**, *13*, 339-344.

Du, Y.; Wang, C. Preparation Ru, Bi monolayer modified Pt nanoparticles as the anode catalyst for methanol oxidation. *Mater. Chem. Phys.* **2009**, *113*, 927-932.

Handbook of Instrumental Techniques for Analytical Chemistry, 1st ed. Settle, F., Ed.; Prentice Hall: Englewood Cliffs, NJ, 1997; Chapter 37, p 709.

Handbook of Thin Film Deposition Processes and Techniques: Principles, Methods, Equipment and Applications, 2nd Edition. Seshan, K., Ed.; Noyes: Norwich, NY, 2002; Chapter 8, p 319.

Herrero, E.; Buller, L.J.; Abruna, H.D. Underpotential Deposition at Single Crystal Surfaces of Au, Pt, Ag and Other Materials. *Chem. Rev.* **2001**, *101*, 1897-1930.

http://www.uccs.edu/~tchriste/courses/PHYS549/549lectures/sputtertech.html (accessed April 2011).

Kinetronics Corporation—Anti-Static Film Cleaning Brushes and Devices. http://kinetronics.com/PLCMSDSData.pdf (accessed April 2011).

OEHHA Water: Public Health Goals (PHGs). http://oehha.ca.gov/water/phg/pdf/dcm.pdf (accessed April 2011).

Oh, I.; Gewirth, A.A.; Kwak, J. Electrocatalytic Dioxygen Reduction on Underpotentially Deposited Tl on Au(111) Studied by an Active Site Blocking Strategy. *Langmuir*. **2001**, *17*, 3704-3711.

Periodic Table of Elements: Los Alamos National Laboratory. http://periodic.lanl.gov/83.shtml (accessed April 2011).

Physics of Thin Films—Sputter Deposition Techniques.

Quiroz, M.; Salgado, L.; Meas, Y. Arrangement of Bismuth on a Ruthenium Electrode. *Electrochim. Acta*. **1988**, *33*, 435-437.

Rubinstein, I., Ed. *Physical electrochemistry: Principles, Methods, and Applications.* CRC Press: Boca Raton, FL, 1995; Chapter 7.

Schmidt, T.J.; Grgur, B.N.; Behm, R.J.; Markovic, N.M.; Ross, Jr. P.N. Bi adsorption on Pt(111) in perchloric acid solution--A rotating ring–disk electrode and XPS study. *Phys. Chem. Chem. Phys.* **2000**, *2*, 4379-4386.

Shiue, W.J. Determination of trace copper by underpotential deposition-stripping voltammetry at nanoporous gold electrode. M.S. Thesis, National Cheng Kung University, Tainan, Taiwan, July 2006.

Single-Molecule and Nanobiology Laboratory. http://snl.bjmu.edu.cn/course/reviews/bitech/LvYalinT.pdf (accessed April 2011).

Sudha, V.; Sangaranarayanan, M.V. Underpotential Deposition of Metals—Progress and Prospects in Modeling. *J. Chem. Sci.* **2005**, *117*, 207-218.

Zhu, W.; Yang, J.Y.; Zhou, D.X.; Bao, S.Q.; Fan, X.A.; Duan, X.K. Equilibrium Thermodynamics Analysis of Underpotential Deposition of Bi-Te Substrate System Thermoelectric Material. *Chemical Journal of Chinese Universities*. **2007**, *28*, 719-722.